Constructing Multifunctional Therapeutic Nanosystems for Photo-immunotherapy of Glioblastoma

Zhang, Ming

Publication date:
2021

Document Version
Publisher's PDF, also known as Version of record

Constructing Multifunctional Therapeutic Nanosystems for Photo-immunotherapy of Glioblastoma

PhD Thesis

Ming Zhang

December 2021

Constructing Multifunctional Therapeutic Nanosystems for Photo-immunotherapy of Glioblastoma

Ming Zhang

PhD Thesis

December 2021

CONTENTS

ABBREVIATIONS

BBB	Blood brain barrier
NPs	Nanoparticles
B1R	B1 receptor
ROS	Reactive oxygen species
CTLs	Cytotoxic T lymphocytes
aPDL1	Anti-PDL1 antibody
PDT	Photodynamic therapy
PTT	Photothermal therapy
NIR	Near-infrared region
PpIX	Protoporphyrin IX
AIE	Aggregation-induced-emission
LITT	Laser interstitial hyperthermia
CNS	Central nervous system
FDA	Food and Drug Administration
GBM	Glioblastoma
5-ALA	5-Aminolevulinic acid hydrochloride
UCNPs	Upconverting nanoparticles
BK	Des-Arg9-Kallidin
NK	Natural killer
TME	Tumor microenvironment
CLSM	Confocal laser scanning microscopy
FUS	Focused ultrasound
MTT	Methyl thiazolyl tetrazolium
DAPI	4’,6-diamidino-2-phenylindole
EDC	1-Ethyl-3-[3-dimethylaminopropyl]carbodiimide hydrochloride
NHS	Hydroxy-2,5-dioxopyrrolidine-3-sulfonicacid sodium salt
TUNEL	Terminal deoxynucleotidyl transferase dUTP nick end labeling
H&E	Hematoxylin and eosin
TEM	Transmission electron microscope
MR	Magnetic resonance

ABSTRACT

The blood brain barrier (BBB) is the gateway to maintain the information exchange between the internal microenvironment of the brain and the surrounding microvascular system. Due to the existence of the BBB, majority of small molecules and almost all macromolecular substances cannot enter the brain area. This is the biggest challenge to treat brain and central system diseases by traditional chemotherapy. Furthermore, the *in vivo* short circulation time and fast metabolism of most drug-loading systems reduce the efficiency of accumulation in the brain area, which leads to an unsatisfied therapeutic concentration. For glioblastoma (GBM), currently there is no very effective cure clinically, mainly because GBM extends the antennae into the brain instead of forming a solid mass that can be targeted and removed. Therefore, there is an urgent need for new treatments to cure GBM. With the advancement of modern frontier treatments, new developments have been brought to the treatment of brain tumors. Photo-immunotherapy, as one of the emerging treatment methods, not only kills cancer cells but can also eliminate other unfavorable cells, without damaging favorable cells. This technique can efficiently activate anti-tumor host immunity in a way that can even cure untreated distant metastasis. Nano-delivery systems have been developed to achieve targeted delivery and treatment of brain tumors. However, there is still a need to further improve the delivery effectiveness as well as therapeutic efficacy.

In this thesis, we have constructed the nanosystems with good biocompatibility to achieve effective treatment of GBM. We achieve photo-immunotherapy for brain tumors by NIR laser-induced PDT or PTT. With the modification of the BK ligand on the surface of nanoparticles (NPs), the BBB is in a highly permeable state that endows high crossing efficiency. The long-circulating NPs have shown excellent abilities in cell internalization, crossing the *in vitro* BBB model-a single-layer cell model, and a GBM-bearing mouse model. In general, the surface-modified NP changes the circulation pattern of NPs *in vivo* and provides an effective way to cross the BBB. Overall, we provide potential platform for GBM-targeted drug delivery as summarized below.

(i) To overcome the immunological tolerance of brain tumors, we report novel multifunctional NPs for highly efficient synergetic immunotherapy. The NPs contain an anti-PDL1 antibody (aPDL1), upconverting NPs (UCNPs), and the photosensitizer 5-Aminolevulinic acid hydrochloride (5-ALA); the surface of the NPs is conjugated with the B1 receptor (B1R) kinin

ligand to facilitate transport across the BBB. Upon irradiation with a 980 nm laser, photodynamic therapy (PDT) is initiated by transforming 5-ALA into protoporphyrin IX (PpIX), which will generate reactive oxygen species (ROS). PDT further promotes intratumoral infiltration of cytotoxic T lymphocytes (CTLs) and sensitizes tumor to PDL1 blockade therapy. We demonstrated that combining PDT and aPDL1 could effectively suppress GBM growth in mouse models. The proposed NPs provide a novel and effective strategy for boosting against GBM photo-immunotherapy.

(ii) B1R kinin ligand (BK) aggregation-induced-emission (BK@AIE) NPs are synthesized; these offer selective penetration through the BBB and strong absorbance in the NIR. The BK ligand can promote the activation of BBB adenosine receptor, which enhances NPs transportation and accumulation inside tumors, as confirmed by T1-weighted magnetic resonance and fluorescence imaging. The BK@AIE NPs exhibit high photothermal conversion efficiency under 980 nm NIR laser irradiation that facilitates the treatment for deep-seated tumors. The survival span of mice is prolonged by effectively inhibiting tumor progression under spatiotemporal photothermal therapy (PTT). NIR irradiation can eradicate tumor tissues and release tumor-associated antigens. It is observed that the PTT treatment of GBM-bearing mice activates natural killer (NK) cells, CD3+ T cells, and M1 macrophages in the GBM area, increasing the therapeutic efficacy. This study demonstrates that NIR-assisted BK@AIE NPs represent a promising strategy for the improved systematic elimination of GBMs and local brain immune privilege activation.

ACKNOWLEDGEMENTS

First, I want to thank Professor Yi Sun for her painstaking efforts and selfless teachings from the beginning to the end, including the topic selection, design, guidance, and the writing and revision of the thesis. My mentor's selfless dedication reflects every step of my growth and progress. Yi has always inspired and educated me with her profound knowledge, rigorous scholarship, keen thinking, generous and kind mind, tireless teaching style, and persevering spirit of seeking truth. Yi has provided me with excellent research conditions and a relaxed academic research atmosphere so that I have enough space to expand my research interests, broaden my research ideas, and carry out research work alone, all of which have benefited me for life. In my study and life, Yi has given me great support, care, and help. Every bit of my progress is condensed with her hard sweat.

I want to thank Professor Sine Reker Hadrup of our department for her care and help in scientific research. I want to thank Qicheng Zhang, Professor Ninglin Zhou, and Professor Jian Shen of Nanjing Normal University for their support and help in the research and study. I want to thank Professor Ben Zhong Tang and Doctor Shunjie Liu of Hong Kong Polytechnic University for their support and help in the research and study. Thanks to the enthusiastic help of Wentao Wang, Tao Zheng, Mohsen Mohammadniaei, Jon Ashley, Maryam Naseri, Xiaotong Feng, and Zeqin Li in the laboratory, which enabled me to master the experimental technology faster.

I want to sincerely thank my parents for their cultivation and education over the years. I want to thank my wife, Wentao, for your support and genuine understanding during my schooling. Finally, I want to thank all the experts and professors who reviewed the paper and attended the defense for their selfless guidance. Lastly thanks again for all the help and care of my supervisors, peers, and family; thank you.

LIST OF PUBLICATIONS

Publications included in the thesis

Ming Zhang, Xuefeng Jiang, Qicheng Zhang, Tao Zheng, Mohsen Mohammadniaei, Wentao Wang, Jian Shen, Yi Sun. "*Biodegradable Polymeric Nanoparticles Containing an Immune Checkpoint Inhibitor (aPDL1) to Locally Induce Immune Responses in the Central Nervous System*." *Advanced Functional Materials* (2021): 2102274.

Ming Zhang, Wentao Wang, Mohsen Mohammadniaei, Tao Zheng, Qicheng Zhang, Jon Ashley, Shunjie Liu, Yi Sun, Ben Zhong Tang. "*Upregulating Aggregation-Induced-Emission Nanoparticles with Blood Brain Barrier Permeability for Precise Photothermal Eradication of Brain Tumors and Induction of Local Immune Responses*." *Advanced Materials* 33 (2021): 2008802.

Publications not included in the thesis

Mohsen Mohammadniaei, **Ming Zhang**, Jon Ashley, Ulf Bech Christensen, Lennart Jan Friis-Hansen, Rasmus Gregersen, Jan Gorm Lisby, Thomas Lars Benfield, Finn Erland Nielsen, Jens Henning Rasmussen, Ellen Bøtker Pedersen, Anne Christine Rye Olinger, Lærke Tørring Kolding, Maryam Naseri, Tao Zheng, Wentao Wang, Jan Gorodkin, Yi Sun. "*A non-enzymatic, isothermal strand displacement and amplification assay for rapid detection of SARS-CoV-2 RNA*." *Nature Communications* 12 (2021): 1.

Qicheng Zhang, WentaoWang, **Ming Zhang**, Fan Wu, Tao Zheng, Bulei Sheng, Yihan Liu, Jian Shen, Ninglin Zhou, Yi Sun. "*A theranostic nanocomposite with integrated black phosphorus nanosheet, Fe_3O_4@MnO_2-doped upconversion nanoparticles and chlorin for simultaneous multimodal imaging, highly efficient photodynamic and photothermal therapy*." *Chemical Engineering Journal* 391 (2020): 123525.

1. INTRODUCTION

1.1 Brain Tumor and Treatment Method

1.1.1 Overview of Brain Tumor

Brain cancer is one of the most deadly cancers because of its high proliferative ability, widespread effect on any ages, and abysmal prognosis. Brain tumor refers to the formation of abnormal cells in brain. The location includes various cells of the brain itself, cranial nerves meninges, skull, pituitary gland, and metastatic brain tumors metastasized from other organs.[1] There are basically two main tumor types: malignant or cancerous tumors and benign tumors. Brain tumors can be further divided into primary brain tumors and metastatic brain tumors.[2] Symptoms occur with the gradual enlargement of all types of brain tumors because of the inevitable compression of the nerves in the area to affect its function.[3] For instance, the tumor-location-dependent clinical manifestations vary from headache, convulsions, and vision problems to vomiting, even unconsciousness with the disease progress.[4, 5] In the advanced stage of malignant brain tumor, tumor cells will also transfer to other organs inside the body. Even with surgical resection operation, the average time for tumor recurrence is 6.9 months while the average survival time is only 14.6 months.[6] In the past 30 years, the clinical results of glioblastoma (GBM) patients showed barely improvement with standard therapies (such as chemotherapy, surgery, and adjuvant radiotherapy).[7] The average overall survival time is 16.6 months.[8, 9] Resistance to traditional therapies is prone to appear during treatment. There is an urgent need for new treatments in the clinic.

1.1.2 Treatment of Brain Tumor

1.1.2.1 Surgical Therapy

The elementary knowledge of brain is that it is a fragile organ to perform operations such as biopsy. Considering the critical function and location of brain in human sapiens life, regardless of the tumor stage (primary brain tumors or metastasized brain tumors), huge challenges are encountered by the surgery treatment.[10-12] The surgical treatment of brain tumors is divided into (i) transcranial microsurgery and (ii) transnasal endoscopic surgery (as shown in **Figure 1**).[13] Until now, surgery is still the main strategy to remove brain tumors *in vivo*. Even if the tumor is successfully removed, surgery may affect the corresponding brain function of the

lesion. Moreover, some of these tumors may be benign, to even increase the risk of surgery, which may outweigh the benefits of surgery.[14]

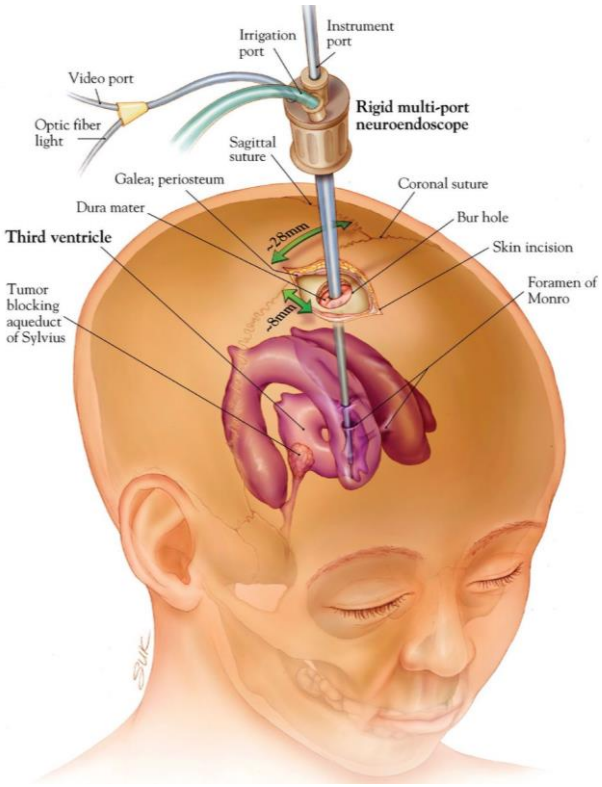

Figure 1. A purely endoscopic neurosurgical procedure.[13]

1.1.2.2 Radiation Therapy

Radiation therapy is now generally regarded as an essential treatment option for brain tumors (as shown in **Figure 2**).[15] However, the following shortcomings of irradiation therapy limit its effects to some extent. More than 20 years ago, radiation therapy for brain cancer in some cases inevitably radiating most of the brain or the entire brain, such as cancer that has metastasized to the brain.[16] This means that even if a specific tumor only occupies 5% of the brain volume, the other 95% of the brain must be irradiated.[17] Whole-brain radiation therapy takes several weeks and may cause neurotoxicity.[18] More serious side effects occur along with the repeatable irradiation; patients may suffer from cognitive impairment or encounter difficulties in walking or communication that seriously affect their life quality. A big improvement of radiation therapy is that, some radiation oncologists can now send targeted radiant beams to the tumor radiation rather than using whole-brain radiation, which shields the rest brain tissues from radiation.[19]

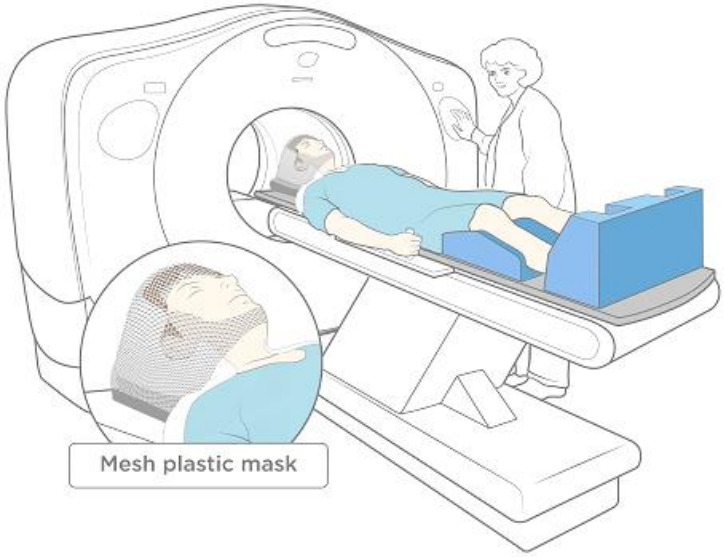

Figure 2. Radiation therapy to the brain.[15]

1.1.2.3 Chemotherapy

There are still many difficulties or obstacles in treating brain tumors by chemotherapy. The highly heterogeneous characteristic endows complex components and behaviors to the primary malignant brain tumor. This makes it challenging to target a single disease. In addition, chemotherapeutic drugs for the brain tumor are limited by the central nervous system (CNS). Since the 1960s, only three drugs have been approved by the U.S. Food and Drug Administration (FDA) to treat brain tumors.[20, 21] Whether endogenous or acquired, drug resistance is more common complication in brain tumors.[22-24] A significant obstacle of brain tumor chemotherapy is the existence of the blood brain barrier (BBB) that induces a difficulty in the delivery of drugs to the tumor site. The subsequent insufficient drug concentration and action time in tumor cells, defective drugs penetration across the BBB, and other factors will affect the efficacy of chemotherapy.[25]

1.1.2.4 Gene Therapy

Gene therapy can be defined as treating diseases by introducing therapeutic genes or manipulating disease-related genes (such as downregulating activated oncogenes in target cells).[26] With the better understanding of the mechanism of virus-cell interaction and advances in recombinant DNA technology, gene therapy has been applied to several cancers.[27, 28] As one of the most frustrating cancer types, brain cancer is an ideal target for gene therapy because the current standard treatment methods are still highly inefficient (as shown in **Figure 3**).[29] Although gene therapy has been successful in preclinical studies, most GBM patients

ultimately failed to significantly prolong survival period in early clinical studies. This is partly because the experimental therapies in early clinical studies are usually used for patients with recurrent or progressive GBM.[30] Even if mature treatments are used in the trial, there may only be slight reactions to these overdeveloped tumors. To correctly evaluate the efficacy, early GBM patients also need to be included in clinical studies. The remaining challenges of GBM gene therapy include limited transduction efficiency of viral vectors, histological heterogeneity of the cell population, lack of the delivery system to cross BBB, failed distinction of tumor cells and normal cells, and selective expression of transgenes in a therapeutically controlled manner.[31-33]

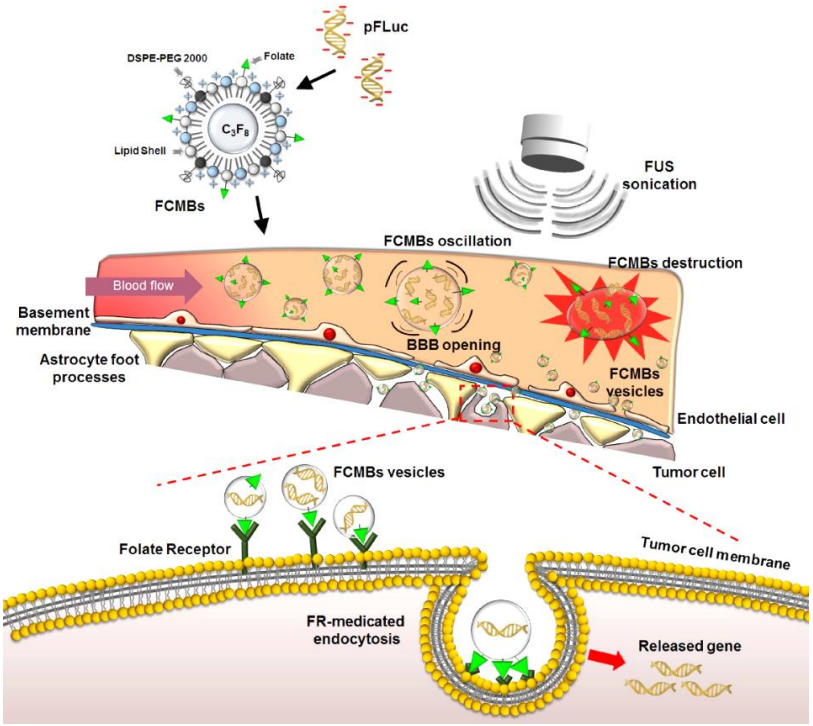

Figure 3. With focused ultrasound (FUS) sonication, the DNA-loaded NPs are destroyed into DNA-containing and folate-inserting vesicles that have increased BBB permeability.[29]

1.1.2.5 Laser Interstitial Hyperthermia

Laser Interstitial Hyperthermia (LITT) was first proposed in 1983.[33] It is a minimally invasive technique for treating difficult-to-resectable intracranial lesions, such as tumors, radiation necrosis, functional areas in the brain, or epileptic foci of deep nuclei and white matter. It also is a viable option for patients who are not suitable for surgery due to comorbidities or risks of anesthesia. LITT is a tissue destruction technique that uses heat energy to produce cell death in the target lesion.[34, 35] At 43 °C for 60 minutes, heating will cause protein denaturation, membrane lipid destruction, enzyme activation, and irreversible tissue damage (as shown in

Figure 4).[36] The pathological tissues are selectively targeted for precise ablation using the inherent thermal conductivity difference between pathological and normal tissues. Although LITT has shown great potential in treating GBM, there are still many problems to be solved, especially postoperative complications caused by improper operation and an extensive range of cerebral edema.[37, 38] Therefore, there is an urgent need for new and more effective strategies. Real progress can only be achieved by increasing our understanding of the biology of these tumors and discovering new mechanisms for intratumoral delivery.

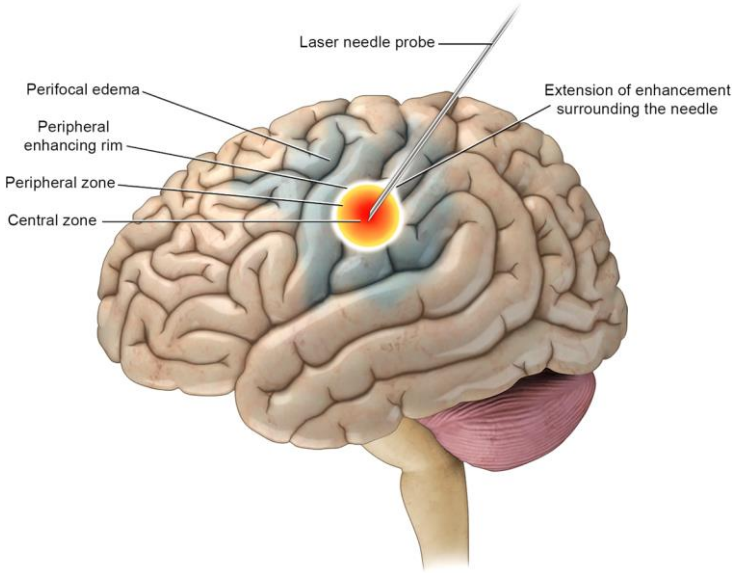

Figure 4. Immediately after and in the early stages after LITT (0 to 3 months post-procedure). The treated lesion shows a distinct central zone and peripheral zone surrounded by vasogenic edema.[36]

1.2 BBB and Overcoming Method

1.2.1 Overview of the BBB

The essential structure of the BBB heavily relies on the function of tight junctions of endothelial cells.[39] Endothelial cells are located inside all blood vessels and tightly connected in the capillaries to form a so-called tight junction structure.[40-42] This tight gap can only allow small molecules, fat-soluble molecules, and some gases to pass through the capillary wall and enter the brain tissue; some large and specific molecules, such as glucose, can obtain access permits through transporters, which can play the role of a particular "door" (as shown in **Figure 5**).[43] Surrounding vascular endothelial cells are other BBB components. These components do not strictly organize the material from the blood into the brain, but they communicate with the cells that form the BBB to change the selectivity of the BBB.[44, 45] The BBB changes in the

brain metastases of primary brain tumors (GBM) and other cancers (including lung cancer, breast cancer, and melanoma). The change of BBB will affect its permeability, and this structure participates in the mutual regulation pathway with tumor cells.[46] Importantly, BBB usually retains the heterogeneous ability to limit the penetration of many therapeutic drugs into intracranial tumors.[47] Overcoming this challenge is the key to improving the effectiveness of treatment.

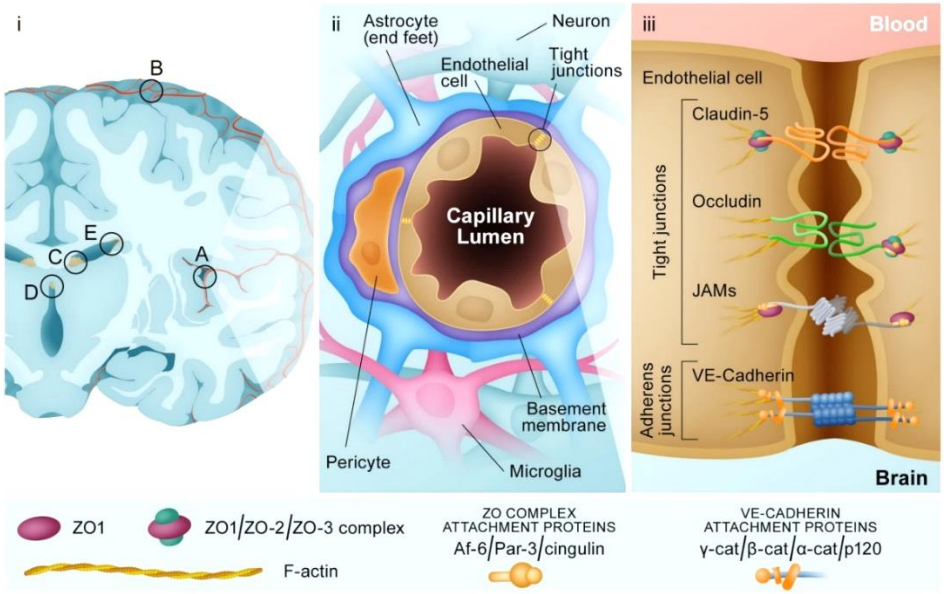

Figure 5. The overview of the BBB.[43]

1.2.2 Methods to Overcome the BBB

1.2.2.1 Focused Ultrasound

For many years, scientists have been trying to find efficient methods to break through the BBB.[48] However, almost no technology is developed to deliver drugs to where it is needed without affecting other parts of the body, and the action is reversible (the barrier opens and closes) at high speed. Some researchers have found that the ultrasound (a frequency higher than the range of human hearing) is entirely harmless based on the injection of lipid-encapsulated gas microbubbles (the drug is ultrasound) in an independent vein (as shown in **Figure 6**).[49, 50] After the rupture due to the action of ultrasound, the fluorescent substance attached to the microbubbles will be released, revealing the open area of the BBB in the mouse brain.[50] Ultrasound is focused on a specific brain area where microbubbles begin to oscillate and increase in size due to the interaction with sound waves. With these tiny bubbles a critical dimension of 8 μm is reached, hence the near BBB structure will temporarily open and allow

the circulating drugs to pass through.[51, 52] This technology has been successfully used for more than ten years, but serious adverse effects along with its application that is the drugs will pass through the entire circulatory system and reach to other organs and cause adverse effects.

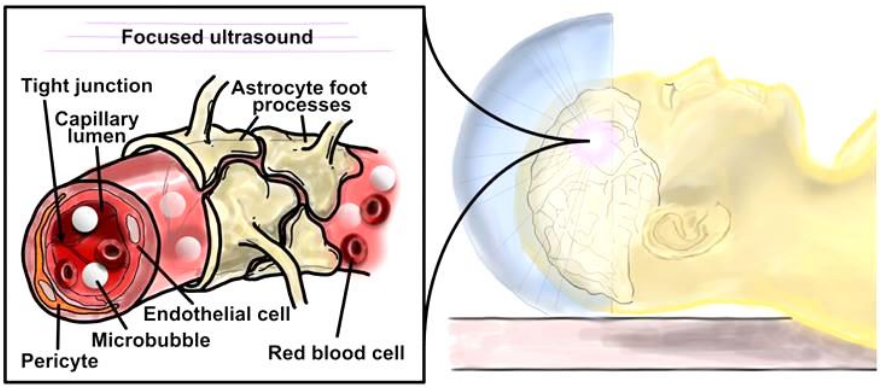

Figure 6. Schematic of microbubble-assisted focused ultrasound BBB disruption.[49]

1.2.2.2 Laser

Laser technology is approved by the FDA as a surgical method for treating brain tumors in 2009. The tool includes a small laser needle probe that heats and ultimately kills tumor cells.[53] When neurosurgeons used lasers to treat brain tumors, they found that the technology could break through the BBB. This research result provides a new treatment option for GBM patients. Eric Leuthardt, professor of neurosurgery at Washington University in St. Louis, reveals that the BBB was disintegrating about four weeks after laser treatment (as shown in **Figure 7**).[54] By disabling the BBB, substances can enter in the brain, but breaking the BBB can also induce substances flow out into circulated blood, leaving the peripheral system and immune system.

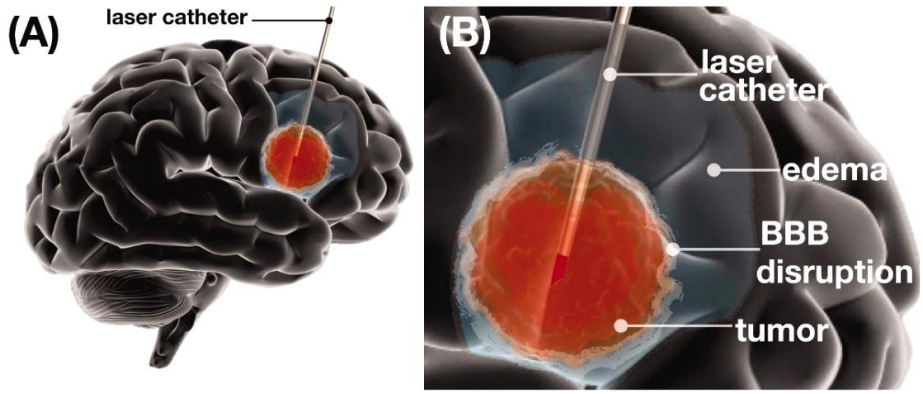

Figure 7. BBB was in a disintegrating state after laser treatment.[54] (A) Schematic representation of intratumoral placement of laser catheter and brain tumor ablation. (B) Schematic representation of brain tumor ablation demonstrating post-LITT contrast enhancement consistent with LITT related BBB disruption and LITT related perifocal edema.

1.2.2.3 Modification of NPs

NPs, as an emerging contrast agent, antireflection agent and transport carrier, have been widely used in biology, immunology, and clinical research, and have become a breakthrough point in the diagnosis, and treatment of brain diseases.[55, 56] With the rapid development of nanomaterials, researchers have used NPs effectively across the BBB. According to the excellent physical properties of nanomaterials, in recent years, many *in vivo* and *in vitro* studies have respectively reported that organic and inorganic nanomaterials as drug carriers can effectively deliver chemotherapeutic drugs into glioma cells and kill tumor cells.[57-59]

1.2.2.3.1 Biochemical Reagent Action

There are some special receptors on BBB endothelial cells, such as transferrin receptor, epidermal growth factor receptor, amino acid transporter, glucose transporter, and etc. The specific protein peptide ligands, carbohydrate ligands or nucleic acid ligands of these receptors can be "installed" on the drug delivery system.[60, 61] The drug delivery system coated with the endogenous ligand can smoothly cross the BBB to achieve the brain-targeted delivery of drugs (as shown in **Figure 8**).[62]

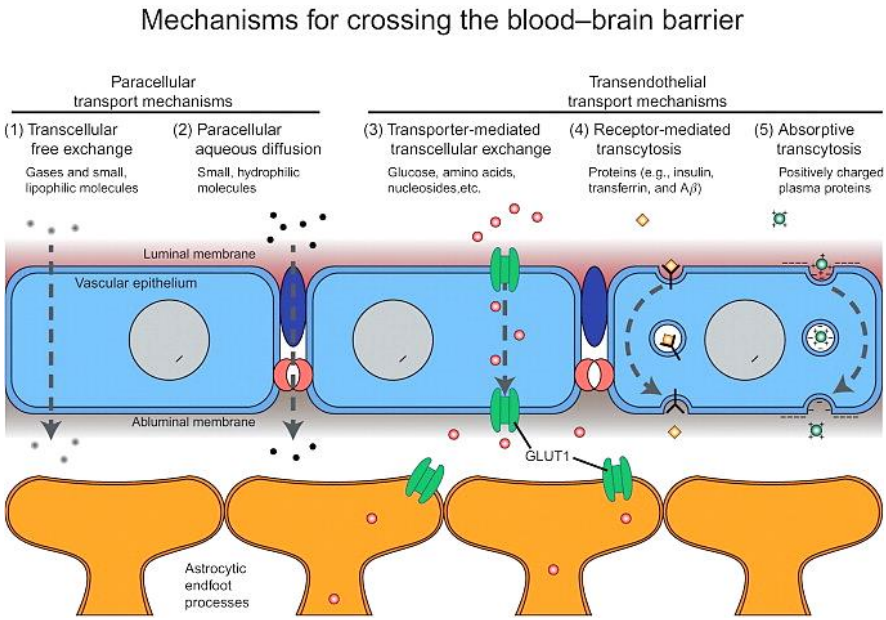

Figure 8. Transport across the BBB occurs through a variety of mechanisms.[62]

1.2.2.3.2 Hydrophilic Group Modification

Hydrophilic groups have high flexibility and important space steric effect that can through the lower drug delivery system with van der Waals force, electrostatic forces, and hydrophobic

action. This weakens the interaction between them, to (i) escape the capture of phagocytic cells, (ii) extend the retention time in the blood circulation, and (iii) supply more targeted drug delivery in the diseased cells.[63-65] In Liu's work, they revealed that drug absorption on carbamazepine NPs coated with carboxymethyl chitosan was improved in blood and brain tissue compared to uncoated carbamazepine.[66] The increase penetration of coated NPs to brain tissue indicates that the NPs modified with hydrophilic groups have higher brain targeting.

1.2.2.3.3 Reduce the Size of the Delivery System

The reticuloendothelial system in the liver, spleen, and blood can selectively swallow foreign particles in the blood. In general, the size of particles is in the range of 200-800 nm, the smaller they are, the less the steric hindrance between the phagocytes occurs, and the easier penetration takes place.[67, 68] However, once the particle size reduces to below 200 nm, the curvature of the local area of the carrier surface will also become smaller (as shown in **Figure 9**).[69] The sites that bind to opsonins are also reduced, which can instead avoid being adsorbed by receptors on the surface of phagocytes, thereby escaping the phagocytosis and clearance of phagocytes.

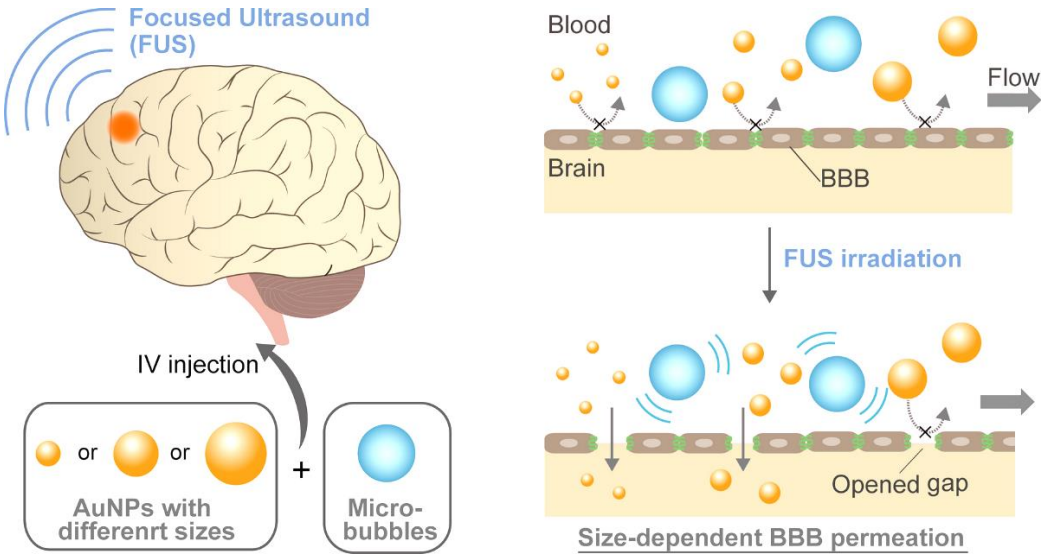

Figure 9. Size-dependent delivery of NPs into the brain assisted by FUS-induced BBB opening.[69]

1.2.3 Change the Route of Administration

1.2.3.1 Nasal Delivery

In the nasal administration, the drug is first exposed to the nasal mucosa. There is olfactory epithelium on the nasal mucosa, and the olfactory nerve and trigeminal nerve innervate the olfactory epithelium (as shown in **Figure 10**).[70] Therefore, the main route of intranasal

administration is through the olfactory nerve and trigeminal nerve pathway. Hydrangea then enters the brain tissue or cerebrospinal fluid. The transport through the olfactory pathway is divided into slow intra-neuronal (in-axon) transport and faster extra-neuronal (extracellular space) transport. After entering the brain, drugs entrance mainly occurs through a simple diffusion. In other areas, arterial pulse action will also be involved.[71]

Currently, clinically available intracerebral drug delivery routes mainly include intraventricular or intracerebral parenchymal injection, intracranial delivery using micropump, catheter infusion, focused ultrasound to open the BBB.[72, 73] However, these invasive operations can induce high risks, whereas the intranasal administration is easily accessible. It can avoid the liver's first pass of drug metabolism, and the dose of intranasal administration is usually 2-10 times lower than the oral dose.[68] In the recent years, a variety of therapeutic drugs (including small and large molecules, peptides and proteins, synthetic genes) have been delivered through nasal delivery to the CNS to treat neurological diseases such as Alzheimer's disease and brain tumors.[74-76]

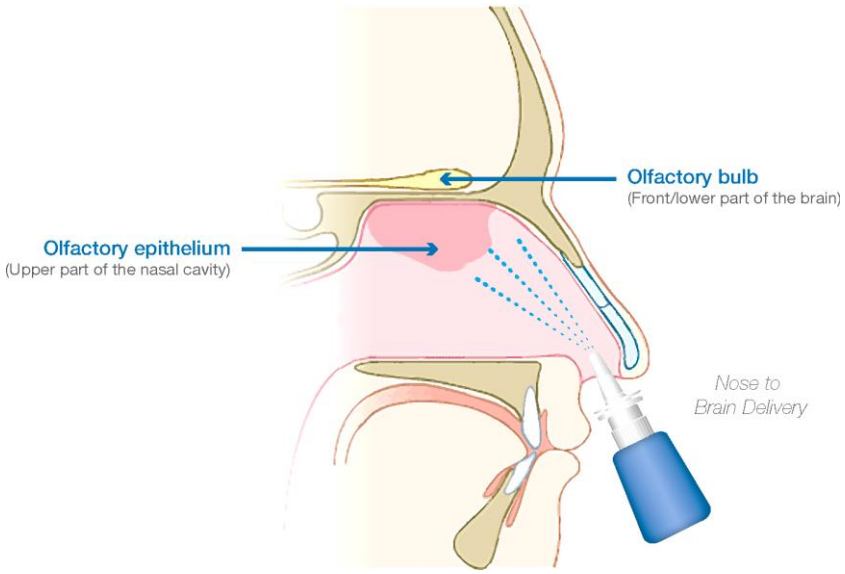

Figure 10. Pathways available to drugs for potential transport to the brain.[70]

1.2.3.2 Intrathecal Injection

Recently, intrathecal injection of chemotherapeutic drugs has become one of the most effective methods to prevent and treat CNS-related diseases.[77, 78] The subsequent toxic effects or complications of CNS have brought great pain to patients. The intrathecal injection is to inject the drug directly into the subarachnoid space through a lumbar puncture, the generated postoperative complications need to be reduced by careful care.[79] The drug is dispersed in the

cerebrospinal fluid, and the effective blood drug concentration is quickly reached. It is reported that most of the isotope-labeled albumin can reach the subarachnoid space on the brain surface within 4-6 hours after injecting into the sheath. Intrathecal administration ensures the medicine circulates with the cerebrospinal fluid to naturally reach the brain cisterns in the subarachnoid space and disperse in the entire ventricular system (as shown in **Figure 11**).[80] Short-term repeated administration can maintain a specific effective drug concentration, which is a better route of administration and treatment for intracranial infection.

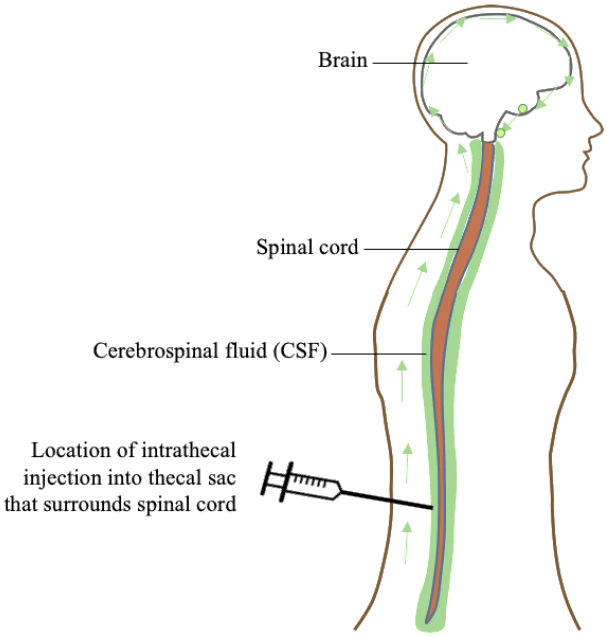

Figure 11. A diagram of how intrathecal injections work.[80]

Although many methods to overcome the BBB have been reported, these methods have high practical value and research value for drug delivery in the brain.[81, 82] However, at this stage, some drugs with NPs as carriers and physical opening methods have entered the clinical stage, but most of the research is still at the stage of animal experiments. There are still many problems with the methods of opening the BBB: (i) histocompatibility and safety; (ii) the mechanism of the opening of the BBB is unclear; (iii) the controllability of the "switch" of the BBB; (iv) irreversibly damage the BBB; (v) it is difficult to accurately monitor the release of drugs in the brain; (vi) the efficiency of opening the BBB is low.[83-85]

1.3 Potential Therapies for Brain Cancer

1.3.1 Photodynamic Therapy

Photodynamic therapy (PDT) is a new type of cancer treatment mode, which has shown promising results in the minimally invasive treatment of various cancers.[86] The basic principle of PDT is that the half-life of administered photosensitizers is different in systemically or locally tissue. After a while, photosensitizer concentration in tumor tissues is significantly higher than that in normal tissues, resulting in selective retention of photosensitizers in tumor tissues.[87, 88] The reactive oxygen species (ROS) were generated under a specific excitation wavelength, leading to tumor cell necrosis and apoptosis.[89] PDT has the following advantages: (i) high selectivity: the photosensitivity reaction occurs in tumor cells and neovascular endothelial cells after laser irradiation; (ii) minimally invasive: the treatment does not require major surgery and only cooperates with endoscopy or other interventional techniques to guide the laser into the body; (iii) definite curative effect: due to the strong drug positioning effect during the treatment process, the photochemical reaction can be produced on all tumor tissues and cells containing photosensitizers.[90-92] It can simultaneously enhance the immune system resistance against tumors. PDT also has own disadvantages: (i) it is impossible to remove cancer cells that have spread in almost all organs and tissues; (ii) once the photosensitizer is injected, the sensitivity to light will last for a while.[93]

1.3.2 Photothermal Therapy

As a minimally invasive, precise, controllable, and effective treatment modality, photothermal therapy (PTT) is a treatment that uses photothermal materials to convert light energy into local overheating, thereby killing cancer cells. PTT has achieved gratifying achievements in preclinical and clinical practice.[94, 95] Recently, the typical organic photothermal therapeutic agents (including nanomicelles encapsulating NIR dyes, photothermal therapeutic agents based on protein structure, porphyrin liposomes, and polymer NIR absorbing materials) are reported, and their respective properties are introduced.[96-99] Compared with the inorganic materials, organic photothermal therapeutic agents are easier to move towards clinical applications due to their biosafety potential, however, there are still limitations to be improved. Some of them include; (i) safety issues in clinical application; (ii) The structure and surface properties need to be further optimized; (iii) combination of multiple treatment techniques, its implementation requires related medical equipment; (iv) the biggest obstacle of PTT is the small penetration depth of light.[100-102]

1.3.3 Immunotherapy

The idea that the human immune system can fight tumors dates back to the 1850s, when Rudolf Virchow, a German pathologist, firstly observed the infiltration of immune cells in human tumor tissue.[103] Later, the American surgeon Coley firstly used the method of injecting bacteria into the soft tissue of the tumor to induce immune response.[104] Nowadays, with the maturation of antibody preparation and other related technologies, immunotherapy has been developed rapidly and become another effective treatment for cancer following surgery, radiotherapy, chemotherapy, and targeted therapy.[105, 106] In particular, the "immune checkpoint" mechanism leading to the suppression of the T cell immune response was identified. With the further understanding of immune response mechanisms in tumor, more and more binding sites on the inhibition and activation pathways have been proposed (as shown in **Figure 12**).[107] A large number of preclinical and clinical studies have been conducted on drugs targeting these sites.

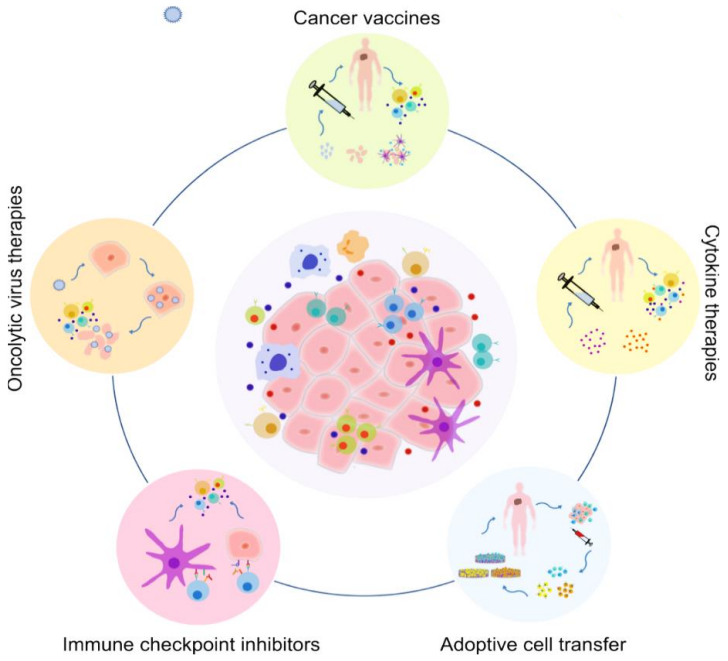

Figure 12. The major categories of immunotherapy.[107]

Immunotherapy was in the first of the top ten scientific breakthroughs in 2013 due to its excellent innovation and efficacy.[75] The characteristics of tumor immunity are slow onset, long time of action, and delayed effect. With the application of immunotherapy, the symptoms can be improved lastingly, to consequently prevent recurrences. The emergence of immunotherapy revolutionized the standard of cancer treatment and the concept of cancer treatment. It is known as the third revolution following traditional chemotherapy drugs and targeted tumor therapy.[108] It kills tumor cells by improving the naive immune response.[109] Moreover, compared with

conventional treatments such as chemotherapy, immunotherapy has significantly improved the frequency and severity of side effects.[110]

Although immune checkpoint inhibitors have shown superior effects beyond conventional therapies in the treatment of many tumors, especially for the treatment of lung cancer, melanoma, and kidney cancer, they have greatly changed the survival rate of patients.[111] However, many years of research have shown that due to the influence of the BBB, drug molecules cannot be concentrated in the GBM tissue, so that the corresponding effect of the tumor on immune checkpoint inhibitors is not ideal. Moreover, GBM has a strong immunosuppressive TME, which limits its response to conventional immunotherapy, so it is called the "desert" of immunotherapy.[112] In recent years, many scientists have tried to use immuno-enhancing therapy drugs to treat this tumor, but they have not achieved the expected results.[113] Therefore, it is urgent to find methods that can enhance the immunogenicity of GBM cells and improve the immunosuppressive properties of the tumor microenvironment.

1.3.4 Photo-immunotherapy

Laser immunotherapy is a new method of comprehensive tumor treatment which combines a specific laser wavelength, photosensitizer, and immune adjuvant.[114] Due to the unique advantages of this therapy in long-term efficacy, it has gradually become a new research hotspot for malignant tumor treatment. The term photo-immunotherapy was firstly proposed by Oklahoma State University in 1997.[115] The basic principle of this therapy is to irradiate the tumor tissue with a semiconductor laser of a specific wavelength through an optical fiber. The immune adjuvant in the tumor tissue can combine with the antigen that released from the destroyed tumor cells to form a vaccine, thereby inducing an immune response against tumor cells, killing the primary tumor cells and metastasis, and generating tumor-specific immunity (as shown in **Figure 13**).[116-119]

Photo-immunotherapy uses the local destruction of laser photothermal and photochemical effects and stimulates the host immune defense system. The treatment uses particular drugs and NIR laser to destroy cancer cells.[120] NIR laser can reach the interior of living tissues without damaging them. By binding the antibody-drug to a specific cell and irradiating it with NIR laser, the cell membrane is destroyed, and all the antibodies are exposed to the immune system, which is super-selective *in vivo*.[121] The tumor microenvironment (TME) has an immune response to the cancer-specific antigen contained in damaged cancer cell fragments, thereby exerting an effect on cancer cells and metastatic cancer cells outside the irradiated area.

Moreover, photo-immunotherapy drugs can also be used as a beneficial supplement to the existing PD-1, PD-L1, or CTLA-4 monoclonal antibodies in enhancing immune response against tumor.[122-126] However, until now, there is little development of such photo-immune drugs for brain cancer treatment.

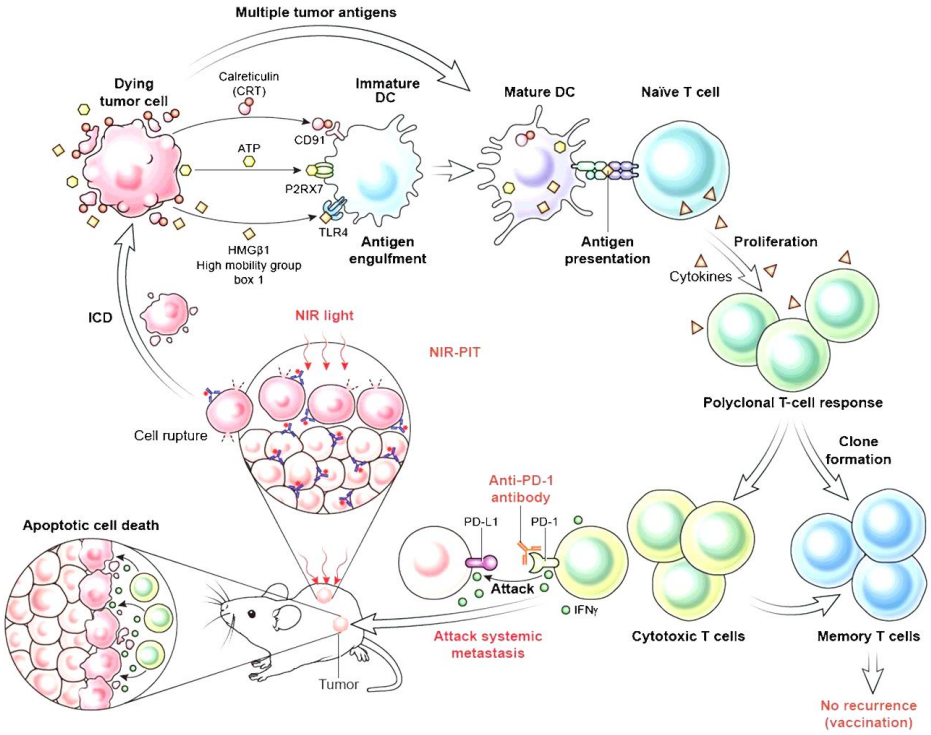

Figure 13. Biology of immunogenic cell death induced by NIR-PTT leads to enhanced antitumor host immunity against treated cancer cells.[116]

2. RAESEARCH OBJECTIVES

The objectives of this thesis has been to explore new ways to (i) deliver NPs across BBB, and (ii) investigate the efficiency of photo-immunotherapy in brain tumors.

Paper I

Biodegradable Polymeric Nanoparticles Containing an Immune Checkpoint Inhibitor (aPDL1) to Locally Induce Immune Responses in the Central Nervous System

To overcome the immunological tolerance of brain tumors, a novel multifunctional NP for highly efficient synergetic immunotherapy is reported. The NP contains an anti-PDL1 antibody (aPDL1), upconverting NPs, and the photosensitizer 5-ALA; the surface of the NP is conjugated with the B1R kinin ligand to facilitate transport across the BBB. Upon irradiation with a 980 nm laser, 5-ALA is transformed into protoporphyrin IX, generating ROS. PDT further promotes intratumoral infiltration of cytotoxic T lymphocytes and sensitizes tumors to PDL1 blockade therapy. It is demonstrated that combining PDT and aPDL1 can effectively suppress GBM growth in mouse models. The proposed NPs provide a novel and effective strategy for boosting anti-GBM photo-immunotherapy.

Paper II

Upregulating Aggregation-Induced-Emission Nanoparticles with Blood Brain Barrier Permeability for Precise Photothermal Eradication of Brain Tumors and Induction of Local Immune Responses

The B1R kinin ligand (Des-Arg9-Kallidin) aggregation-induced-emission (BK@AIE) NPs are synthesized; these offer selective penetration through the BBB and strong absorbance in the NIR. The BK@AIE NPs exhibit high photothermal conversion efficiency under 980 nm NIR laser irradiation, facilitating the treatment of deep-seated tumors. Tumor progression can be effectively inhibited to extend the survival span of mice after spatiotemporal PTT. NIR irradiation can eradicate tumor tissues and release tumor-associated antigens. It is observed that the PTT treatment of GBM-bearing mice activates NK cells, CD3+ T cells, and M1 macrophages in the GBM area increasing the therapeutic efficacy. This study demonstrates that NIR-assisted BK@AIE NPs represent a promising strategy for the improved systematic elimination of GBMs and local brain immune privilege activation.

EPILOUE

The research project presented in this thesis are all concerned with exploring new ways to deliver NPs across BBB and investigating the efficiency of photo-immunotherapy in brain tumors. Numerous efforts have been made to facilitate drug delivery efficiency across the BBB. A popular approach is a receptor-mediated transcytosis.[127-129] The binding of the ligand and receptor promotes endocytosis and the vesicular trafficking machinery helps to transport the drugs across the BBB.[130-132] Well-characterized receptors include the transferrin receptor, insulin-like growth factor, and low-density lipoprotein receptors.[133, 134] However, a significant drawback is that these receptors are universally expressed in normal cell lines and tissues, resulting in unwanted peripheral organ uptake.[135, 136] BR1 is barely detectable under physiological conditions, except in the CNS. Moreover, B1R is overexpressed in major inflammatory pathologies, making it a target for pharmaceuticals.[137, 138] As a result, GBM cells, as well as the surrounding brain capillary endothelial cells, express a high level of B1R.[30] Therefore, we envision that the kinin ligand could bind to B1R on the blood vessel in GBM areas, locally increasing the permeability of the BBB. The transient and localized BBB 'disruption' allows for the effective delivery of NPs to the GBM area.

As the fifth cancer treatment method after surgery, radiotherapy, chemotherapy, and immunotherapy, photo-immunotherapy has been highly anticipated. Since the Ministry of Health, Labour, and Welfare of Japan approved the world's first photo-immunotherapy drug for surgically unresectable malignant tumors of the head and neck in September 2020, researchers have also carried out photo-immunotherapy to treat lung cancer, colorectal cancer, breast cancer, and pancreatic cancer.[139-141] Such clinical trials have given many patients hope for life and expressed their desire to go to Japan for medical treatment. According to the latest report, 20 Japanese hospitals can implement photo-immunotherapy.[142] When a cancer cell ruptures and dies in response to NIR-PIT/PDT, the substances inside the cell will be released, and the nearby immune system will perceive these substances as foreign bodies, destroying the immune cells of the cancer cells, that is, cytotoxic T According to the suppression of other immune cells that control T cells.[143, 144] In mouse experiments, the control T cells were quickly and selectively removed, and it was confirmed that the "cancer noxious T cells" were activated within 1 h. Longevity effect of mice.[145] In other words, activating T cells has a significant immune response from the treated tumor to other tumors. Therefore, the research project in this thesis is concerned with investigating the efficiency of photo-immunotherapy in brain tumors.

With these nanoplatforms, the BBB around the GBM was temporarily opened, obtaining meaningful progress in anti-tumor efficiency by increasing the number of GBM-targeted NPs. Moreover, the excellent NIR laser-induced PDT or PTT effect from NPs leads to serious GBM cell damage, which leads to a stronger immune response by releasing endogenous tumor antigens. The tumoricidal MΦ and NK cells are activated during this process, exacerbating GBM elimination and inducing long-term immune memory. Therefore, the combination of phototherapy and immunotherapy will greatly boost the antitumor immune response and elicit long-term immune memory effects, leading to the inhibition of both primary and metastatic tumors.

In **paper I**, we provide a multifunctional NP based on MUCNP to specifically trigger the brain antitumor immune response via 980 nm laser-mediated PDT. With this nanoplatform, we temporarily opened the BBB around the GBM, obtaining meaningful progress in anti-tumor efficiency by increasing the number of GBM-targeted NPs. Moreover, the excellent NIR laser-induced PDT effect from BK@γ-PGA@5-ALA@MUCNP@aPDL1 NPs leads to serious GBM cell damage, which leads to a stronger immune response by releasing endogenous tumor antigens. Later, the released-aPDL1 from NPs enhanced immune cytokine secretion and recruited CD4+ and CD8+ T cells into GBM, thus enhancing the therapeutic efficacy. In addition, tumoricidal MΦ and NK cells are activated during this process, exacerbating GBM elimination and inducing long-term immune memory. Therefore, we aim to provide a nanoplatform based on PpIX, possessing great photo-immunotherapy potency, eliminating primary GBM, and preventing GBM relapse. This would be a tremendous advance in the clinical treatment of GBM.

In **paper II**, we have developed a multifunctional biocompatible nanoplatform based on BK coated AIE NPs, which could (i) specifically target the brain tumor, (ii) penetrate through the morbid BBB, (iii) perform PTT, and (iv) simultaneously activate the local immune system for a very effective synergetic brain cancer therapy. *In vivo* bimodal fluorescence and MR imaging verified the significant tumor accumulation of BK@AIE NPs. *In vivo* excellent tumor inhibition effect of PTT from BK@AIE NPs was realized by systematic administration of the animal tumor models. With the advantages like the temporary modulation of morbid BBB permeability, GBM cells could be specifically targeted, followed by a rapid increase in the local temperature of the brain tumor with minimal harm to surrounding normal tissue. *In vivo*, BK@AIE NPs-mediated PTT showed a significant effect in both eliminating tumor cells for releasing antigens in the local microenvironment and instigating an inflammatory response for

recruiting immune cells into the region. BK@AIE NPs-mediated PTT is thus an apt tool for activating the immune system of the brain. Moreover, BK@AIE NPs-mediated PTT could eliminate CSCs inside tumors in mouse models, the root of cancer recurrence associated with conventional therapy, for cancer treatment with highly improved efficacy.

Compared with traditional drug delivery systems, nano-drug delivery systems can effectively improve the pharmacokinetics and pharmacodynamic properties of drugs and improve the anti-tumor efficacy. The huge development potential and broad application prospects have attracted widespread attention from the majority of formulation developers and pharmaceutical manufacturers. More and more nano-drugs have begun to enter the stage of clinical trials and enter the market. Although some progress has been made, there is still a lot of work to be done. With further in-depth research on nano-medicine carriers, the potential safety of nanomaterials has always been a hot topic of discussion. Therefore, the design and development of nano-drug carriers with good biodegradability and biocompatibility is an important prerequisite for realizing the industrialization of nano-drug delivery systems. In addition to safety issues, there are fewer types of high-quality excipients (only some lipids and human serum albumin) that have been approved for use in nanomedicine formulations, which greatly limits their further applications. In terms of the preparation process, the technical barriers for the development of nanomedicine are relatively high, the preparation process is complicated and conventional methods cannot be used for monitoring. In addition, the production of nano-formulations usually involves complex multi-unit operations, which are greatly affected by equipment, operating conditions, and process parameters during process scale-up.

In future, more research work is needed to: (i) simplify preparation method of NPs; (ii) further expand the research of different types of brain tumor models, as current tumor animal models are relatively simple; (iii) use a longer wavelength laser light source to achieve the killing of tumors in deep tissues; (iv) use the brain immune system activated by NIR-PTT to further treat brain tumors; (v) to study the ability of the immune system to inhibit the recurrence and metastasis of brain tumors after activation; (vi) evaluate the toxicity of NPs more systematically.

PAPER I

Biodegradable Polymeric Nanoparticles Containing an Immune Checkpoint Inhibitor (aPDL1) to Locally Induce Immune Responses in the Central Nervous System

Adv. Funct. Mater. 2021, 2102274

Biodegradable Polymeric Nanoparticles Containing an Immune Checkpoint Inhibitor (aPDL1) to Locally Induce Immune Responses in the Central Nervous System

Ming Zhang,[a,b] Xuefeng Jiang,[b] Qicheng Zhang,[b] Tao Zheng,[a] Mohsen Mohammadniaei,[a] Wentao Wang,[a] Jian Shen,[b*] and Yi Sun[a*]*

[a]*Department of Health Technology, Technical University of Denmark, Kongens Lyngby, DK-2800, Denmark;*

[b]*Jiangsu Collaborative Innovation Center for Biomedical Functional Materials, School of Chemistry and Materials Science, Nanjing Normal University, Nanjing 210023, P. R. China;*

Corresponding authors: Wentao Wang, wentwa@dtu.dk; Jian Shen, jshen@njnu.edu.cn; Yi Sun, suyi@dtu.dk

Abstract: *Immunotherapy is an efficient approach to clinical oncology. However, the immune privilege of the central nervous system (CNS) limits the application of immunotherapeutic strategies for brain cancers, especially glioblastoma (GBM). Tumor resistance to immune checkpoint inhibitors is a further challenge in immunotherapies. To overcome the immunological tolerance of brain tumors, we report a novel multifunctional nanoparticle (BK@γ-PGA@5-ALA@MUCNP@aPDL1 NPs) for highly efficient synergetic immunotherapy. The NPs contains an anti-PDL1 antibody (aPDL1), upconverting NPs (UCNPs), and the photosensitizer 5-ALA; the surface of the NP is conjugated with the B1R kinin ligand (des-Arg^9-Kallidin) to facilitate transport across the morbid blood brain barrier (BBB). Upon irradiation with a 980 nm laser, 5-ALA is transformed into protoporphyrin IX (PpIX), generating reactive oxygen species (ROS). Photodynamic therapy (PDT) further promotes intratumoral infiltration of cytotoxic T lymphocytes (CTLs) and sensitizes tumors to PDL1 blockade therapy. We demonstrated that combining PDT and aPDL1 could effectively suppress GBM growth in mouse models. The proposed NPs provide a novel and effective strategy for boosting anti-GBM photo-immunotherapy.*

Introduction

Glioblastoma (GBM) is the most aggressive and common form of primary brain tumors in adults.[1-3] Their poor prognosis is mainly due to resistance to therapeutics and second tumor relapse after surgery and treatment, which has remained a significant challenge until now.[4-5] Alternative strategies have been proposed and investigated for treating GBM. Recently, checkpoint blockade has shown huge promise in cancer immunotherapy.[6-7] CTLA-4 blockade

and PD-1/PD-L1 blockade have already been permitted by the U.S. Food and Drug Administration for treating different types of cancers.[8] However, checkpoint inhibitors have shown limited efficiency for GBM, partly because of the poor efficiency of drug delivery across the blood brain barrier (BBB).[9-10] Another major challenge is the immunosuppressive tumor microenvironment (TME), including poor T cell infiltration, excessive tumor-associated macrophages (MΦ), and the expression of immunosuppressive molecules.[11-13] To improve these immunotherapeutic effects in GBM treatment, drugs — such as the anti-PDL1 antibody (aPDL1) — must be efficiently delivered across the BBB. In addition, it is essential to develop intervention strategies to sensitize GBM and convert the immunologically 'cold' environment into a "hot" environment.

Numerous efforts have been made to facilitate drug delivery efficiency across the BBB. A popular approach is receptor-mediated transcytosis.[14-16] In this method, the binding of the ligand and receptor promotes endocytosis and the vesicular trafficking machinery helps to transport the drugs across the BBB.[17-19] Well-characterized receptors include the transferrin receptor, insulin-like growth factor, and low-density lipoprotein receptors.[20-21] However, a significant drawback is that these receptors are universally expressed in normal cell lines and tissues, resulting in unwanted peripheral organ uptake.[22-24] An alternative strategy is to physically/chemically modulate the BBB permeability, potentially allowing for a larger number of therapeutics to be delivered to their target.[25-26]; however, most of these methods are invasive and cause a non-selective increase in permeability throughout the central nervous system (CNS). Kinins were previously found to be natural modulators of vessel permeability but their unique properties have not been well explored for drug delivery. The biological functions of kinins are mediated through the activation of G-protein coupled receptors, referred to as the B1 receptor (B1R) and B2 receptor (B2R). B2R exhibits constitutive expression in numerous tissues.[27, 28] In contrast, BR1 is barely detectable under physiological conditions, except in the CNS. Moreover, B1R is overexpressed in major inflammatory pathologies, making it a target for pharmaceuticals.[29, 30] Interestingly, the inflammatory environment around GBM is beneficial for its growth and angiogenesis.[31] These physiological activities further contribute to activating B1R in the brain tumor microenvironment (TME).[32] As a result, GBM cells, as well as the surrounding brain capillary endothelial cells, express a high level of B1R.[30] Therefore, we envision that the kinin ligand could bind to B1R on the blood vessel in GBM areas, locally increasing the permeability of the BBB. In addition, the kinin ligand can also specifically target GBM cells.[33, 34] Therefore, conjugating the B1R kinin ligand (BK, des-Arg9-

Kallidin) with therapeutics or nanoparticle (NP)-based drug delivery systems would present a completely new method of safe and effective drug delivery to tumors in the CNS.

Combining immune drugs with photodynamic therapy (PDT) based on immune adjuvant NPs could help to inhibit tumor invasion.[35-37] PDT has received great attention in both clinical practices and preclinical studies.[38, 39] During the PDT process, the activated photosensitizer induced by laser irradiation generates reactive oxygen species (ROS), resulting in immunogenic tumor cell death.[40] Thus, coupling PDT with checkpoint inhibitors is promising for boosting immunotherapy in GBM. An ideal photosensitizer can achieve deeper tissue penetration by absorbing light in the far-red wavelengths. Moreover, an ideal photosensitizer candidate would address systemic toxicity via rapid elimination from the body and high tumor tissue selectivity. 5-ALA is a second-generation photosensitizer that is already permitted by the E.U. for the PDT of different types of cancers.[41] It can be converted into the effective photosensitizer, protoporphyrin IX (PpIX), through the endogenous heme pathway.[42] A major advantage of 5-ALA is its selective accumulation in tumor cells, i.e., a higher level of PpIX in tumor sites only. Moreover, PpIX could be rapidly removed from the body while other clinically applied photosensitizers — mainly Phototofrin® or Foscan® — would stay in the body for a much longer period.[41,42] Unfortunately, the blue exciting light for 5-ALA fails to penetrate deep tissue or avoids autofluorescence issues.[43] Comparatively, the wavelength of exciting light for upconverting NPs (UCNPs) can reach 980 nm, which is within the "optical transmission window" for biological tissues, mediating higher tissue penetration and photostability, reducing photodamage, and nonblinking fluorescence, with strongly induced visible to near-infrared (NIR) luminescence signals.[44] Hence, the combination of UCNPs with 5-ALA would achieve PDT in the NIR region.

To address the challenges of current checkpoint blockade therapy in GBM, we present a novel NP platform that can both enhance delivery across the BBB and alter the immunosuppressive TME (**Scheme 1**). aPDL1, 5-ALA, and magnetic UCNP (MUCNP) self-assembled into NPs in the presence of biodegradable poly(γ-glutamic acid) (γ-PGA). BK were then conjugated to the surface to form the final NPs (BK@γ-PGA@5-ALA@MUCNP@aPDL1). The kinin ligand provides the vasculature and tumor-targeting ability. After intravenous injection, the NPs first bind to the B1R, and the enhanced localized accumulation of the NPs induces a series of secondary reactions to expand the permeability of the BBB. Once across the BBB, BK@γ-PGA@5-ALA@MUCNP@aPDL1 can passively accumulate at the tumor site through active B1R targeting and enhance the permeability and

retention (EPR) effect. The released aPDL1 could block the tumor cell surface marker-PDL1 when 5-ALA and MUCNP are endocytosed by GBM cells. Under 980 nm laser excitation, the GBM cells underwent apoptosis due to the produced $^1O_2$. The immunogenic death of tumor cells triggers inflammation, which stimulates TME by promoting increased intratumoral infiltration of cytotoxic T lymphocytes (CTLs) in GBM. NPs may represent a robust platform for overcoming barriers in GBM immunotherapy. The transient and localized BBB 'disruption' allows for the effective delivery of NPs to the GBM area. The combination of PDT and checkpoint inhibitors will greatly boost the antitumor immune response and elicit long-term immune memory effects, leading to the inhibition of brain tumors.

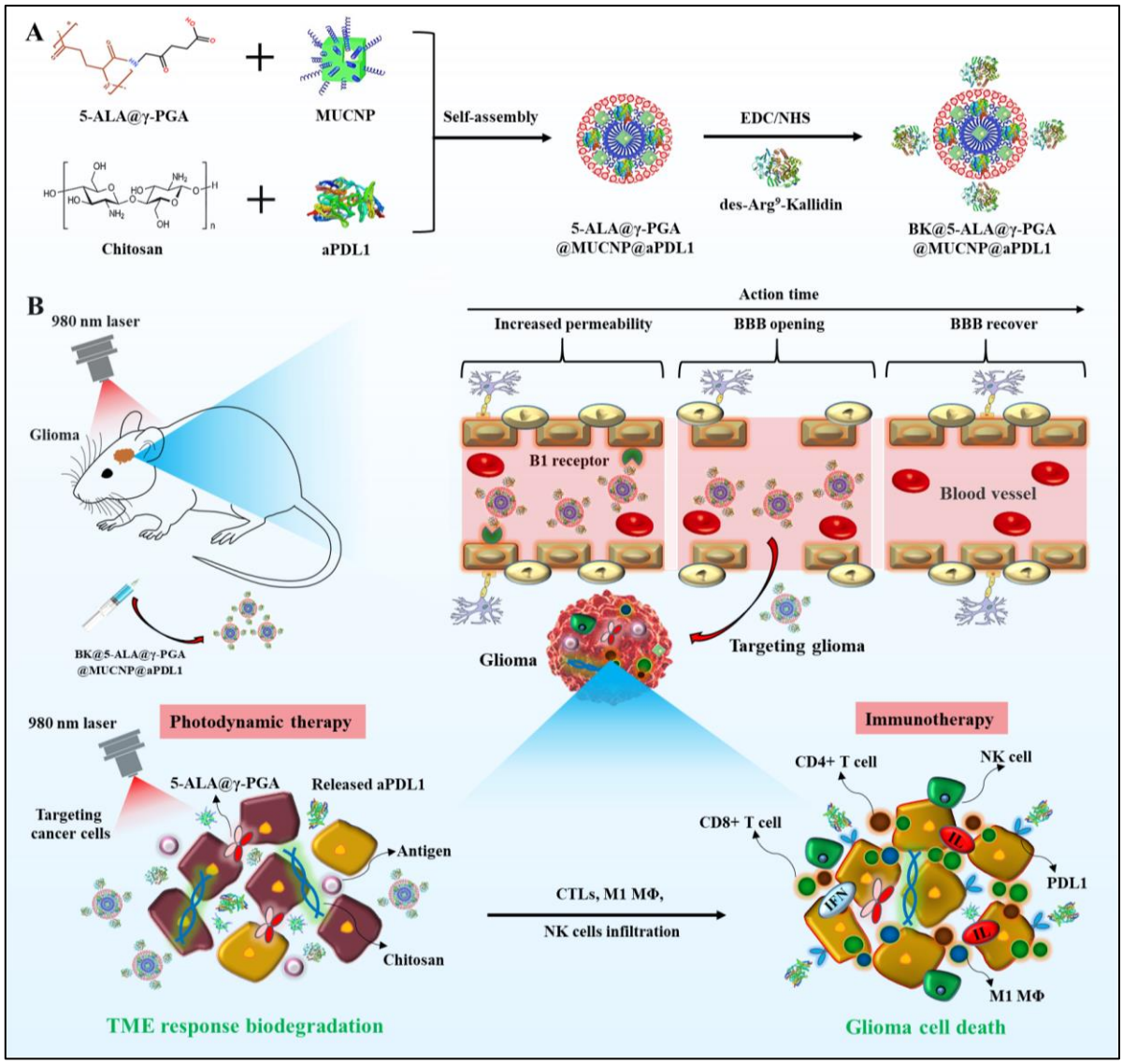

Scheme 1. (A) Schematic diagram of the synthesis process of the BK@γ-PGA@5-ALA@MUCNP@aPDL1 NPs. (B) Schematic illustration of antitumor immune responses induced by BK@γ-PGA@5-ALA@MUCNP@aPDL1− mediated PDT in combination with checkpoint-blockade.

Results and discussion

A biocompatible theranostic agent was designed by integrating mitochondrial-targeting PpIX for synthetic cancer therapy.[42] However, the blue excitation light of PpIX hampers its *in-vivo* applications. To obtain useful UV-visible emission, MUCNP was synthesized as an upconversion energy donor. Furthermore, an Fe_3O_4-based host lattice was employed to support the magnetic resonance (MR) imaging capability by shortening the relaxation time of T2. To prepare MUCNP, oleic acid-capped Fe_3O_4 NPs were synthesized. Subsequently, the as-synthesized OA-Fe_3O_4 was used as the seed on which the upconversion luminescent shell (NaYF4:Yb/Er) could form. The high-resolution transmission electron microscope (HRTEM) image shows that the lattice fringes of UCNP and the Fe_3O_4 core were 0.31 nm and 0.26 nm (**Figure 1A**), respectively, which ascribed to the (111) lattice planes of cubic $NaYF_4$ and (331) lattice planes of the magnetite face-centered cubic structure. This result suggests that the $NaYF_4$:Yb/Er shell was successfully wrapped onto the magnetic seed nanocrystals. As shown in **Scheme 1A**, γ-PGA@5-ALA@MUCNP@aPDL1 instantaneously self-assembled with the addition of aqueous γ-PGA@5-ALA, MUCNP and aPDL1 into the room-temperature chitosan solution. Transmission electron microscope (TEM) was used to observe the morphology of the γ-PGA@5-ALA@MUCNP@aPDL1 (**Figure 1B**). We can see that the cluster structure of the MUCNP can develop after the formation of hybrid NPs and the size of each NP can be estimated as 80 – 120 nm; this agrees well with the diameter of 115 nm measured via dynamic laser scattering (DLS) (**Figure S1**).

To increase the permeability of the BBB and the targeting ability towards GBM cells, BK was modified on the NP surface by the EDC/NHS reaction. The TEM image (**Figure 1C**) shows small changes in the morphology of γ-PGA@5-ALA@MUCNP@aPDL1 after modification by BK. The uniform distribution of Er, Y, and Fe elements was observed in the elemental mapping images (**Figure 1D**), demonstrating successful MUCNP incorporation within the BK@γ-PGA@5-ALA@MUCNP@aPDL1. Moreover, the protein file analysis of aPDL1 specific bands demonstrated efficient aPDL1 loading within the BK@γ-PGA@5-ALA@MUCNP@aPDL1 nanocomposites (**Figure 1E**). aPDL1 retained their PDL1 binding capability when they were compressed into BK@γ-PGA@5-ALA@MUCNP@aPDL1 via western blotting (WB) assay (**Figure 1E**), suggesting that the effect of compression is negligible for impeding the bioactivity of aPDL1. The successful preparation of BK@γ-PGA@5-ALA@MUCNP@aPDL1 was confirmed via its X-ray diffraction (XRD) pattern

(**Figure 1F**), as shown by the diffraction peaks of Fe_3O_4 and UCNPs core-shell structures. Moreover, BK@γ-PGA@5-ALA@MUCNP@aPDL1 exhibited ferromagnetic behavior with a hysteresis loop at 300 K (**Figure 1G**), suggesting that BK@γ-PGA@5-ALA@MUCNP@aPDL1 can be used as a good magnetic resonance (MR) imaging agent. To explore the efficiency of upconversion emission for PDT and *in-vivo* optical bioimaging, the upconversion luminescence (UCL) spectra of BK@γ-PGA@5-ALA@MUCNP@aPDL1 was measured. As shown in **Figure 1H**, the emissions at 500 – 550 nm and 630 – 690 nm were ascribed to the $^2H_{11/2} \rightarrow {}^4I_{15/2}$, $^4S_{3/2} \rightarrow {}^4I_{15/2}$, and $^4F_{9/2} \rightarrow {}^4I_{15/2}$ transitions of Er^{3+} (**Figure S2**), demonstrating efficient energy transfer from MUCNP to PpIX.

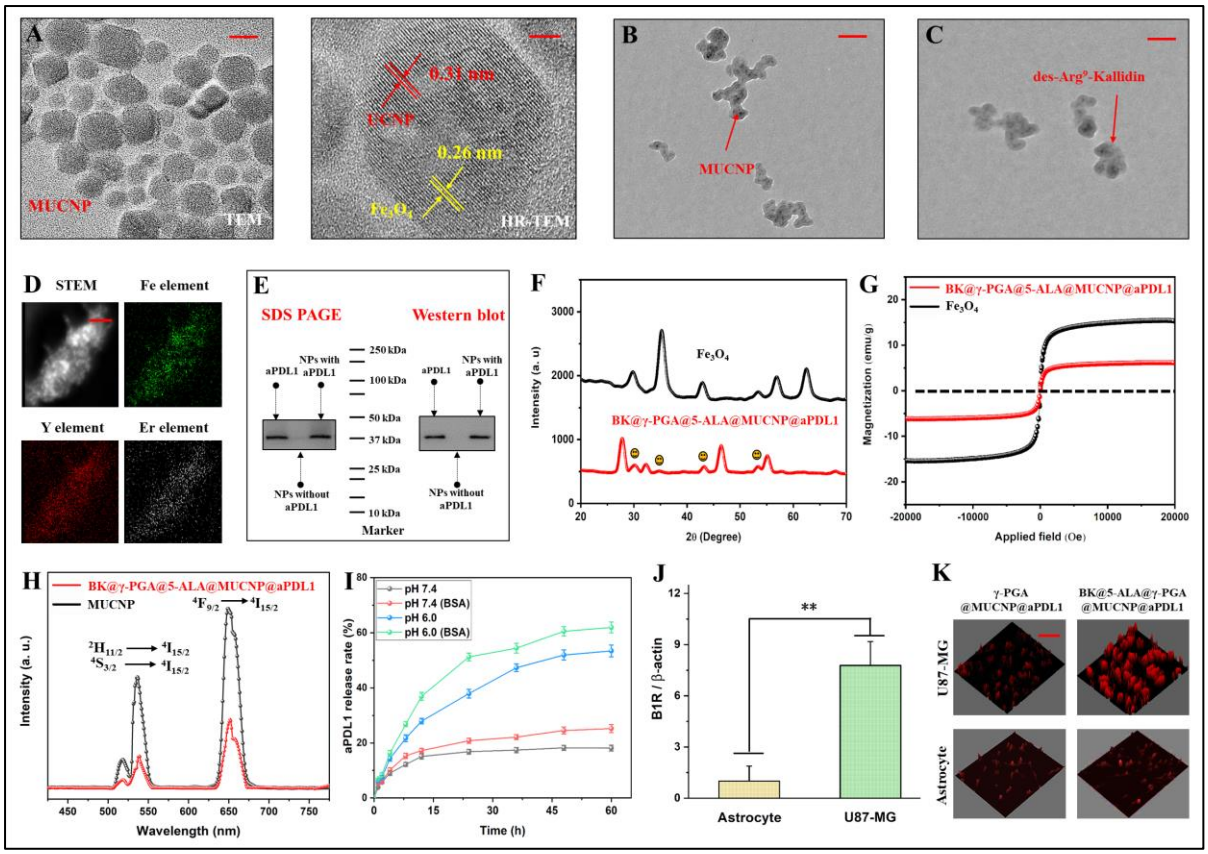

Figure 1. (A) TEM (scale bar: 10 nm) and HRTEM image (scale bar: 1 nm) of MUCNP. (B) TEM image of γ-PGA@5-ALA@MUCNP@aPDL1. Scale bar: 100 nm (C) TEM image of BK@γ-PGA@5-ALA@MUCNP@aPDL1. Scale bar: 100 nm (D) HAADF-STEM image and element mapping of BK@γ-PGA@5-ALA@MUCNP@aPDL1. Scale bar: 100 nm (E) SDS-PAGE gel electrophoresis (left) and WB (right) of αPDL1 in the BK@γ-PGA@5-ALA@MUCNP@aPDL1 solution. (F) XRD spectrum of Fe_3O_4 NPs and BK@γ-PGA@5-ALA@MUCNP@aPDL1. (G) VSM spectra of Fe_3O_4 NPs and BK@γ-PGA@5-ALA@MUCNP@aPDL1. (H) The UCL spectra of the MUCNP and BK@γ-PGA@5-ALA@MUCNP@aPDL1. (I) Time and pH-dependent aPDL1 release profiles of BK@γ-PGA@5-ALA@MUCNP@aPDL1. (J) The expression of B1R in U87-MG cells and astrocytes. $^{**}P < 0.01$. (K) Cellular uptake of the γ-PGA@5-ALA@MUCNP@aPDL1 and BK@γ-PGA@5-ALA@MUCNP@aPDL1 in U87-MG cells and astrocytes. Scale bar: 50 μm

The *in-vitro* release profiles of BK@γ-PGA@5-ALA@MUCNP@aPDL1 were evaluated in different buffers at 37 °C. As shown in **Figure 1I**, the release profile of aPDL1 from BK@γ-PGA@5-ALA@MUCNP@aPDL1 was initially rapid, followed by slower and sustained release under all releasing conditions. After 60 h incubation, aPDL1 in PBS (pH 6.0) was released significantly faster than at pH 7.4; this could be attributed to a significant reduction in the degree of ionization of γ-PGA moieties. *In-vitro* tests were performed in 10 % bovine serum albumin (BSA) to simulate the physiological environment. The slight increase in the release rate in 10 % BSA verified the good colloidal stability of BK@γ-PGA@5-ALA@MUCNP@aPDL1 in a serum-equivalent concentration of BSA.

B1R, a specific biomarker of inflammatory tumor cells, was investigated as the target site of the BK-based NPs (**Figure S3**). As expected, B1R protein expression was significantly higher in U87-MG cells than in astrocytes (**Figure 1J**). To test whether BK@γ-PGA@5-ALA@MUCNP@aPDL1 can specifically target GBM cells, we incubated the NPs with U87-MG cells, which overexpress B1R on their surface and used human astrocytes — with expression of only a few B1R biomarkers — as a control. As an additional control, we also incubated U87-MG cells and astrocytes with γ-PGA@5-ALA@MUCNP@aPDL1 (without the BK targeting molecule) and subjected all groups to the same treatment protocol. Using a confocal laser scanning microscopy (CLSM), we detected strong fluorescence signals in U87-MG cells incubated with BK@γ-PGA@5-ALA@MUCNP@aPDL1 (**Figure 1K**) while there was a weak signal in both the astrocytes and the U87-MG cells incubated with γ-PGA@5-ALA@MUCNP@aPDL1.

5-ALA penetrates non-selectively into cells, where it is metabolized to the active sensitizer PpIX. The distinct activity of the enzymes in the tumor led to a higher PpIX accumulation within the cancer cells than the normal cells (**Figure 2A**). PpIX can generate $^1O_2$ under red light irradiation, which eventually leads to cell apoptosis or necrosis. Therefore, the generation and accumulation of PpIX in cancer cells are important. To investigate the PDT effects of PpIX, DMSO was used to extract the generated PpIX in U87-MG cells. The optical properties of the extracted DMSO solutions were studied using fluorescence spectroscopy and UV-vis. Compared with other groups, strong red fluorescence emission at 635 nm was observed (**Figure 2B**) in the BK@γ-PGA@5-ALA@MUCNP@aPDL1 group, which is a characteristic fluorescence emission of PpIX. Hence, it was testified that PpIX could be generated in U87-MG cells via the treatment of BK@γ-PGA@5-ALA@MUCNP@aPDL1.

In-vitro PpIX generation was also studied using a CLSM. Astrocytes and U87-MG cells were treated with γ-PGA@MUCNP@aPDL1, BK@γ-PGA@MUCNP@aPDL1, 5-ALA, γ-PGA@5-ALA@MUCNP@aPDL1, and BK@γ-PGA@5-ALA@MUCNP@aPDL1. The CLSM results are shown in **Figure 2C**, where the red fluorescence color represents the presence of PpIX. Red fluorescence can hardly be observed in astrocytes (**Figure 2D**), which might be due to the rapid degradation of PpIX in normal cells. For U87-MG cells, obvious red fluorescence was observed after treatment with γ-PGA@5-ALA@MUCNP@aPDL1 and 5-ALA (**Figure 2C**). Even stronger red fluorescence was observed for the U87-MG cells in the BK@γ-PGA@5-ALA@MUCNP@aPDL1 group than in the γ-PGA@5-ALA@MUCNP@aPDL1 and 5-ALA groups, indicating that more 5-ALA was delivered into cells based on the polymer nanocarriers that contributed to generating massive PpIX. Next, the efficiency of PpIX generation from this drug delivery system via U87-MG cells was investigated. As shown in **Figure 2E**, the red fluorescence intensity of PpIX in the BK@γ-PGA@5-ALA@MUCNP@aPDL1 group was higher than that in the γ-PGA@5-ALA@MUCNP@aPDL1 group, indicating that more PpIX was generated by treatment with BK@γ-PGA@5-ALA@MUCNP@aPDL1. Furthermore, the U87-MG cells exhibited intense fluorescence signals in the yellow fluorescence (merged channel), demonstrating that PpIX was mainly localized in the mitochondria of U87-MG cells. The sectional TEM image in **Figure 2F** confirms that BK@γ-PGA@5-ALA@MUCNP@aPDL1 accumulated in the tumor cells and its distribution was mostly uniform throughout the cytoplasm. Therefore, these results indicate that PpIX originated from the cytoplasm rather than the nucleus or cell membrane.

The biocompatibility of BK@γ-PGA@5-ALA@MUCNP@aPDL1 was also investigated using red blood cell (RBC) shapes, hemolysis assay, and methyl thiazolyl tetrazolium (MTT) assay. The photomicrographs in **Figure 2G** indicate that the shape of erythrocytes in the test blood did not change after treatment with BK@γ-PGA@5-ALA@MUCNP@aPDL1, no significant hemolysis was observed when RBCs were co-cultured with BK@γ-PGA@5-ALA@MUCNP@aPDL1 (**Figure 2H**). Next, negligible toxicity was observed in U87-MG cells treated with BK@γ-PGA@5-ALA@MUCNP@aPDL1 even at the highest concentration of 5-ALA (15 μg/mL), indicating good biocompatibility of BK@γ-PGA@5-ALA@MUCNP@aPDL1 (**Figure 2I**). These results suggest that BK@γ-PGA@5-ALA@MUCNP@aPDL1 had insignificant cytotoxicity and possessed good hemocompatibility *in-vitro*.

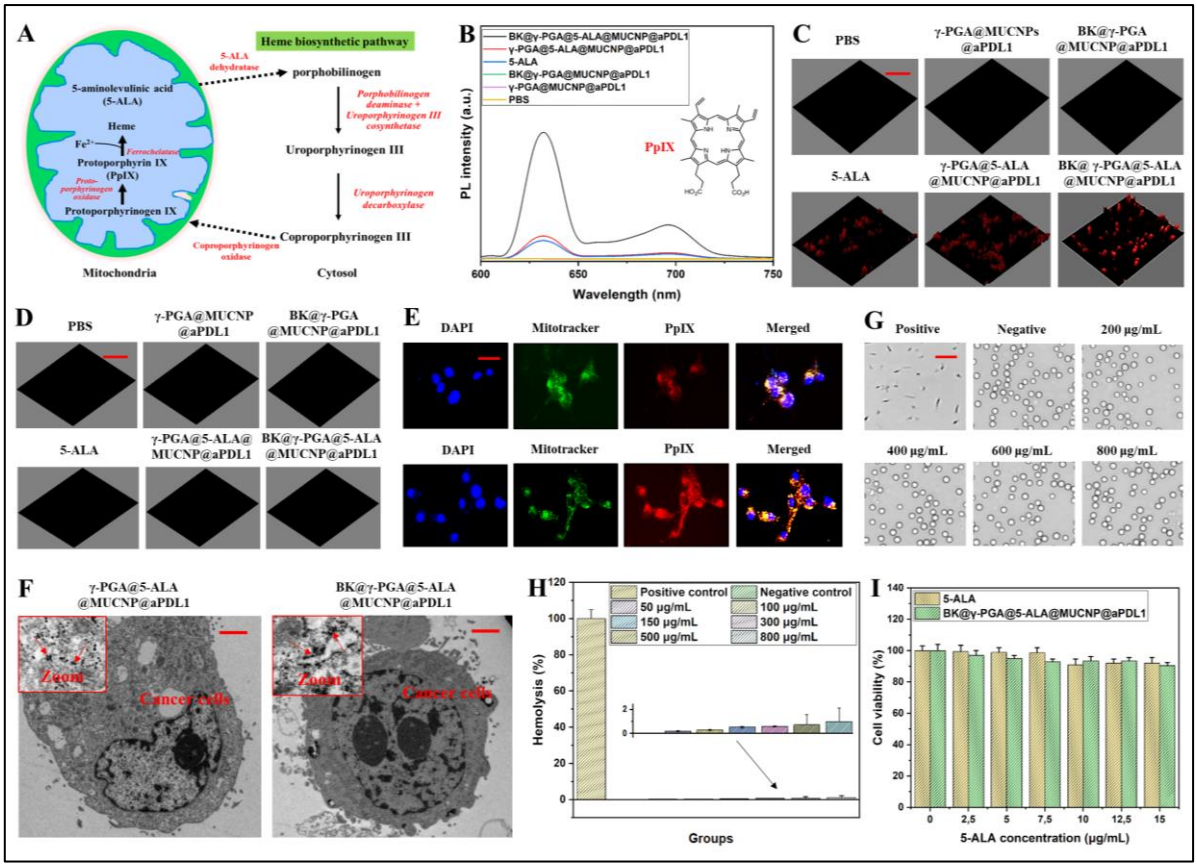

Figure 2. (A) Schematic diagram of the heme biosynthetic pathway of PpIX. (B) The fluorescence emission spectrum of PpIX extracted from U87-MG cells. Confocal images of U87-MG cells (C) and astrocytes (D) treated with different solutions. Scale bar: 100 μm (E) CLSM images show the cellular localization of PpIX after γ-PGA@5-ALA@MUCNP@aPDL1 (upper) and BK@γ-PGA@5-ALA@MUCNP@aPDL1 (bottom) treatments. Scale bar: 30 μm (F) Cross-section TEM images of U87-MG cells incubated with γ-PGA@5-ALA@MUCNP@aPDL1 and BK@γ-PGA@5-ALA@MUCNP@aPDL1. Scale bar: 1 μm RBCs shapes (G) and hemolysis percentage of RBCs (H) after treated with different solutions. Scale bar: 15 μm (I) Cell viability assay of U87-MG cells after BK@γ-PGA@5-ALA@MUCNP@aPDL1 and 5-ALA treatment.

The photoactivity of BK@γ-PGA@5-ALA@MUCNP@aPDL1 was evaluated by testing $^1O_2$ generation under 635 nm and 980 nm laser irradiation. The intracellular $^1O_2$-generation capability of BK@γ-PGA@5-ALA@MUCNP@aPDL1 was tested via electron spin resonance (ESR) spectroscopy. A characteristic spin adduct of $^1O_2$ is observed (**Figure S4**), suggesting that $^1O_2$ was generated from BK@γ-PGA@5-ALA@MUCNP@aPDL1. In the control experiments of TEMPO-incubated PpIX with a 980 nm laser, the characteristic $^1O_2$ peaks remained unchanged. This observation illustrated that $^1O_2$ could be generated from the cooperation of MUCNP and 5-ALA via an efficient energy transfer process. Furthermore, the intracellular $^1O_2$ generation of BK@γ-PGA@5-ALA@MUCNP@aPDL1 was investigated using a $^1O_2$ sensor green (SOSG) probe. As shown in **Figure 3A**, only weak green fluorescence

was shown in the U87-MG cells incubated with 5-ALA upon 635 nm laser irradiation. In contrast, strong fluorescence was observed in the cells incubated with BK@γ-PGA@5-ALA@MUCNP@aPDL1 upon 635 nm or 980 nm laser irradiation, suggesting that targeting BK@γ-PGA@5-ALA@MUCNP@aPDL1 could largely enhance the cellular uptake by GBM cells.

As BK@γ-PGA@5-ALA@MUCNP@aPDL1 could generate $^1O_2$ under a 980 nm laser, we further detected its antitumor efficiency against U87-MG cells *in-vitro* (**Figure S5**). Calcein AM (living cell, green)/PI (dead cell, red) co-staining (**Figure 3B**) and MTT (**Figure S6**) were used to assess cell viability after PDT. Cell apoptosis occurred after 5-ALA exposure to the 635 nm laser while the well-displayed green fluorescence in other treatment groups presented a good cell survival situation. All of the cells treated with BK@γ-PGA@5-ALA@MUCNP@aPDL1 were killed when irradiated with a 635 nm or 980 nm laser, as indicated by the intense homogeneous red fluorescence. Subsequently, the photocytotoxicity of 5-ALA in BK@γ-PGA@5-ALA@MUCNP@aPDL1 at different concentrations was evaluated using the MTT assay in U87-MG cells. Under laser irradiation at 635 nm for 10 min, the cell viability decreased with increasing 5-ALA concentration, for both BK@γ-PGA@5-ALA@MUCNP@aPDL1 and 5-ALA (**Figure S7**). The half-maximal inhibitory concentration (IC50) for BK@γ-PGA@5-ALA@MUCNP@aPDL1 (5 μg/mL) was found to be lower than that of free 5-ALA (10 μg/mL). Thus, the enhanced photocytotoxicity of BK@γ-PGA@5-ALA@MUCNP@aPDL1 agrees with the increased PpIX formation in U87-MG cells. The concentration-dependent photodynamic cytotoxicity was further investigated after incubation of U87-MG cells with BK@γ-PGA@5-ALA@MUCNP@aPDL1 at different concentrations by flow cytometry (**Figure 3C**). Concentration-dependent cytotoxicity, with viabilities of 14.3 – 94.5 %, was revealed when U87-MG cells were treated with BK@γ-PGA@5-ALA@MUCNP@aPDL1 in conjunction with 980 nm laser irradiation, indicating high anticancer efficiency.

Similar to many other indices, mitochondrial dysfunction has been identified as a functional marker of cell apoptosis. Therefore, the dysfunction of mitochondria in U87-MG cells caused by BK@γ-PGA@5-ALA@MUCNP@aPDL1 under 980 nm laser irradiation was examined before further evaluation of the *in-vitro* PDT efficacy. Mitochondrial membrane potential (MMP) was used to monitor the degree of damage by staining with JC-1 (**Figure 3D**). The reduction in MMP always replies to the gathering of JC-1 monomer (green fluorescence) while the aggregation of JC-1 (red fluorescence) responds to a high MMP, indicating a standard

state. Moreover, the fluorescent shift of JC-1 from orange to green represents the occurrence of early apoptosis. Cells treated with PBS, BK@γ-PGA@5-ALA@MUCNP@aPDL1, and 5-ALA without laser irradiation exhibited strong red fluorescence in the merged images (**Figure 3D**), indicating that very little MMP change occurred in U87-MG cells. However, the significantly increased green fluorescence in cells treated with BK@γ-PGA@5-ALA@MUCNP@aPDL1 under 980 nm or 635 nm laser irradiation, suggesting that the mitochondria were damaged with a reduction in MMP. Furthermore, with 980 nm or 635 nm laser alone, most of the cells showed red fluorescence, suggesting that laser irradiation does not result in mitochondrial damage. Hence, we concluded that the ROS from BK@γ-PGA@5-ALA@MUCNP@aPDL1 in conjunction with 980 nm laser excitation accounted for the mitochondrial dysfunction, indicating that this system could lead to an efficient antitumor process through targeted PDT and enhanced cell apoptosis.

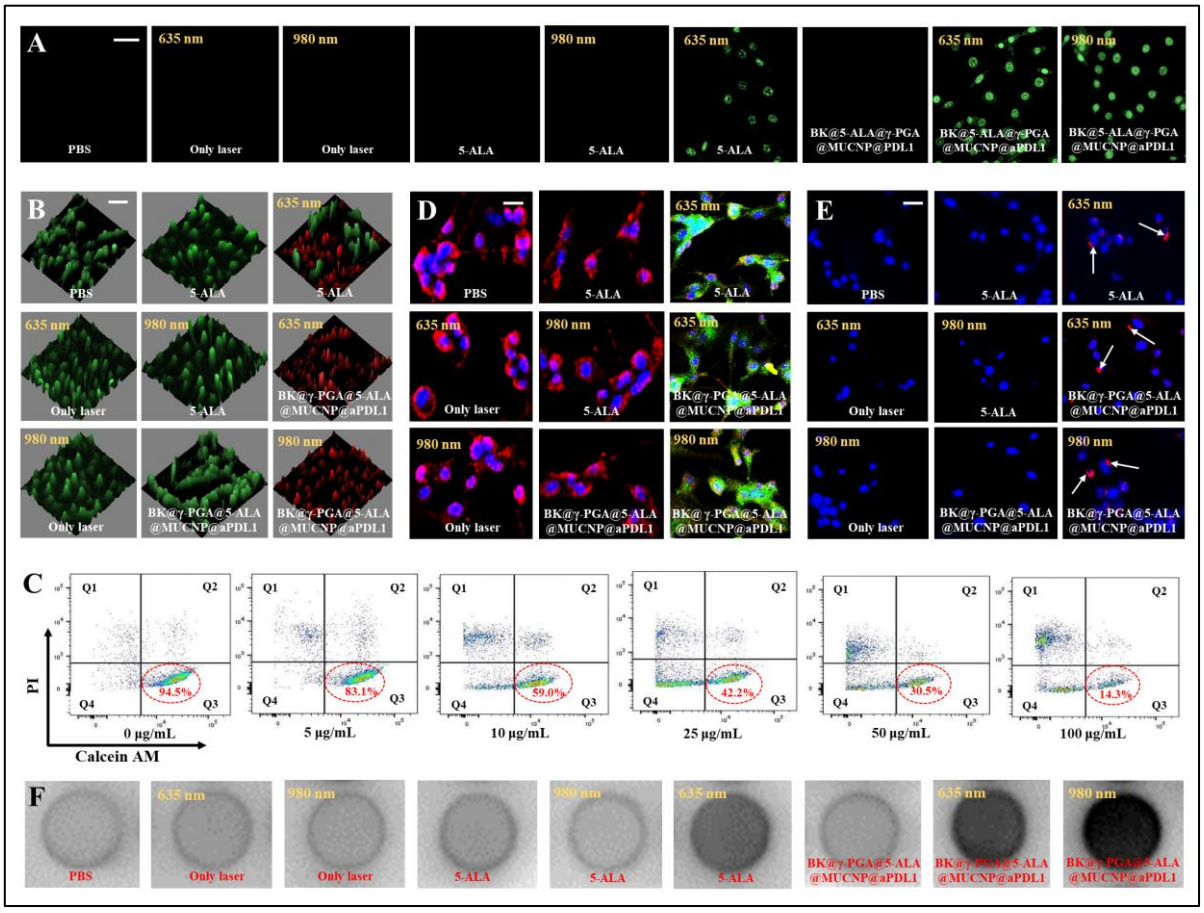

Figure 3. (A) SOSG probe detection of intracellular $^1O_2$ with different samples. Scale bar: 100 μm (B) The antitumor efficiency against U87-MG cells post various treatments. Scale bar: 100 μm (C) The viability of U87-MG cells was quantified by flow cytometry. (D) The mitochondrial potential changes after various treatments. Scale bar: 20 μm (E) CRT expression of U87-MG cells after various treatments. Scale bar: 30 μm (F) The 8-oxoG levels in total genomic DNA were tested by dot blot assay after different treatments.

Recently, immunogenic cell death (ICD) has been used to describe the state of immunogenic apoptosis and active immune response. A characteristic of ICD is the increased surface exposure of calreticulin proteins (CRT) following extensive damage. As a result, CRT exposure serves as a phagocytic calling signal to provoke an internal immune response. By assessing the fluorescent signals of CRT exposure in U87-MG cells, we found that the strongest CRT signals were detected in the cells incubated with BK@γ-PGA@5-ALA@MUCNP@aPDL1 upon 635 nm or 980 nm laser irradiation (**Figure 3E**). These results demonstrate that BK@γ-PGA@5-ALA@MUCNP@aPDL1 based PDT can induce apoptosis in U87-MG cells by enhancing the release of damage-associated molecular patterns. Moreover, 8-oxoguanine (8-oxoG), one of the most common oxidative DNA lesions in mammalian cells, is used as a biomarker to evaluate the degree of oxidative damage. Based on previous results, we further tested whether the formation of 8-oxoG partly accounted for cancer cell elimination induced by the generated $^1O_2$. Indeed, when the cells treated with BK@γ-PGA@5-ALA@MUCNP@aPDL1 were irradiated with 635 nm or 980 nm light, significantly higher levels of 8-oxoG were generated compared to the other groups (**Figure 3F**), suggesting more serious global genomic DNA damage. Defects in DNA damage are closely associated with apoptosis. In summary, the simultaneous occurrence of mitochondrial dysfunction and DNA damage from BK@γ-PGA@5-ALA@MUCNP@aPDL1 treatment could synergistically enhance antitumor efficacy.

To examine the effects of BK@γ-PGA@5-ALA@MUCNP@aPDL1 on MΦ phenotype and function, *in-vitro* RAW 264.7 cells were used as these MΦ express high PDL1. We observed that MΦ cultured with aPDL1 and BK@γ-PGA@5-ALA@MUCNP@aPDL1 were more numerous and larger than those of the other treatments (**Figure S8**). Furthermore, EdU-Alexa Fluor staining was used to assess the proliferation of MΦ following different treatments. After 24 h exposure to aPDL1 and BK@γ-PGA@5-ALA@MUCNP@aPDL1, the number of dividing cells substantially increased in RAW 264.7, as evidenced by the increased red fluorescence and nuclei (**Figure S9**). Live-cell observation of MΦ cultured with aPDL1 and BK@γ-PGA@5-ALA@MUCNP@aPDL1 demonstrated that MΦ size continuously increased over 48 h (**Figure S10**). We next determined whether BK@γ-PGA@5-ALA@MUCNP@aPDL1 treatment activated MΦ by measuring the levels of the costimulatory molecules CD86 and MHC II. MΦ in aPDL1 and BK@γ-PGA@5-ALA@MUCNP@aPDL1 treated groups were higher than those in the other treatments (**Figure 4A**). Moreover, aPDL1

and BK@γ-PGA@5-ALA@MUCNP@aPDL1 treatment upregulated the signals of TNFα and IL12 (**Figure 4B**), indicating the production of inflammatory MΦ.

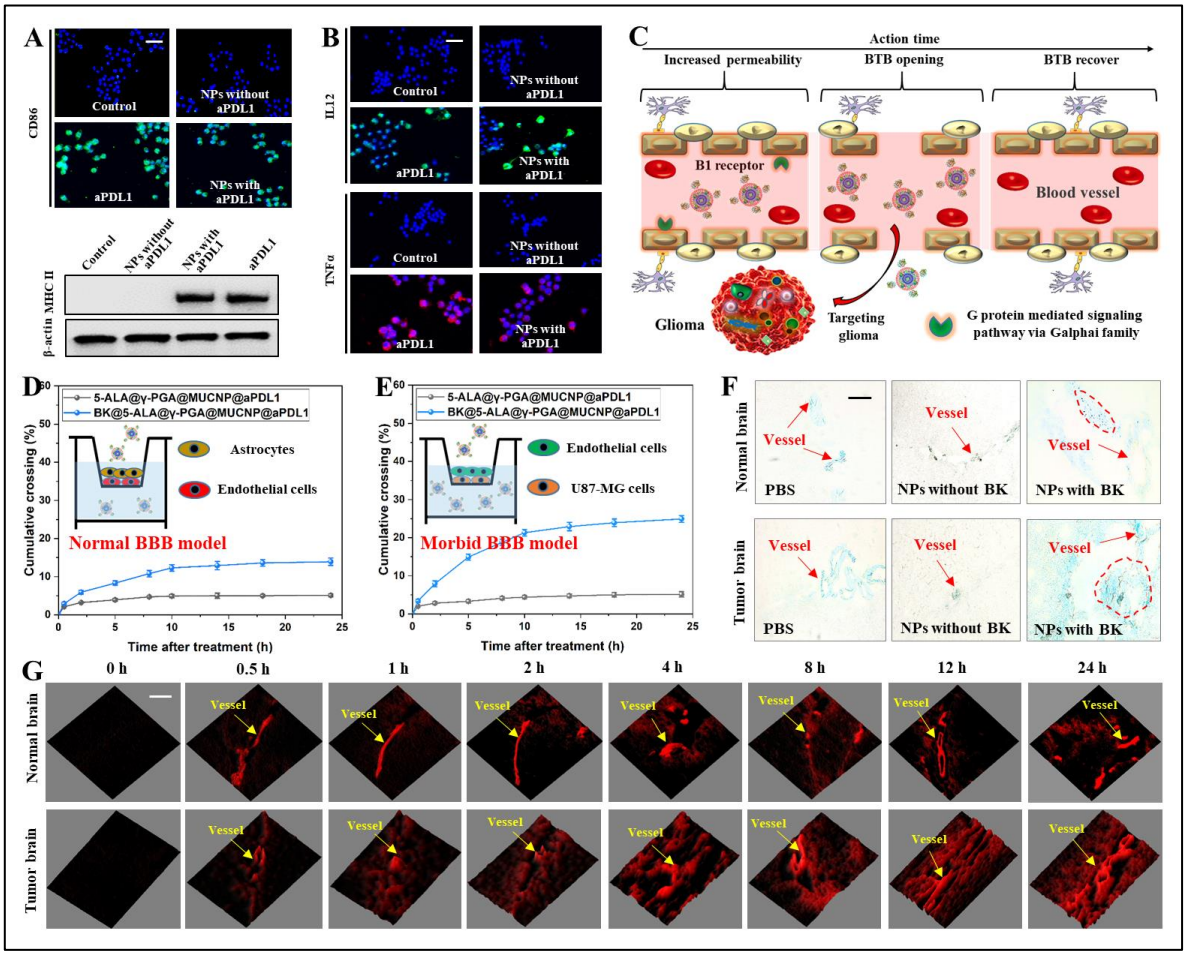

Figure 4. (A) MΦ were stained for stimulatory CD86 expression by the immunofluorescence assay after different treatments. Scale bar: 30 μm The stimulatory MHC II expression was detected by WB assay. (B) The stimulatory IL12 and TNFα expression were detected using the immunofluorescence assay. (C) Schematic illustration of BK@γ-PGA@5-ALA@MUCNP@aPDL1 NPs crossing the morbid BBB. Evaluating normal BBB (D) and morbid BBB (E) crossing dynamics of γ-PGA@5-ALA@MUCNP@aPDL1 or BK@γ-PGA@5-ALA@MUCNP@aPDL1. (F) Evaluating normal BBB and morbid BBB opening status after addition of γ-PGA@5-ALA@MUCNP@aPDL1 or BK@γ-PGA@5-ALA@MUCNP@aPDL1 by EB diffusion experiment. Scale bar: 100 μm (G) UCL images of cerebrovascular in normal and U87-MG tumor-bearing mice after intravenous injection of BK@γ-PGA@5-ALA@MUCNP@aPDL1. Scale bar: 100 μm

B1R in our system was applied to extend the intercellular space within brain capillaries and vascular endothelial cells as it is ubiquitously expressed in brain capillary endothelial cells.[39] Therefore, NPs labeled with B1R-activating kallidin can efficiently breach the normal BBB or morbid BBB *in-vivo* (**Figure 4C**). An *in-vitro* normal BBB model was constructed to assess the normal BBB penetrating capacity of BK@γ-PGA@5-ALA@MUCNP@aPDL1. The fluorescence intensity of solutions in the basal chamber acted as indications for the passing

rates through the BBB during 24 h, which was used to quantitatively evaluate the BK-mediated crossing dynamics (**Figure 4D**). The results showed that BK@γ-PGA@5-ALA@MUCNP@aPDL1 could increase the passing rate by momentarily increasing BBB permeability. The human umbilical vascular endothelial cells (HUVECs)/U87-MG cells co-culture model was established to mimic the other major physiologic obstacle-morbid BBB for GBM during the drug delivery process. When co-cultured, U87-MG cells could stimulate HUVECs to exhibit angiogenic characteristics. As shown in **Figure 4E**, the total transfer percentage of BK@γ-PGA@5-ALA@MUCNP@aPDL1 was 3.9-fold higher than that of γ-PGA@5-ALA@MUCNP@aPDL1. Based on the experimental results of the normal BBB and morbid BBB penetrating capacity, BK-modified NPs possessed better penetration capacity of morbid BBB than normal BBB due to the overexpression of B1R in the U87-MG cell membrane.

To investigate the *in-vivo* efficiency of BK@γ-PGA@5-ALA@MUCNP@aPDL1-induced morbid BBB-opening, normal mice (normal BBB) and mice bearing GBM (morbid BBB) were treated with Evans blue (EB). When administered with PBS and γ-PGA@5-ALA@MUCNP@aPDL1, EB could not cross the normal BBB or morbid BBB. Part of the EB can seep out of the normal mouse blood vessels when administered with BK@γ-PGA@5-ALA@MUCNP@aPDL1. However, when EB and BK@γ-PGA@5-ALA@MUCNP@aPDL1 were administered together, the GBM was stained blue, as indicated by the intense homogeneous blue dye on the outside of the vasculature (**Figure 4F**). This demonstrated that BK was appropriate for selectively opening the morbid BBB or normal BBB. However, BK-modified NPs possessed a better penetration capacity of morbid BBB than normal BBB due to the overexpression of B1R in brain tumor tissues (**Figure S11**). We also used UCL imaging to monitor BK@γ-PGA@5-ALA@MUCNP@aPDL1 distribution in vascular tissues. There was a weak UCL signal outside of the normal mouse brain vasculature when administered with BK@γ-PGA@5-ALA@MUCNP@aPDL1. However, strong UCL outside of the vasculature was observed in U87-MG tumor-bearing mice when the mice were administered BK@γ-PGA@5-ALA@MUCNP@aPDL1 (**Figure 4G**), in accordance with the results of the EB staining. These results indicate that BK@γ-PGA@5-ALA@MUCNP@aPDL1 accumulated well in the brain tissues of U87-MG tumor-bearing mice.

To ensure that the brain tumor animal model was successfully established, brain tissue was extracted from normal mice and tumor-bearing mice to perform the hematoxylin and eosin (H&E) analysis. The highly angiogenic and hemorrhagic features indicated a GL261-implanted

tumor model (**Figure 5A**). Once γ-PGA@5-ALA@MUCNP@aPDL1 and BK@γ-PGA@5-ALA@MUCNP@aPDL1 were intravenously injected into GBM-bearing mice, UCL images were recorded at 24 h. BK@γ-PGA@5-ALA@MUCNP@aPDL1 was most highly localized in the brain region of mice at 24 h after intravenous injection compared to the γ-PGA@5-ALA@MUCNP@aPDL1 group (**Figure 5B**). The average UCL intensity in the tumor of BK@γ-PGA@5-ALA@MUCNP@aPDL1-treated mice was 3.1-fold higher than that of γ-PGA@5-ALA@MUCNP@aPDL1-treated mice (**Figure S12**), indicating the superior homotypic targeting ability of BK@γ-PGA@5-ALA@MUCNP@aPDL1 to GBM. To evaluate targeting efficiency, the fluorescence intensity of the tumor site was monitored after intravenous injections at different time points. Brains were collected and histopathological sections were visualized using a CLSM. Over 24 h, we observed that BK@γ-PGA@5-ALA@MUCNP@aPDL1 displayed better GBM-targeted ability in GL261 tumor-mice compared to γ-PGA@5-ALA@MUCNP@aPDL1 (**Figure 5C**), which agreed with the *in-vivo* results. These results indicate that BK@γ-PGA@5-ALA@MUCNP@aPDL1 could activate the B1R on the BBB to allow for more efficient self-passage and accumulation in the tumor.

The signal contrast enhancement performance of BK@γ-PGA@5-ALA@MUCNP@aPDL1 was evaluated using a small animal MR imager. A significant decline in T2 signal intensity was observed when the concentration of Fe constantly decreased (**Figure 5D**). By utilizing the superparamagnetic and tumor-targeting properties of BK@γ-PGA@5-ALA@MUCNP@aPDL1, *in-vivo* MR imaging of tumor-bearing mice was investigated. After the mice were treated with γ-PGA@5-ALA@MUCNP@aPDL1 and BK@γ-PGA@5-ALA@MUCNP@aPDL1 for 24 h, a more obvious darkening effect at the tumor site was observed in the BK@γ-PGA@5-ALA@MUCNP@aPDL1 group (**Figure 5E**); this demonstrates that the synthesized BK@γ-PGA@5-ALA@MUCNP@aPDL1 could be a candidate as a T2-weighted contrast agent. Fe levels in the main organs at 24 h post-injection of γ-PGA@5-ALA@MUCNP@aPDL1 and BK@γ-PGA@5-ALA@MUCNP@aPDL1 were tested via inductively coupled plasma mass spectrometry (ICP-AES). γ-PGA@5-ALA@MUCNP@aPDL1 could hardly be detected in the brain because of the existence of the BBB (**Figure 5F**) while BK modification increased drug accumulation to a greater extent because NPs could traverse the BBB by receptor-mediated permeation. *In-vivo* PpIX generation was also investigated using a small animal fluorescence imaging system. The fluorescent signals in the GBM sites increased over time and reached a maximum at 20 h post-injection (**Figure 5G**), which could be attributed to the time-consuming biosynthetic pathway

of PpIX. The distribution of PpIX in mouse organs was quantified by *ex vivo* imaging after treatment with BK@γ-PGA@5-ALA@MUCNP@aPDL1. The photograph and tissue sections of different organs showed a strong PpIX fluorescent signal distributed in the tumor other than in other tissues (**Figure 5G, H**). As shown in **Figure S13**, the blood accumulation level of BK@γ-PGA@5-ALA@MUCNP@aPDL1 decreased gradually over time. The BK@γ-PGA@5-ALA@MUCNP@aPDL1 signals in the blood remained at a reasonably high level even 24 h post-injection.

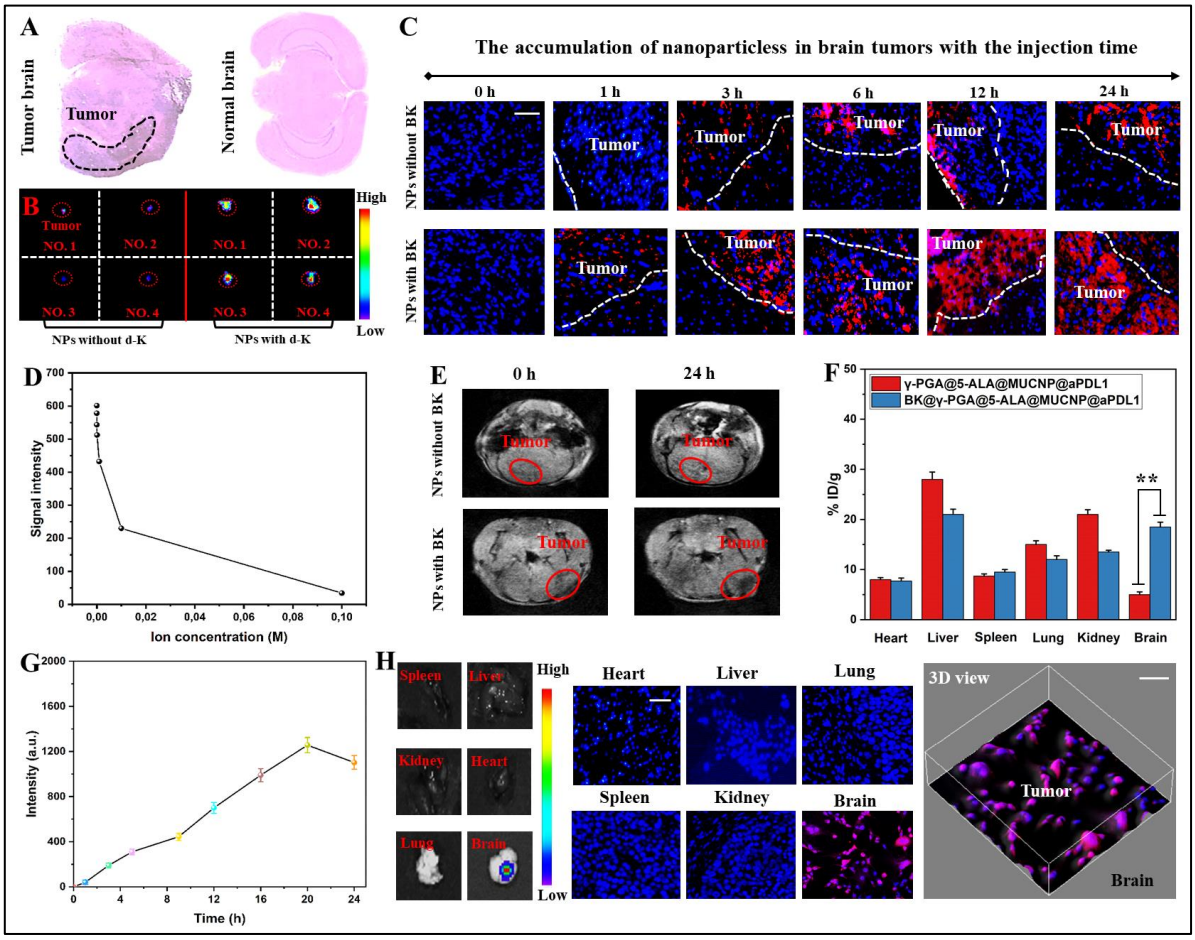

Figure 5. (A) H&E staining of brains from the GL261 tumor-bearing and normal mice. (B) UCL images of tumor after 24 h intravenous injection of γ-PGA@5-ALA@MUCNP@aPDL1 and BK@γ-PGA@5-ALA@MUCNP@aPDL1. (C) UCL images of tumor biopsies after intravenous injection of γ-PGA@5-ALA@MUCNP@aPDL1 and BK@γ-PGA@5-ALA@MUCNP@aPDL1. Scale bar: 100 μm (D) The T2 MR signal intensity is affected by the Fe concentrations of BK@γ-PGA@5-ALA@MUCNP@aPDL1. Inset: A representative T2 weighted MR image of BK@γ-PGA@5-ALA@MUCNP@aPDL1. (E) *In vivo* T2-weighted MR image of a tumor-bearing mouse brain after intravenous injection of γ-PGA@5-ALA@MUCNP@aPDL1 and BK@γ-PGA@5-ALA@MUCNP@aPDL1. (F) Fe detected in the γ-PGA@5-ALA@MUCNP@aPDL1 and BK@γ-PGA@5-ALA@MUCNP@aPDL1 groups. $^{**}P < 0.01$. (G) Average FL intensities from the tumor area after tail vein injection during 24 h. (H) *Ex vivo* fluorescent images of main organs slice at 24 h post-injection. Scale bar: 50 μm

Next, we evaluated the antitumor efficacy of BK@γ-PGA@5-ALA@MUCNP@aPDL1 in a GL261 tumor-bearing C57BL/6 mouse model. To highlight the prominent functions of our treatment strategy, we allocated various treatments: group 1, PBS; group 2, aPDL1; group 3, BK@γ-PGA@5-ALA@MUCNP; group 4, BK@γ-PGA@5-ALA@MUCNP plus 980 nm laser; group 5, BK@γ-PGA@5-ALA@MUCNP@aPDL1; and group 6, BK@γ-PGA@5-ALA@MUCNP@aPDL1 plus 980 nm laser. The photoactivity of BK@γ-PGA@5-ALA@MUCNP@aPDL1 *in-vivo* was examined using dichlorofluorescein diacetate (DCF) as an $^1O_2$ indicator. Groups 4 and 6 demonstrated the appearance of highly diffuse green fluorescence of DCF upon 980 nm laser illumination of the tumor sections, suggesting PDT-triggered $^1O_2$ generation in tumor tissues while low green fluorescent signals indicated no harmful $^1O_2$ (**Figure 6A**).

Subsequently, mouse brain tumors were harvested after various treatments to analyze the local immune response. By recording the quantitated analysis and fluorescent signals in brain tumor tissues, we observed that the number of CD8+ T cells sharply increased with the combined treatment, clearly indicating that the combined treatment was a potent strategy for recruiting CD8+ T cells into GBM (**Figure 6B**). Despite this, by measuring the percentage of CD4+ T cells, we observed that CD4+ cells in the treated groups also increased compared to the control group (**Figure 6C**), leading to a potential increase in regulatory T cells (Tregs). Fortunately, the CD8+ T cell-to-Treg ratio in group 6 was determined to be higher than in groups 4 or 5, implying that BK@γ-PGA@5-ALA@MUCNP@aPDL1-based photo-immunotherapy significantly elicited antitumor immunity. Delivery of aPDL1 checkpoint inhibitor and activation of CNS immunity significantly reprogramed tumor MΦ. In addition to MΦ, natural killer (NK) cells, another tumor killer, were also measured by flow cytometry. As expected, both MΦ and NK cells exhibited higher amounts in groups 5 and 6 than in other groups (**Figure 6D, E**). In particular, M1 MΦ-generated iNOS was responsible for the tumoricidal effect. Therefore, the level of iNOS as an antitumor marker was also measured in tumor slices after various treatments (**Figure S14**). iNOS signals were higher after treatment with BK@γ-PGA@5-ALA@MUCNP@aPDL1 in conjunction with laser irradiation compared with the other groups. Moreover, these activated immunocytes promoted the antitumor effect by producing more inflammatory cytokines in the tumor area. By detecting the levels of serum cytokines by multiplex assays, we found that the treatment in group 6 generated the most cytokines compared to the other groups, such as IL1β, IL12, TNFα, and IFN-γ (**Figure S15**).

These results strongly support the high capacity of the combined treatment to activate systemic immunity.

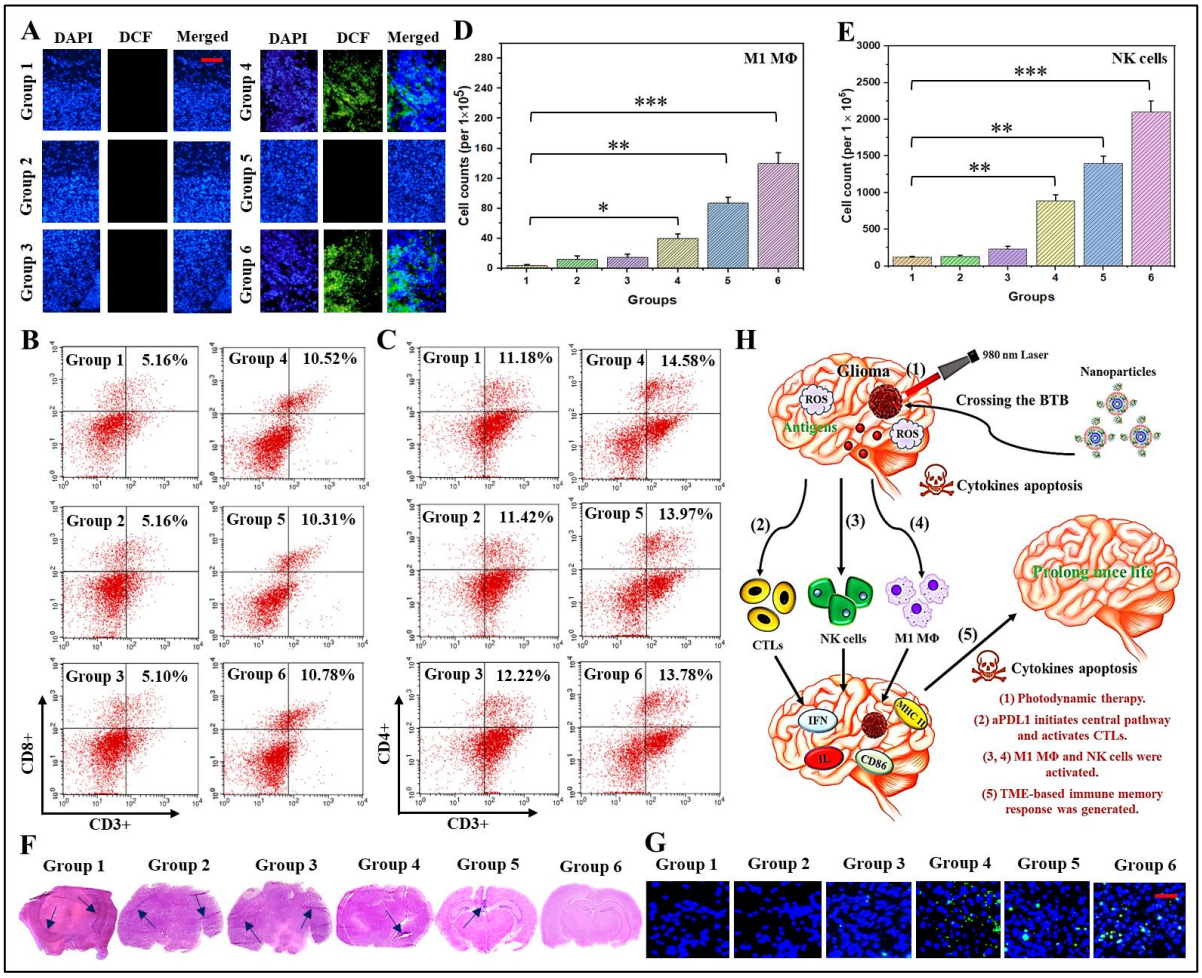

Figure 6. (A) CLSM images of PDT-induced $^1O_2$ generation *in vivo*. The proportion of tumor-infiltrating CD8+ cytotoxic T cells (B) and CD4+ effector T cells (C) in each treatment group. The number of M1 MΦ (D) and NK cells (E) in each treatment group. H&E staining (F), TUNEL staining (G) of tumor sections after different treatments (scale bars: 200 μm). (H) The mechanisms of the photo-immunotherapy process of BK@γ-PGA@5-ALA@MUCNP@aPDL1 NPs for GBM. **P* < 0.05, ***P* < 0.01, and ****P* < 0.001.

By recording the survival curves of orthotopic GBM mice under various treatments, we found that mice in group 6 survived for over 60 days (**Figure S16**); this is in significant contrast to other groups (which died within 48 days), suggesting the most potent therapeutic effect induced by long-term immune memory protection via BK@γ-PGA@5-ALA@MUCNP@aPDL1-mediated photo-immunotherapy. H&E (**Figure 6F**), and dUTP-biotin nick end labeling (TUNEL) (**Figure 6G**) staining of tumor slices were performed to detect the apoptotic situation under various treatments. It was found that BK@γ-PGA@5-ALA@MUCNP@aPDL1 in conjunction with 980 nm laser irradiation induced the most significant apoptotic level. Moreover, the indistinctive mouse body weights and normal

histological H&E images in all groups suggest the excellent biocompatibility of the NPs (**Figure S17**).

The visible inhibition of GBM growth and relapse from our NPs could be explained as follows (**Figure 6H**): (1) PDT was identified to induce the CNS and thus activate the immune system. Next, the PDT of BK@γ-PGA@5-ALA@MUCNP@aPDL1 NPs killed GBM cells via both necrosis and apoptosis. Then, the dead tumor cells would be "eaten" and generate tumor-derived antigenic peptides via innate immune effector cells, which could stimulate the corresponding T-cell response; (2) aPDL1 initiates central pathway inhibition with cancer cells attack and activates CTLs; (3, 4) activated tumoricidal M1 MΦ and NK cells are another strength for eliminating tumor cells; (5) these NPs possess vaccine characters that they could induce a long-term immune memory response specifically for GBM based on their effectively photo-immunotherapy effect, which would largely inhibit tumor relapse.

Conclusion

In summary, we provide a multifunctional NP based on MUCNP to specifically trigger the brain antitumor immune response via 980 nm laser-mediated PDT. With this nanoplatform, we temporarily opened the BBB around the GBM, obtaining meaningful progress in introtumoricidal efficiency by increasing the number of GBM-targeted NPs. Moreover, the excellent NIR laser-induced PDT effect from BK@γ-PGA@5-ALA@MUCNP@aPDL1 NPs leads to serious GBM cell damage, which leads to a stronger immune response by releasing endogenous tumor antigens. Later, the released-aPDL1 from NPs enhanced immune cytokine secretion and recruited CD4+ and CD8+ T cells into GBM, thus enhancing the therapeutic efficacy. In addition, tumoricidal MΦ and NK cells are activated during this process, exacerbating GBM elimination and inducing long-term immune memory. Therefore, we aim to provide a nanoplatform based on PpIX, possessing great photo-immunotherapy potency, eliminating primary GBM, and preventing GBM relapse. This would be a tremendous advance in the clinical treatment of GBM.

Supporting Information

Supporting Information is available from the Wiley Online Library or from the author.

Acknowledgements

This work is supported by the Villum Fonden, Denmark, Project No. 13153.

Conflict of Interest

The authors declare no conflict of interest.

Keywords: glioblastoma; immunotherapy; photodynamic therapy; reactive oxygen species; cytotoxic T lymphocyte

[1] a) H. Ohgaki, P. Kleihues, *Clin. Cancer. Res.* **2013**, *19*, 764-772; b) C. L. Tso, W. A. Freije, A. Day, Z. Chen, B. Merriman, A. Perlina, S. F. Nelson, *Cancer Res.* **2006**, *66*, 159; c) P. I. D'Urso, O. F. D'Urso, C. Storelli, M. Mallardo, C. D. Gianfreda, A. Montinaro, S. Marsigliante, *Int. J. Oncol.* **2012**, *41*, 228; d) H. Hu, Q. Mu, Z.Bao, Y.Chen, Y.Liu, J. Chen, T. Jiang, *Cell* **2018**, *175*, 1665.
[2] H. Guerrero-Cázares, S. Y. Tzeng, N. P. Young, A. O. Abutaleb, A. Quiñones-Hinojosa, J. J. Green, *ACS Nano* **2014**, *8*, 5141.
[3] J. Chen, Y. Li, T.-S. Yu, R. M. McKay, D. K. Burns, S. G. Kernie, L. F. Parada, *Nature* **2012**, *488*, 522.
[4] a) N. Kuthala, R. Vankayala, Y. N. Li, C. S. Chiang, K. C. Hwang, *Adv. Mater.* **2017**, *29*, 1700850; b) R. F. Barth, Z. Zhang, T. Liu, *Cancer Commun.* **2018**, *38*, 1; c) M. Ratnaparkhe, J. K. Wong, P. C. Wei, M. Hlevnjak, T. Kolb, M. Simovic, A. Ernst, *Nat. Commun.* **2018**, *9*, 1.
[5] H. Jin, G. Zhao, J. Hu, Q. Ren, K. Yang, C. Wan, A. Huang, P. Li, J.-P. Feng, J. Chen, *ACS Appl. Mater. Interfaces* **2017**, *9*, 25755.
[6] C. Song, H. Phuengkham, Y. S. Kim, I. Lee, I. W. Shin, H. S. Shin, S. M. Jin, S. H. Um, H. Lee, K. S. Hong, *Nat. Commun.* **2019**, *10*, 1.
[7] C. K. Chung, C. Da Silva, D. Kralisch, A. Chan, F. Ossendorp, L. J. Cruz, *J. Control. Release* **2018**, *285*, 56.
[8] a) K. M. Hargadon, C. E. Johnson, C. J. Williams, *Int. Immunopharmacol.* **2018**, *62*, 29-39; b) Q. Fan, Z. Chen, C. Wang, Z. Liu, *Adv. Funct. Mater.* **2018**, *28*, 1802540.
[9] A. Deczkowska, I. Amit, M. Schwartz, *Nat. Neurosci.* **2018**, *21*, 779.
[10] a) S. D. Kamath, P. U. Kumthekar, *Front. Oncol.* **2018**, *8*, 414; b) L. Marcelis, A. Antoranz, A. M. Delsupehe, P. Biesemans, J. F. Ferreiro, K. Debackere, T. Tousseyn, *Cancer Immunol. Immunother.* **2020**, *69*, 1751.
[11] A. M. Lesokhin, T. M. Hohl, S. Kitano, C. Cortez, D. Hirschhorn-Cymerman, F. Avogadri, G. A. Rizzuto, J. J. Lazarus, E. G. Pamer, A. N. Houghton, *Cancer Res.* **2012**, *72*, 876.
[12] T. Chanmee, P. Ontong, K. Konno, N. Itano, *Cancers (Basel)* **2014**, *6*, 1670.
[13] X. Yang, Y. Lin, Y. Shi, B. Li, W. Liu, W. Yin, Y. Dang, Y. Chu, J. Fan, R. He, *Cancer Res.* **2016**, *76*, 4124.
[14] X. Gao, Q. Yue, Z. Liu, M. Ke, X. Zhou, S. Li, J. Zhang, R. Zhang, L. Chen, Y. Mao, *Adv. Mater.* **2017**, *29*, 1603917.
[15] K. Fan, X. Jia, M. Zhou, K. Wang, J. O. Conde, J. He, J. Tian, X. Yan, *ACS Nano* **2018**, *12*, 4105.
[16] X. Li, Y. Yang, H. Zhao, T. Zhu, Z. Yang, H. Xu, Y. Fu, F. Lin, X. Pan, L. Li, *J. Am. Chem. Soc.* **2020**, *142*, 3862.
[17] a) T. T. Zhang, W. Li, G. Meng, P. Wang, W. Liao, *Biomater. Sci.* **2016**, *4*, 219; b) R. Qiao, Q. Jia, S. Huwel, R. Xia, T. Liu, F. Gao, M. Gao, *ACS Nano*. **2012**, *6*, 3304; c) S. Wohlfart, A. S. Khalansky, S. Gelperina, D. Begley, J. Kreuter, *J. Control. Release*, **2011**,*154*, 103.
[18] Y. Song, D. Du, L. Li, J. Xu, P. Dutta, Y. Lin, *ACS Appl. Mater. Interfaces* **2017**, *9*, 20410.
[19] T. Lin, P. Zhao, Y. Jiang, Y. Tang, H. Jin, Z. Pan, H. He, V. C. Yang, Y. Huang, *ACS Nano* **2016**, *10*, 9999.
[20] a) K. B. Johnsen, T. Moos, *J. Control. Release* **2016**, *222*, 32; b) K. B. Johnsen, M. Bak, F. Melander, M. S.Thomsen, A. Burkhart, P. J. Kempen, T. Moos, *J. Control. Release* **2019**, *295*, 237; c) G. Sharma, A. R. Sharma, S. S. Lee, M. Bhattacharya, J. S. Nam, C. Chakraborty, *Int. J. Pharm.* **2019**, *559*, 360.
[21] Y. Xu, G. K.-W. Kong, J. G. Menting, M. B. Margetts, C. A. Delaine, L. M. Jenkin, V. V. Kiselyov, P. De Meyts, B. E. Forbes, M. C. Lawrence, *Nat. Commun.* **2018**, *9*, 1.
[22] J. S. Smith, S. Rajagopal, *J. Biol. Chem.* **2016**, *291*, 8969.
[23] J. Zhang, X. Zhang, G. Liu, D. Chang, X. Liang, X. Zhu, W. Tao, L. Mei, *Theranostics* **2016**, *6*, 2099.
[24] K. B. Johnsen, M. Bak, F. Melander, M. S. Thomsen, A. Burkhart, P. J. Kempen, T. L. Andresen, T.Moos, *J. Control. Release* **2019**, *295*, 237.
[25] J. Lai, G. Deng, Z. Sun, X. Peng, J. Li, P. Gong, P. Zhang, L. Cai, *Biomaterials* **2019**, *211*, 48.

[26] a) W. Wang, Z. Hu, *Adv. Mater.* **2019**, *31*, 1804827; b) A. Battigelli, J. Russier, E. Venturelli, C. Fabbro, V. Petronilli, P. Bernardi, A. Bianco, *Nanoscale* **2013**, *5*, 9110; c) K. Glunde, D. Artemov, M. F. Penet, M. A. Jacobs, Z. M. Bhujwalla, *Chem. Rev.* **2010**, *110*, 3043.
[27] M. N. Oliveira, B. Breznik, M. M. Pillat, R. L. Pereira, H. Ulrich, T. T. Lah, *Cancer Microenviron.* **2019**, *12*, 1.
[28] I. Sörensen-Zender, R. Chen, S. Rong, S. David, A. Melk, H. Haller, R. Schmitt, *Transl. Res.* **2019**, *213*, 124.
[29] X. Hu, R. K. Leak, A. W. Thomson, F. Yu, Y. Xia , L. R.Wechsler, J. Chen, *Nat. Rev. Neurol.* **2018**, *14*, 559.
[30] J. Côté, V. Bovenzi, M. Savard, C. Dubuc, A. Fortier, W. Neugebauer, L. Tremblay, W. Müller-Esterl, A.-M. Tsanaclis, M. Lepage, *PLoS One* **2012**, *7*, 37485.
[31] M. Simonelli, L. Di Tommaso, M. Baretti, A. Santoro, *Immunotherapy* **2016**, *8*, 1363.
[32] a) K. L. Black, K. Chen, D. P. Becker, J. E. Merrill, *J. Neurosurg.* **1992**, *77*, 120-126; b) A. Murat, E. Migliavacca, S. F. Hussain, A. B. Heimberger, I. Desbaillets, M. F. Hamou, M. E. Hegi, *PloS One* **2009**, *4*, 5947.
[33] M. K. Kranjc, M. Novak, R. G. Pestell, T. T. Lah, *Radiol. Oncol.* **2019**, *53*, 397-406.
[34] M. F. Attia, N. Anton, J. Wallyn, Z. Omran, T. F. Vandamme, *J. Pharm. Pharmacol.* **2019**, *71*, 1185.
[35] L. Hu, Z. Cao, L. Ma, Z. Liu, G. Liao, J. Wang, S. Shen, D. Li, X. Yang, *Biomaterials* **2019**, *223*, 119469.
[36] U. Salem, V. A. Kumar, J. E. Madewell, D. F. Schomer, D. C. de A. Bastos, P. O. Zinn, J. S. Weinberg, G. Rao, S. S. Prabhu, R. R. Colen, *Cancer Imaging*, **2019**, *19*, 1.
[37] J. Xu, L. Xu, C. Wang, R. Yang, Q. Zhuang, X. Han, Z. Dong, W. Zhu, R. Peng, Z. Liu, *ACS Nano* **2017**, *11*, 4463.
[38] B. Lin, J. Liu, Y. Wang, F. Yang, L. Huang, R. Lv, *Chem. Mater.* **2020**, *32*, 4627.
[39] S. Cao, J. Fan, W. Sun, F. Li, K. Li, X. Tai, X. Peng, *Chem. Commun.* **2019**, *55*, 12956.
[40] Y. Zhang, L. He, J. Wu, K. Wang, J. Wang, W. Dai, A. Yuan, J. Wu, Y. Hu, *Biomaterials* **2016**, *107*, 23.
[41] a) R. Baskaran, J. Lee, S. -G. Yang, *Biomater. Res.* **2018**, *22*, 1-8; b) V. Snyder, T. C. Reed-Newman, L. Arnold, S. M. Thomas, S. Anant, *Front. Oncol.* **2018**, *8*, 203.
[42] L. Yan, J. Miller, M. Yuan, J. F. Liu, T. M. Busch, A. Tsourkas, Z. Cheng, *Biomacromolecules* **2017**, *18*, 1836.
[43] A. Potapov, S. Goryaynov, V. Okhlopkov, L. Shishkina, V. Loschenov, T. Savelieva, D. Golbin, A. Chumakova, M. Goldberg, M. Varyukhina, *Neurosurg. Rev.* **2016**, *39*, 437.
[44] Z. Luo, L. Zhang, R. Zeng, L. Su, D. Tang, *Anal. Chem.* **2018**, *90*, 9568.

Supporting Information for PAPER I

Experimental Section

Chemicals. γ-PGA (Mw = 1000 kDa), des-Arg^9-Kallidin (BK), iron(III) chloride hexahydrate, iron(II) dichloride tetrahydrate, Yttrium(III) nitrate hexahydrate, Ytterbium (III) nitrate pentahydrate, Erbium(III) nitrate pentahydrate, Neodymium(III) nitrate hexahydrate, dioctyl sodium sulfosuccinate (AOT), sodium hydroxide, sodium fluoride, 1-Ethyl-3-(3-dimethylaminopropyl) carbodiimide (EDC), hydroxy-2,5-dioxopyrrolidine-3-sulfonicacid sodium salt (NHS), 4′,6-diamidino-2-phenylindole (DAPI), and 1,3-diphenylisobenzofuran (DPBF) were supplied from Sigma-Aldrich (St. Louis, USA). Ammonium hydroxide, oleic acid (OA), toluene, and N-methyl pyrrolidone (NMP) were obtained from Sinopharm Chemical Reagent Co., Ltd. (Shanghai, China). 3-(4,5-dimethyl-2-thiazolyl)-2,5-diphenyl-2-H-tetrazolium bromide (MTT), Phosphate-buffered solution (PBS), live/dead cell double staining kit, Dulbecco's modified eagle medium (DMEM), dimethyl sulfoxide (DMSO), and reactive oxygen species (ROS) determination kit was obtained from Keygen Biotech. Co., Ltd. (Nanjing, China).

Synthesis of MUCNP. The OA-Fe_3O_4 nanoparticles were prepared using an ammonia coprecipitation method of Fe (III) and Fe (II). Then, the MUCNPs were prepared using as-prepared OA-Fe_3O_4 NPs as seeds and covered with red UCL shells by the hydrothermal method. Typically, 3.33 mL of $Y(NO_3)_3$ (0.5 M), 3 mL of $Yb(NO_3)_3$ (0.2 M), and 0.33 mL of $Er(NO_3)_3$ (0.2 M) water solution were added into 33.3 mL ethanol contained 0.99 g NaOH, 2.5 mL of toluene dispersion of OA-Fe_3O_4 (10 mg/mL), 2.5 mL of toluene and 16.65 mL of OA under stirring. Then 6.66 mL of NaF (8 mM) was then dropped wisely into the mixture. After 30 min of vigorous agitation at room temperature, the mixed solution was transferred into a 100 mL sealed Teflon-lined autoclave and heated at 200 °C for 8 h. Finally, the mixture was cooled to room temperature, and the product was collected by magnetic separation and washed with ethanol several times. Finally, PAA with strong coordination ability was used to displace hydrophobic ligands on the MUNCP surface by a ligand exchange process for endowing MUNCP with hydrophilicity.

Preparation of BK@γ-PGA@5-ALA@MUCNP@aPDL1 NPs. Firstly, γ-PGA@5-ALA solution was prepared as follows: 20 mg 5-ALA was dissolved in 3 mL PBS, the pH of the solution was adjusted at 7.0 by NaOH. Subsequently, 0.22 μm filter was used to degerm for the

store in a certain period. 10 mg γ-PGA was dissolved in 200 μL PBS, 4.5 mg EDC, and 3 mg NHS was added in sequence and mixed for 2 h at room temperature. Then, an aqueous aPDL1 and MUNCP were mixed with an aqueous γ-PGA@5-ALA with a final volume of 25 mL. Test complexes were obtained upon addition of the mixed solution, using a pipette, into an aqueous CS (10 kDa, with a degree of deacetylation of 85%, 0.2 mg/mL, 20 mL, pH 6.0) and then thoroughly mixed for 30 s by vortex and left for at least 1 h at room temperature. Finally, BK was coated on the γ-PGA@5-ALA@MUCNP@aPDL1 NPs surface by the EDC method.

In-vitro Release of aPDL1. To determine the drug release of aPDL1 from the BK@γ-PGA@5-ALA@MUCNP@aPDL1, we suspended the weighed freeze-dried BK@γ-PGA@5-ALA@MUCNP@aPDL1 in 10 mL of release medium. aPDL1 released from BK@γ-PGA@5-ALA@MUCNP@aPDL1 was collected using ultracentrifugation and examined by an anti-rabbit total IgG ELISA kit. To test the ability of BK@γ-PGA@5-ALA@MUCNP@aPDL1 to retain the activity of complexed proteins, the binding affinity of aPDL1 was determined by ELISA with recombinant PDL1 protein. To clarify the effect of PDT on aPDL1 activity, BK@γ-PGA@5-ALA@MUCNP@aPDL1 was first treated by 0.5 or 1.0 W/cm^2 lasers for 10 min and then examined using ELISA.

Hemolysis Test and the Shape of Erythrocytes. Erythrocytes were acquired by centrifuging 5 mL whole blood with anticoagulation at 3000 rpm for 8 min. Ablution of erythrocytes was used PBS and then resuspended in PBS at a volume ratio of 1:9. Afterward, 1.2 mL of BK@γ-PGA@5-ALA@MUCNP@aPDL1 solutions (in PBS) with different concentrations were mixed with 0.3 mL of the attenuated erythrocytes suspension. Positive and negative controls were acquired by mixing 1.2 mL of deionized water and PBS with 0.3 mL of the attenuated erythrocytes suspension, respectively. All mixtures were maintained at 37 °C for 3.5 h and then centrifuged at 3000 rpm for 8 min. A microplate reader (BioTek Synergy 2) was used to measure the optical density (O.D.) of the samples at 541 nm. The calculating equation of the hemolysis rate was as follow:

$$\text{Hemolysis rate (\%)} = [(O.D._{sample} - O.D._{negative})/(O.D._{positive} - O.D._{negative})] \times 100\%.$$

$O.D._{sample}$, $O.D._{positive}$, and $O.D._{negative}$ represent the absorption values of the sample, positive control, and negative control, respectively. Light microscopy (Nanjing Jiangnan Novel Optics Co., Ltd, BM2100) was used for observing the shape of erythrocytes.

Cell Culture. Human glioblastoma (U87-MG) cells, brain capillary endothelial cells (BCECs), and astrocytes were cultured in DMEM medium containing 10 % FBS and 1 % streptomycin-

penicillin. Human umbilical vascular endothelial cells (HUVECs) were cultured in DMEM medium containing 20 % FBS, 10 ng/ml bFGF, and 1 % streptomycin-penicillin.

PpIX Generation in Vitro. The PpIX generation was evaluated by fluorescence emission spectroscopy. The U87-MG cells were plated in a 96-well plate (1×10^6 cells per well) and incubated for 24 h. Then, the cell culture medium was replaced by a serum-free medium, and the cells were treated with BK@γ-PGA@5-ALA@MUCNP@aPDL1 and free 5-ALA at various concentrations for 24 h. Afterward, the cell culture medium was replaced by DMSO (100 μL per well) to extract the generated PpIX by slightly shaking the plate for 15 min. The fluorescence intensity at 635 nm (405 nm excitation wavelength) and UV absorption of each well was recorded by a microplate reader.

Photocytotoxicity. The U87-MG cells were seeded in a 96-well plate (1×10^6 cells per well) and cultured for 24 h. Then, the cell culture medium was replaced by a serum-free medium, and the cells were treated with different samples at various concentrations. After 24 h incubation with different samples, the plate was irradiated by 980 nm or 635 nm light (0.5 W/cm^2) for 10 min. After incubation for 24 h at 37 °C, the culture solution and sample were removed, and 20 μL 5 mg/mL of MTT solution was added for another 4 h incubation. The obtained formazan crystals were dissolved with 100 μL of DMSO and the solution was then measured at 570 nm on a Bio-Tek microplate reader. Flow Cytometry Analysis of Apoptosis. U87-MG cells were treated with BK@γ-PGA@5-ALA@MUCNP@aPDL1 for 24 h. The cells were irradiated by 980 nm (0,5 W/cm^2) for 10 min. After treatment, both adherent and floating cells were collected, washed with PBS, and resuspended in 200 μL of binding buffer containing the fluorescent dyes Calcein-AM and PI and put in the dark for 10 min according to the kit instructions. Then, cells were immediately analyzed by flow cytometry.

In Vitro Penetration of BK@γ-PGA@5-ALA@MUCNP@aPDL1 on the Normal or Morbid BBB Model Assay. The rat primary BCECs were isolated from SD rats and then cultured in a transwell chamber coated with rat tail collagen. The transendothelial electrical resistance (TEER) was measured to assess the integrity of the normal BBB model by an epithelial volt-Ωm instrument. As the TEER reached over 250 Ω cm^2, 10 μg/mL BK@γ-PGA@5-ALA@MUCNP@aPDL1 was added to the apical chambers. And the solution in the basal chamber was collected at each predetermined time point to detect the fluorescence intensity using a fluorescence spectrophotometer. To establish the *in-vitro* morbid BBB model, U87-MG cells were seeded onto the lower chamber, while HUVECs were in the upper chamber at

a density of 5:1 U87-MG/HUVECs ratio. The culture medium in each upper chamber was changed by BK@γ-PGA@5-ALA@MUCNP@aPDL1 after 4 days. The fluorescence intensity of collected solutions from the basal chamber was measured.

Animal Model. All animal operations were carried out following institutional animal use and care regulations provided by Nanjing Normal University and Keygen Biotech. Co., Ltd.. For orthotopic glioblastoma models, C57BL/6 mice (8 weeks old, female) were used. Anesthetized mice were fixed at a stereotaxic apparatus and then the brain was cleaned with 75 % ethanol. A hole was drilled with a 1 mm bit at 1.6 mm on the right side of the bregma and 4.6 mm behind the coronal suture. Glioblastoma GL261 cells (1×10^6) in 10 μL of PBS were injected 2.6 mm deep into the brain tissue for 10 min.

Western Blotting Assay. Brain tumors and normal brain tissues taken from the contralateral hemisphere were resected from the brain tumors mice and normal mice, respectively. The following primary antibodies and dilutions were used: rabbit anti-B1R antibody (1:100) (#ABR-011, Alomone labs) and mouse monoclonal anti-β-actin antibody (1:5,000) (#MA1-91399, Thermo Fisher Scientific). For cell line samples testing, rabbit anti-B1R antibody (1:500) (ab75148, Abcam) was used. Goat anti-rabbit IgG H&L (HRP) (ab205718, Abcam) and goat anti-mouse IgG H&L (HRP) (ab205719, Abcam) was used as the secondary antibody at a ratio of 1:10,000. B1R expression was quantified using Image J and was normalized against β-actin expression level.

Dot Blot Assay. The genomic DNA was heated at 95 °C for 10 min to denature, then cooled on ice for 5 min. 120 ng of DNA was dropped onto Hybond-N+ membrane (RPN303B, Ge Healthcare). The membranes cross-linked under UV light at 70,000 μJ/cm^2 for 2 min, then blocked with 1% BSA in PBS. The level of DNA oxidative damage was evaluated using mouse monoclonal antibody for 8-oxoG (4354-MC-050, Trevigen), and a goat anti-mouse IgG H&L (HRP) (ab205719, Abcam).

Immunofluorescence Assay. 5×10^5 of RAW 264.7 cells were seeded in 24-well plates, and treated as indicated groups. Cells were incubated with 4% formaldehyde for 15 min to fix, then 0.5% Triton X-100 for 20 min to permeabilize. Cells were blocked with 1.5% Bovine Serum Albumin (BSA) for 1 h. Then cells were incubated with rabbit anti-iNOS antibody [EPR16635] (ab178945, Abcam) (1:100) at 4 °C for overnight. Cells were washed with cold Hank's for three times and incubated with goat anti-rabbit IgG H&L (Alexa Fluor® 594) (ab150080, Abcam) (1:200) for 1 h. Cells were washed with cold Hank's for three times and stained with

DAPI at ratio of 1:500 for 15 min, and then visualized with a confocal laser scanning microscopy (CLSM).

In Vivo Penetration of BK@γ-PGA@5-ALA@MUCNP@aPDL1 on Morbid BBB Model Assay. The penetration of NPs on normal BBB/morbid BBB model assay was investigated using Evans-Blue (EB) extravasation. Evans Blue (2% in PBS, 4 mL/kg) was injected intravenously into the normal and tumor mice at 8 h after the treatment of γ-PGA@5-ALA@MUCNP@aPDL1 and BK@γ-PGA@5-ALA@MUCNP@aPDL1. The model mice were randomly chosen and sacrificed to harvest the brains for frozen sections. Finally, the frozen sections of the brain were observed under the optical microscope.

In Vivo UCL and MR Imaging. BK@γ-PGA@5-ALA@MUCNP@aPDL1 were intravenously injected into tumor-bearing mice. Fluorescent scans were performed at 24 h post-injection by a CALIPER Lumina II *in-vivo* imaging system with an adjustable 980 nm laser as the exciting source for *in vivo* imaging. BK@γ-PGA@5-ALA@MUCNP@aPDL1 dissolved in serum with different concentrations were scanned by a 3.0 T clinical MR imaging scanner. T2 weighted animal MR imaging was performed under the same MR scanner with a special coil designed for small-animal imaging.

In Vivo toxicity test. Three groups of healthy C57BL/6 mice with five mice in each group were treated with BK@γ-PGA@5-ALA@MUCNP@aPDL1 at changing concentrations (0, 1, and 5 mg/kg), respectively. At 1, 10, and 20 days post-injection, mouse blood with a volume of about 0.8 mL was obtained through the ocular vein and tested using both blood biochemistry assay and blood panel test.

Blood Circulation Time and In Vivo Distribution. C57BL/6 mice (8 weeks old) received an intravenous injection of BK@γ-PGA@5-ALA@MUCNP@aPDL1 (50 mg/kg). At the desired time points venous blood was collected. 24 h after injection, the mice were euthanized. Then, the major organs and tumors were harvested and lysed in the mixture of $HClO_4$ and HNO_3 ($HClO_4$: HNO_3 = 1:9, v/v). The Fe ions contents in blood and organs were measured using ICP-AES. The NPs content was calculated from the increase of Fe ions content in blood or organs with the standard curve.

In Vivo Treatment for Orthotopic Tumor Model. The mice bearing orthotopic brain tumors were categorized into six groups in which ten mice were used in each group. The six groups include group 1 PBS; group 2 aPDL1; group 3 BK@γ-PGA@5-ALA@MUCNP; group 4

BK@γ-PGA@5-ALA@MUCNP plus 980 nm laser; group 5 BK@γ-PGA@5-ALA@MUCNP@aPDL1; and group 6 BK@γ-PGA@5-ALA@MUCNP@aPDL1 plus 980 nm laser. All the major organs (heart, liver, spleen, lung, and kidney) and the tumors were collected and examined by H&E, and TUNEL staining at the end of the antitumor study. At the end of treatment, the number of T-cell, NK cells, M1 MΦ was measured by flow cytometry. Furthermore, blood was drawn from tumor-bearing mice after the treatment, and serum was separated for cytokine analysis. The multiplex cytokine assay was performed using a custom Bio-Plex Pro Assay kit.

In Vivo ROS Measurement. 10 μL of DCFH-DA solution with a concentration of 10 mM was injected into the brain before laser irradiation. Afterward, the brain was illuminated for 10 min (0.5 W/cm^2). Then, the tumor tissues were taken and stained by DAPI. Fluorescence images were collected on an Olympus imaging system.

Statistical Analysis. Mean values and error bars are defined as mean and S.D. The statistical significance was performed by one-way analysis of variance (ANOVA) with Tukey's post hoc test and two-sided unpaired Student's t-test. Statistical significance was set as $*P < 0.05$, $**P < 0.01$, $***P < 0.001$.

Supporting Figures

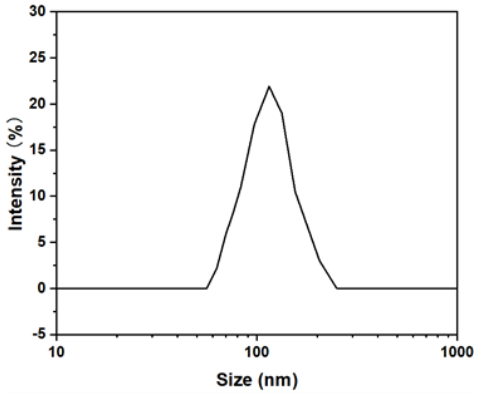

Figure S1. DLS of BK@γ-PGA@5-ALA@MUCNP@aPDL1.

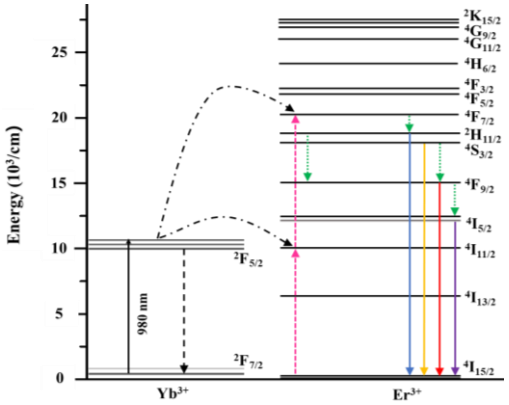

Figure S2. Upconversion mechanism of MUCNP excited using a 980 nm laser.

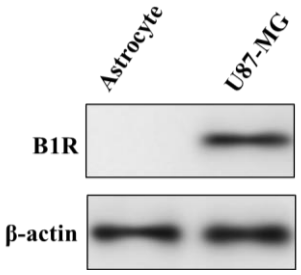

Figure S3. Detection of the protein level of B1R in U87-MG cells and astrocytes by WB.

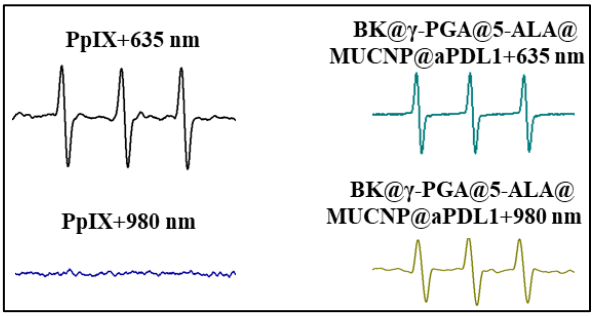

Figure S4. ESR spectra of the different samples extracted from U87-MG cells.

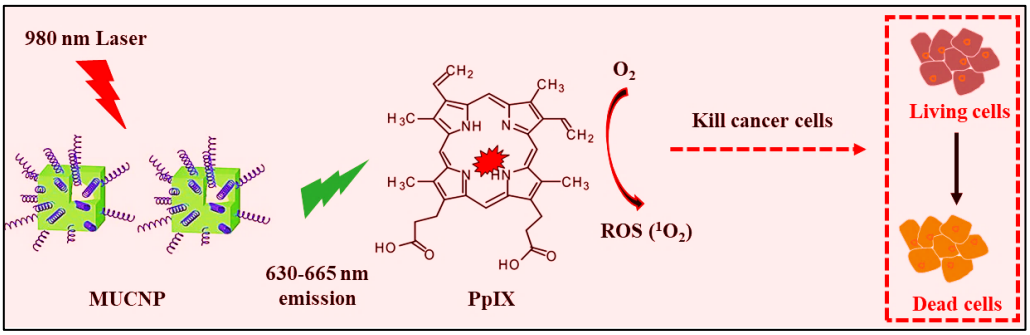

Figure S5. Schematic illustration of PpIX for 980 nm laser trigger PDT.

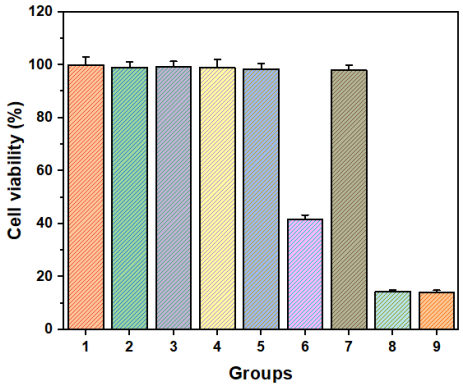

Figure S6. Cell viability assay of U87-MG cells after various treatments. Group 1, PBS; Group 2, only 635 nm laser; Group 3, only 980 nm laser; Group 4, 5-ALA; Group 5, 5-ALA plus 980 nm laser; Group 6, 5-ALA plus 635 nm laser; Group 7, BK@γ-PGA@5-ALA@MUCNP@aPDL1, Group 8, BK@γ-PGA@5-ALA@MUCNP@aPDL1 plus 635 nm laser; and Group 9, BK@γ-PGA@5-ALA@MUCNP@aPDL1 plus 980 nm laser.

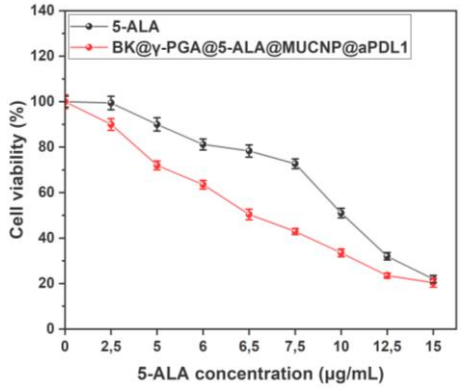

Figure S7. Cell viability assay of U87-MG cells after being treated with BK@γ-PGA@5-ALA@MUCNP@aPDL1 and free 5-ALA under equivalent concentrations of 5-ALA with laser irradiation at 635 nm for 10 min.

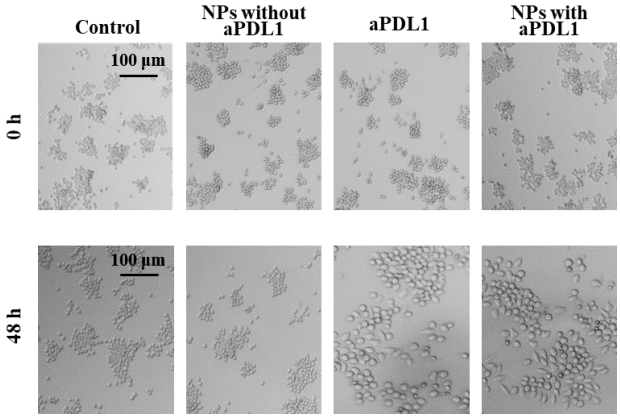

Figure S8. Macrophage proliferation and size increased after BK@γ-PGA@5-ALA@MUCNP@aPDL1 treatment. Scale bar: 30 μm

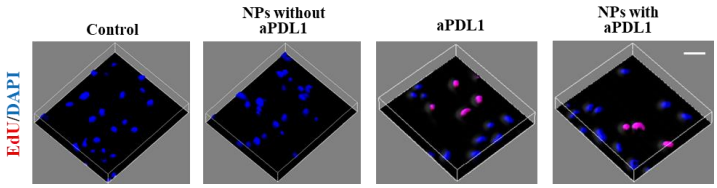

Figure S9. Proliferation was measured using EdU incorporation. Scale bar: 30 μm

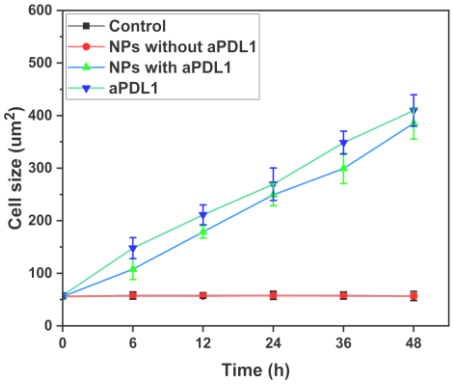

Figure S10. Macrophage size was calculated after BK@γ-PGA@5-ALA@MUCNP@aPDL1 treatment.

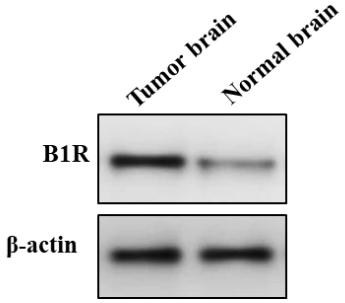

Figure S11. Detection of the protein level of B1R in normal and tumoral brain tissues by WB.

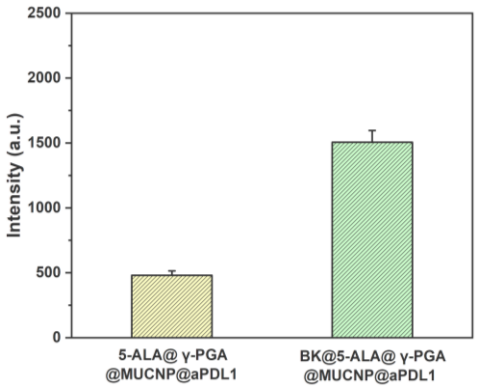

Figure S12. Quantification of UCL signal in the tumor region after tail vein injection of γ-PGA@5-ALA@MUCNP@aPDL1 and BK@γ-PGA@5-ALA@MUCNP@aPDL1 at 24 h.

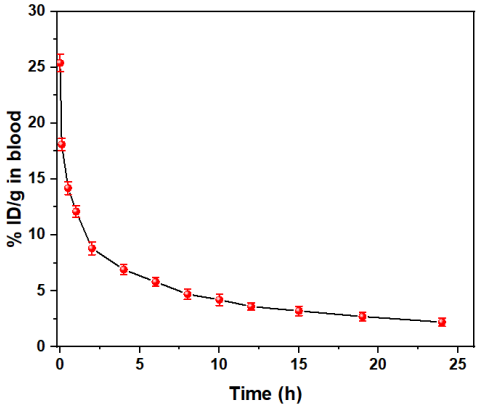

Figure S13. The blood circulation profile of BK@γ-PGA@5-ALA@MUCNP@aPDL1.

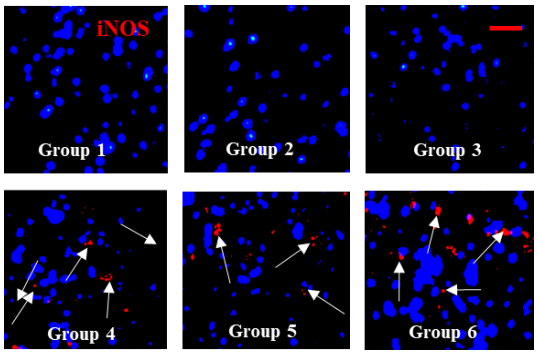

Figure S14. *Ex-vivo* study of M1 MΦ by immunostaining for iNOS after different treatments. Scale bar: 50 μm

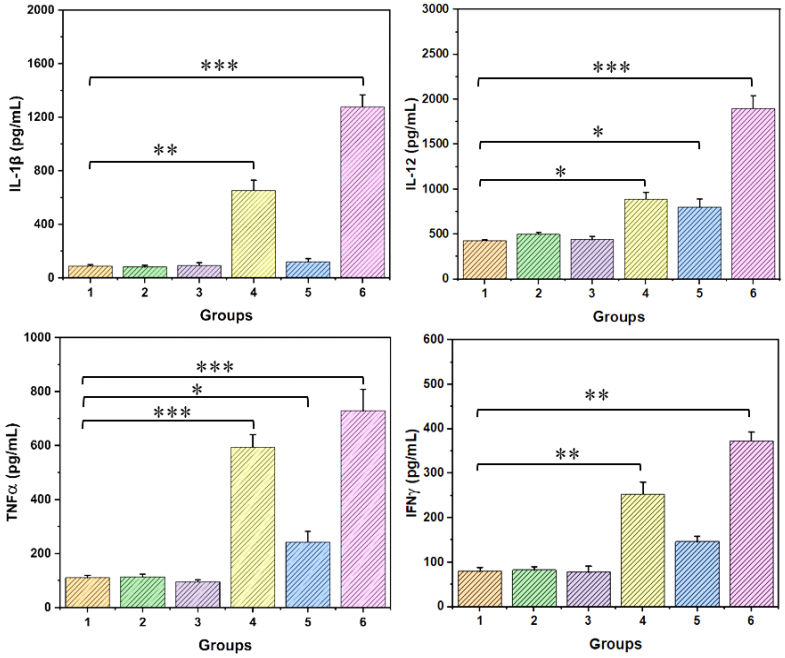

Figure S15. Cytokine expression levels in sera from mice after various treatments. **P* < 0.05, ***P* < 0.01, and ****P* < 0.001.

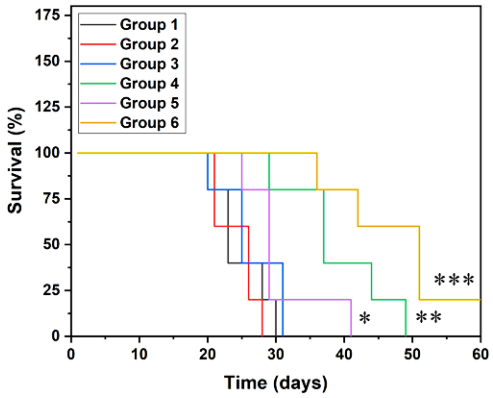

Figure S16. Survival rates of the GL261 tumor-bearing mice after various treatments *P < 0.05, **P < 0.01, and ***P < 0.001.

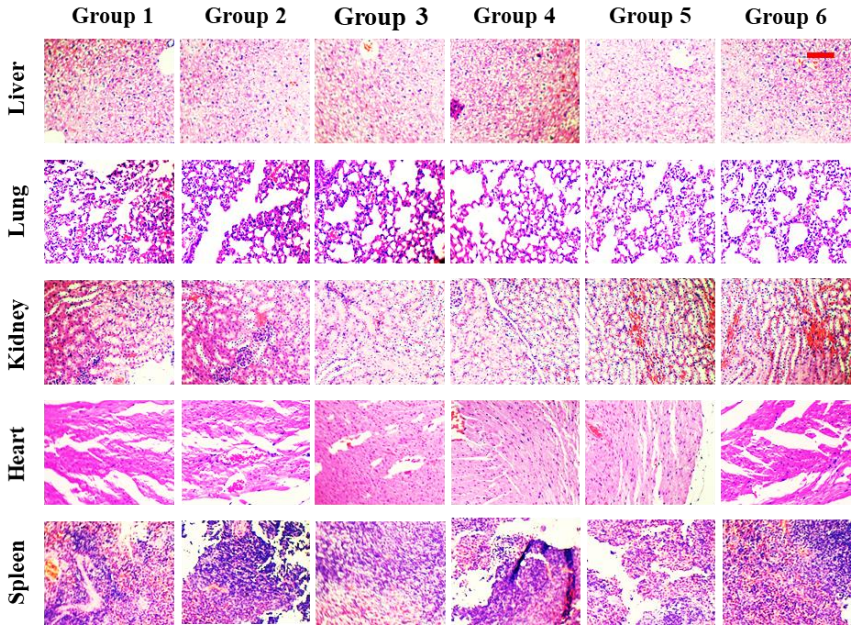

Figure S17. Representative H&E staining of mouse organs after various treatments. Scale bar: 100 μm

PAPER II

Upregulating Aggregation-Induced-Emission Nanoparticles with Blood Brain Barrier Permeability for Precise Photothermal Eradication of Brain Tumors and Induction of Local Immune Responses

Adv. Mater. 2021, 33, 2008802

Upregulating Aggregation-Induced Emission Nanoparticles with Blood Brain Barrier Permeability for Precise Photothermal Eradication of Brain Tumors and Induction of Local Immune Responses

Ming Zhang[a,c], Wentao Wang[a], Mohsen Mohammadniaei[a], Tao Zheng[a], Jon Ashley[a], Qicheng Zhang[c], Shunjie Liu[b*], Yi Sun[a*], Ben Zhong Tang[d*]*

[a]*Department of Health Technology, Technical University of Denmark, Kongens Lyngby, DK-2800, Denmark;*

[b]*Key Laboratory of Polymer Ecomaterials, Changchun Institute of Applied Chemistry, Chinese Academy of Sciences, Changchun 130022, China; University of Science and Technology of China, Hefei 230026, China;*

[c]*Jiangsu Collaborative Innovation Center for Biomedical Functional Materials, School of Chemistry and Materials Science, Nanjing Normal University, Nanjing 210023, P. R. China;*

[d]*Hong Kong Branch of Chinese National Engineering Research Center for Tissue Restoration and Reconstruction, Department of Chemistry, The Hong Kong University of Science and Technology, Clear Water Bay, Kowloon, Hong Kong, 999077 China*

Corresponding authors: Wentao Wang, wentwa@dtu.dk; Shunjie Liu, yhliushunjie@163.com; Yi Sun, suyi@dtu.dk; Ben Zhong Tang, tangbenz@ust.hk

Abstract: *Compared to the other tumors, glioblastoma (GBM) is extremely difficult to treat. Recently, photothermal therapy (PTT) has demonstrated advanced therapeutic efficacies. However, due to the relatively low tissue penetration efficiency of the laser light, its applications in deep-seated tumors are still challenging. In this study, aggregation-induced emission nanoparticles (BK@AIE NPs) were synthesized, featuring selective penetration to the morbid blood brain barrier (BBB) and strong absorbance in the near-infrared region (NIR). The des-Arg9-Kallidin (BK) ligand can prompt morbid BBB adenosine receptor activation, which enhances transportation and accumulation inside the tumor, as confirmed by T1-weighted magnetic resonance (MR) and fluorescence imaging. The BK@AIE NPs exhibit high photothermal conversion efficiency upon irradiation at 980 nm with NIR laser, enabling treatment of deep-seated tumors. The tumor progression could be effectively inhibited to extend the survival spans of mice after the spatiotemporal PTT. The NIR irradiation can eradicate the tumor tissues and release tumor-associated antigens. It was observed that PTT treatment of micebearing GBM activates natural killer (NK) cells, CD3+ T cells, and M1 macrophages in the GBMs area to elevate the therapeutic efficacy. This study demonstrates that NIR-assisted*

BK@AIE NP is a promising strategy for the improved systematic elimination of GBMs and activation of local brain immune privilege.

Introduction

Due to the existence of the morbid blood brain barrier (BBB) and the lack of efficient treatment strategies, glioblastoma (GBM) is currently one of the most devastating cancers.[1-3] The challenges of GBM treatment include (i) the high infiltration and aggressive nature of GBM, which results in the unsatisfactory remission by using traditional treatment methodologies (surgery, adjuvant chemo, or radiotherapy); (ii) the barrier of morbid BBB, which makes it difficult for the delivery of diagnostic and therapeutic agents.[4, 5] Numerous efforts have been devoted to facilitate drugs to cross the morbid BBB. Receptor-mediated transcytosis that utilizes the receptors/transporters expressed on morbid BBB, is a popular approach.[6, 7] However, many of these receptors are ubiquitously expressed in several cell types and tissues, leading to unwanted peripheral organ uptake. Moreover, the transport capacity of endocytosis is rather low due to the limited number of membrane transport proteins and the complex intracellular trafficking procedures. Most methods are invasive and cause a non-specific increase in permeability throughout the central nervous system (CNS).[8] An alternative strategy is to modulate the permeability of morbid BBB, which potentially allows the delivery of larger amount of therapeutics. In that regard, we found that kinin B1 receptor (B1R) is of particular interest. Kinin peptides are natural modulators of the tone and permeability of vessels.[9] The biological tasks of kinins are mediated through the activation of G-protein coupled receptors (GPCR) called the B1R and B2R. B2R exhibits constitutive expression in numerous tissues. On the contrary, except for CNS, B1R is almost undetectable under physiological conditions.[10] Moreover, B1R is proven to be inducible and expressed in major inflammatory diseases, including cardiovascular disease and cancer. Therefore, B1R is likely to serve as a pharmaceutical target to minimize collateral effects.[11] Some researchers have developed B1R-targeted smart drug delivery NPs for cancer and other B1R related cancer diseases treatments.[12, 13] It is noteworthy that GBM is in a zone of inflammation that maintains tumor proliferation and angiogenesis, while the process partly relies on GBM-derived cytokines, which may trigger B1R activity on the microcirculatory system of brain tumors. As a result, GBM cells as well as the surrounding brain capillary endothelial cells show a over expression of B1R.[14] Therefore, we envisioned that the kinin ligand could bind to the B1R on the blood vessel in GBM areas, thus locally increasing the permeability of the morbid BBB. In addition, the kinin ligand can also specifically target the GBM cells. Conjugating the B1R kinin

ligand with therapeutics or nanoparticles (NPs)-based drug delivery systems therefore would present a completely new way to safely and effectively deliver drugs to tumors in CNS.[15, 16]

Nanoparticles-based photothermal therapy (PTT) has been demonstrated with a high degree of efficiency to selectively ablate the tumors.[17] Recently, several strategies of PTT have been proposed for brain tumors. PTT is currently the most widely utilized thermal ablation approach in clinical practice mainly for the treatment of recurrent or deep-seated tumors in the brain.[18, 19] Whereas in these studies, the general power density of 808 nm laser was above 1.5 W/cm^2, which was far beyond the safe 0.33 W/cm^2 value.[20] This is because the dense skull and scalp can cause severe attenuation of the incident light, such that only lasers with high power density can reach the therapeutic threshold to penetrate these tumor tissues. One option to improve the light penetration in PTT, is to change the wavelength of a laser from 808 nm to 980 nm, as the living tissues would be more transparent for the 980 nm laser.[21-23] However, an unresolved issue to apply 980 nm laser in brain-tumor PTT treatment is the lack of secondary NIR (NIR-II) photothermal therapeutic agents.[24, 25]

Fortunately, aggregation-induced emission (AIE)-active luminogens (AIEgens), as a new kind of fluorophore with freely abundant motioned molecular rotators or vibrators in structure, would be an ideal option as a NIR-II photothermal therapeutic agent. The AIEgens has a potential tunable performance by promoting or inhibiting the intramolecular motions, and NIR-II absorbing AIEgens have been demonstrated.[26-30] Furthermore, organic theranostic agents can be fabricated into NPs forms to obtain ideal blood circulation time and preferential accumulation in the tumor regions.[31, 32] Although synthesis of AIEgen NPs may partially restrict the intramolecular motion of AIEgens, AIE NPs can form in loose packing configurations to keep intramolecular motions active based on their inherent twisted propeller-like conformations.[33-35] This, in turn, makes AIEgens suitable for balancing energy dissipation and multifunctional phototheranostics.[36-38] Thus we hypothesized that AIE NPs could function as effective NIR-II PTT agents. In addition, according to recent preliminary clinical trial studies, PTT can generate a tumoricidal immunological effect by releasing tumor-associated agents from the residue after hyperthermia of tumor cells.[39-41] Inspired by such interesting findings, we also postulated that the tumor-associated antigens generated *in situ* after NIR-II PTT treatment would activate the immune response in the GBM region.

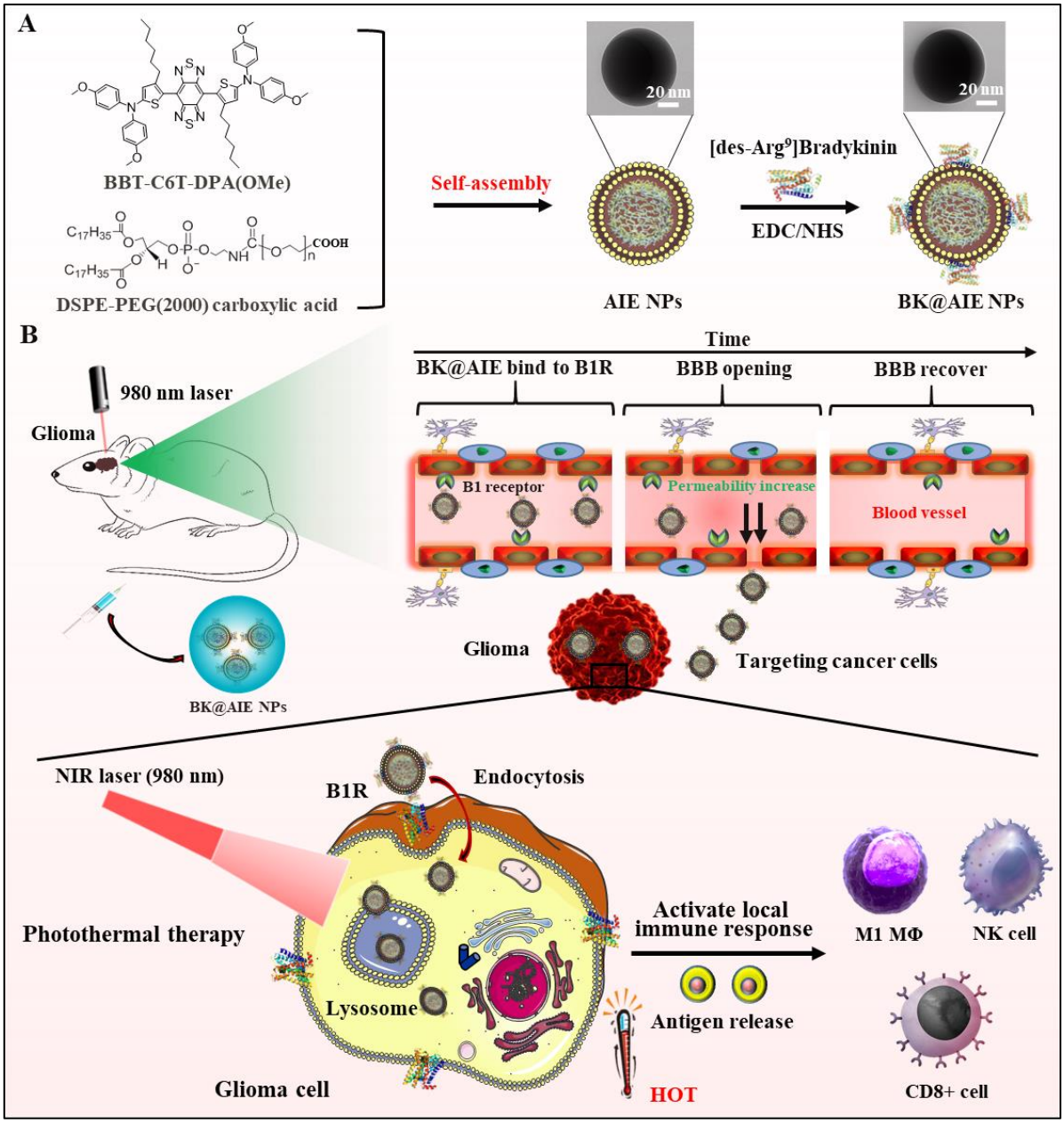

Figure 1. Schematic diagram of (A) fabrication procedure of BK@AIE NPs, and (B) synergetic treatment of brain tumors using PTT and local immune response activation.

Herein, the des-arg^9-Bradykinin (BK, a type of B1R agonist) decorated biocompatible and photostable conjugated AIE NPs with strong absorption in the NIR-II window were designed for brain tumor treatment using a synergetic strategy of PTT and local immune response activation (**Figure 1A**). A higher penetration efficiency into the scalp and skull for 980 nm laser was observed as compared with the common 808 nm laser, which is in agreement with previous literatures.[42, 43] In addition, owing to the active targeting effect of the BK ligand, a real-time multi-modal imaging system assisted clear pinpointing of the aggregation of BK@AIE NPs in the GBM. After spatiotemporal PTT, the tumor progression was effectively

inhibited and the immune response was significantly activated. Finally, BK@AIE NPs-mediated PTT further stimulated the activation of T lymphocytes, natural killer (NK) cells, and enhanced M0 macrophages differentiating into M1 macrophages (MΦ) (**Figure 1B**). To the best of our knowledge, this is the first report of using AIE NPs with covalently bonded B1R agonists to treat brain tumors and activate the local immune response.

Results and discussion

The synthetic routes of BBT-C6T-DPA(OMe) are given in **Figure 2A**. Its structures and characterization results are shown in **Figure S1-3**. In BBT-C6T-DPA(OMe) small molecules, the intramolecular bond stretching vibration is less sensitive to the external environmental constraints compared with the intramolecular rotation, making it extremely advantageous in improving the heat generation inside the NPs. To investigate more about the photothermal characteristics at the morphological level, we synthesized the AIE NPs through a nanoprecipitation method using amphiphilic copolymers (DSPE-PEG(2000)carboxylic acid), a type of biocompatible copolymers that have been used frequently in the drug delivery field, as the doping matrix (**Figure 2B**). In addition, the matrix endued AIEgens with desirable blood circulation time and excellent colloidal stability. To increase the permeability of the morbid BBB and target to the GBM cells, BK was modified on the AIE NPs surface *via* EDC/NHS coupling. The BK modified surface would enhance the cell uptake for NPs then resulting in ameliorating therapy outcomes.

We assessed three characteristics of BK@AIE NPs to evaluate their feasibility for PTT: (i) absorption properties in the NIR region, (ii) photostability, and (iii) photothermal conversion (PC) efficiency. From the UV-Vis spectra of BK@AIE NPs in **Figure 2C**, two distinct peaks can be seen in the UV and NIR regions. Interestingly, a broad absorption was observed within the NIR region with the maximum value near 980 nm, making it very applicable for NIR-II PTT. Evidently, the change in NP concentration from 30 to 120 μg/mL increased the measured absorption intensity. In this work, we selected a commercially-available and compatible 980 nm continuous laser to study the NIR-II photothermal effect of BK@AIE NPs with different concentrations under different laser powers. In **Figure 2D-F**, the temperature of BK@AIE NPs solutions increased dramatically with 980 nm laser irradiation and with an increase in BK@AIE NP concentration. The temperature of BK@AIE NPs solutions (120 μg/mL) increased by 31.3 ℃ with 5 min irradiation, while the temperature in the water group increased by 3.2 ℃ (**Figure 2D**). **Figure 2E, F** illustrate the recorded temperature of BK@AIE NPs

suspension as a function of laser power. A rapid increase in BK@AIE NPs temperature within 5 min was observed, from which, 0.72 W/cm^2 laser power represented an appropriate localized temperature of 56.4 ± 2.1 ^{o}C for further analysis. Moreover, the photothermal stability of BK@AIE NPs was evaluated. As shown in **Figure 2G**, the PC properties of BK@AIE NPs showed no significant change after five cycles of NIR irradiation, whereas for the free indocyanine green (ICG) a gradual decrease of temperature over the five cycles was seen, suggesting good photothermal stability of our developed BK@AIE NPs.

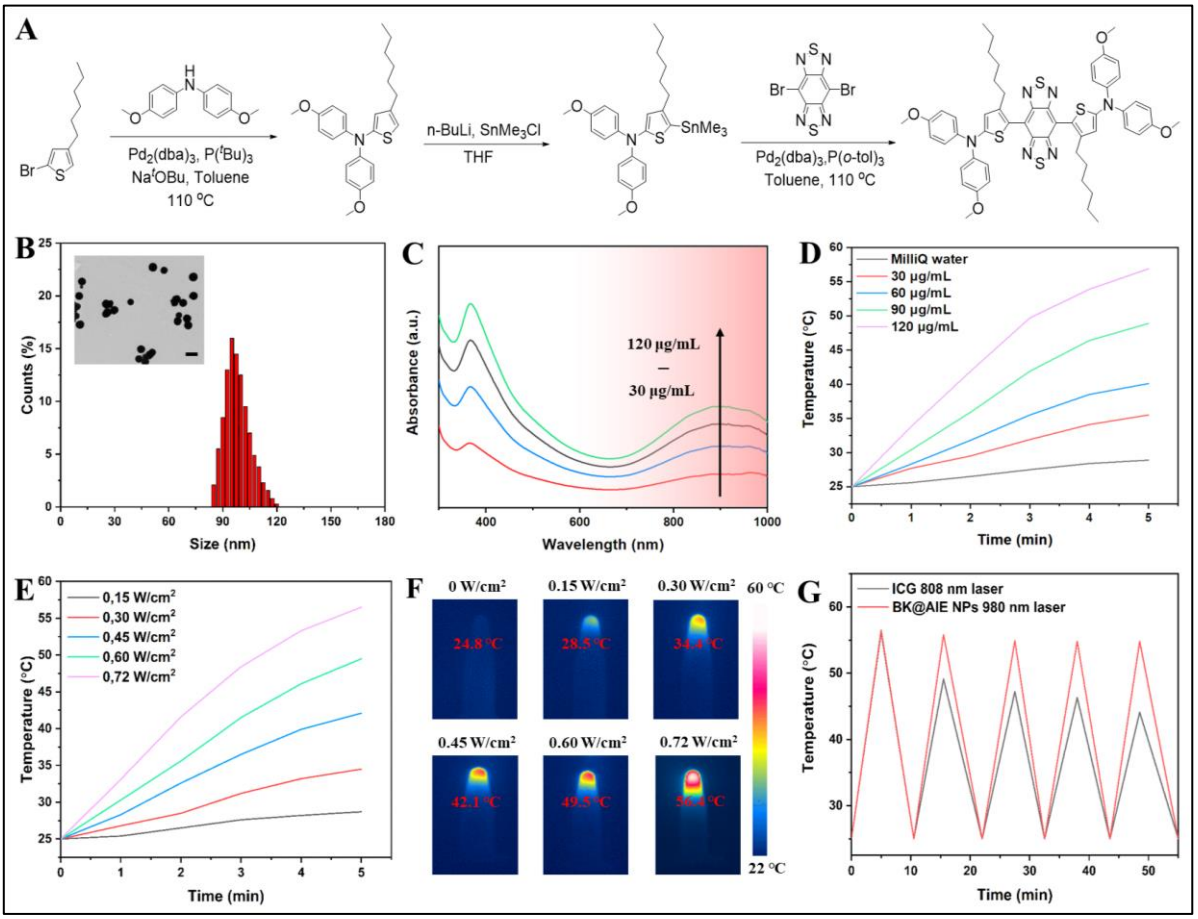

Figure 2. (A) Synthetic procedure of BBT-C6T-DPA(OMe). (B) DLS data of BK@AIE NPs. Inset shows the TEM image of BK@AIE NPs. Scale bar: 100 nm (C) UV-Vis spectra of BK@AIE NPs at different concentrations. (D) Photothermal effects of BK@AIE NPs at different concentrations under 980 nm laser (0.72 W/cm^2). (E) Photothermal effects of BK@AIE NPs (120 μg/mL) at different laser powers. (F) Infrared thermal images of BK@AIE NPs at different laser powers for 5 min. (G) The temperature change of free ICG and BK@AIE NPs over five cycles of repeated laser irradiation (switch on/off).

To verify the superiority of the 980 nm laser over the 808 nm laser for PTT, their penetration ability was evaluated via irradiating various tissues. As shown in **Figure S4**, **5**, the 980 nm laser represented significantly deeper penetration than that of the 808 nm laser under the same tissue thickness. For instance, within 3 mm chicken tissues, about 41% of the 980 nm

laser energy was successfully kept, while this was only around 28% for the 808 nm laser (**Figure S4**). **Figure S5** indicates the results of the laser penetration rate through the mice skulls and scalps. In the mice skull group, tissues treated with 980 nm laser (85%) retained more light energy than the 808 nm laser (78%) treated group. Similarly, through mice skulls together with the scalps, tissues treated with 980 nm laser (48%) lost less light energy than the 808 nm laser (31%) treated group. Therefore, these results indicate that 980 nm PTT should be more effective in treating brain tumors.

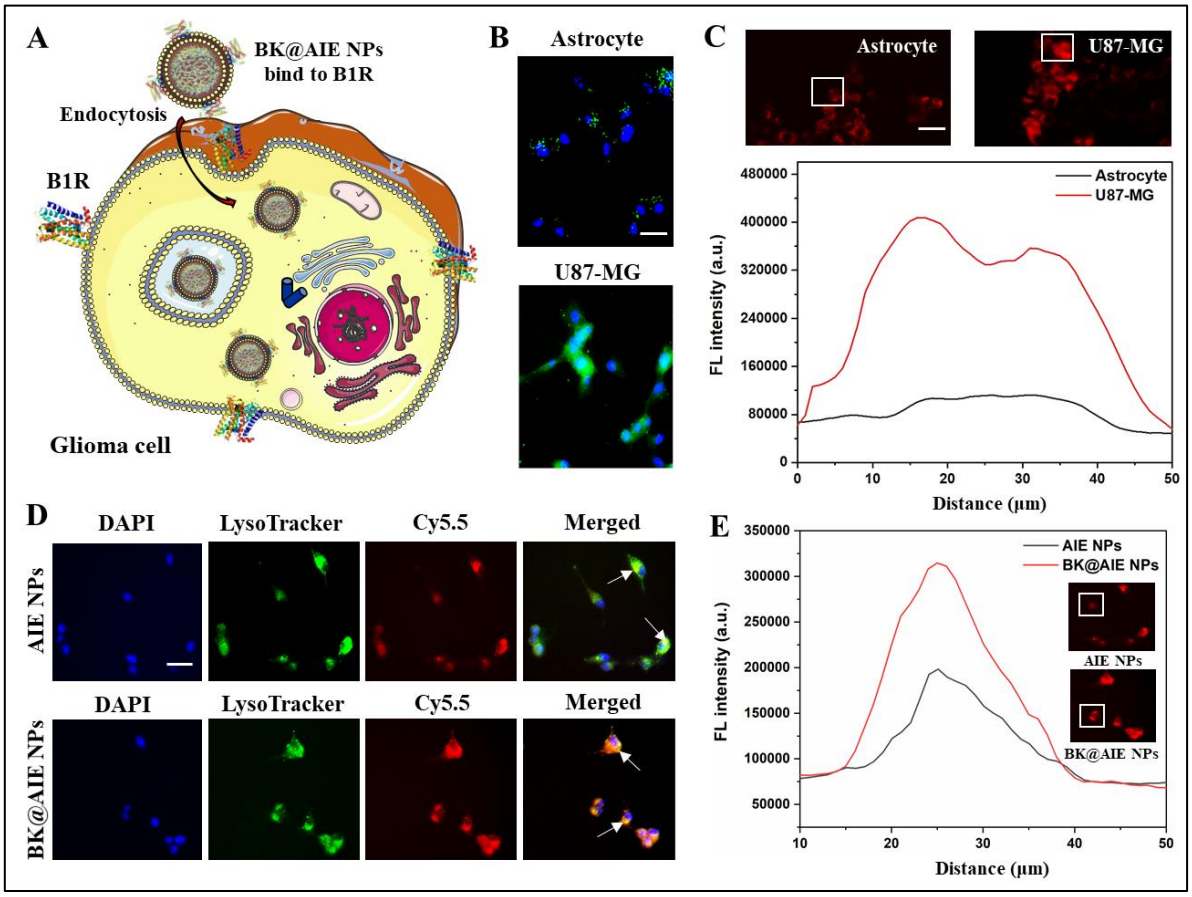

Figure 3. (A) The proposed mechanism of BK@AIE NPs cellular uptake pathway. (B) Detection of B1R in U87-MG cells and astrocytes. Scale bar: 20 μm (C) Confocal laser scanning microscopy (CLSM) images and quantitative fluorescence intensity of the *in vitro* cellular uptake of BK@AIE NPs cells in U87-MG cells and astrocytes. Scale bar: 50 μm (D) CLSM images of U87-MG cells after incubation with AIE NPs and BK@AIE NPs for 4 h. Scale bar: 20 μm (E) The quantitative fluorescence intensity of U87-MG cells after incubation with AIE NPs and BK@AIE NPs by Image J. All NPs were labeled with Cy5.5.

It is well known that active targeting could efficiently improve the targeted ability for nanoscale formulations during the drug delivery process. B1R, inducible prototypical GPCR regulates the permeability of vessels in brain tumors.[44,45] Therefore, B1R was investigated as the specific biomarker on the AIE NPs for inflammatory tumor cells (**Figure 3A**). Here, we

detected the expression of B1R in the U87-MG cells and astrocytes. Based on the immunofluorescence analysis, there is a significantly higher signal from B1R protein in U87-MG cells compared to the astrocytes (**Figure 3B**). To verify the *in vitro* BK@AIE NPs targeting efficiency, Cyanine-5.5 (Cy5.5) was chosen to modify the BK@AIE NPs for monitoring uptake *via* EDC/NHS coupling. The uptake of BK@AIE NPs was observed by a fluorescence microscope followed by quantitative data analysis using Image J software (**Figure 3C**). The results show a substantially higher cellular uptake of the BK@AIE NPs in U87-MG cells. These results show that the BK@AIE NPs specifically recognized U87-MG cells due to the interaction between BK and B1R. Similarly, the BK-based NPs could efficiently target U87-MG tumors *in vivo* rather than astrocytes from the previous work.[46]

The intracellular delivery NPs into the target site are critical factors for influencing their potential applications in biomedicine.[47, 48] Therefore, to further monitor the location of BK@AIE NPs in the cancer cells, we conducted the co-localization analysis using U87-MG cells incubated with LysoTracker biomarkers and 4',6-diamidino-2-phenylindol (DAPI). BK@AIE NPs were labeled with Cy5.5 in **Figure 3D**, and the endo/lysosomes were stained with LysoTracker Green dyes. The most pristine AIE NPs remained inside the lysosomes after incubating with the cells for 4 h, as displayed by the yellow dots in the merged CLSM images (overlap of red and green dots). In contrast, co-localization was reduced when analyzing the BK @AIE NPs, suggesting that BK@AIE NPs accumulated mainly in the lysosomes of U87-MG cells (**Figure 3D**). The cellular internalization efficiency of BK@AIE NPs was also evaluated by a CLSM and the fluorescence intensity was analyzed using Image J. In **Figure 3E**, the cellular uptake efficiency of BK@AIE NPs strongly depends on the B1R mediated endocytosis pathway. The red fluorescence intensity emitted by Cy5.5 was stronger in the BK@AIE NPs group, which indicated a higher cellular uptake of BK@AIE NPs in U87-MG cells. However, the fluorescence intensity in the cells was weaker after treating with AIE NPs. The above results suggested that the BK@AIE NPs group not only accelerated the NPs escaping from the lysosome but also improved the internalization efficiency.

Being similar to many other indexes, the dysfunction of mitochondria has been identified as a functional marker of cell apoptosis. Therefore, the dysfunction of mitochondria in U87-MG cells caused by BK@AIE NPs under 980 nm laser irradiation was examined before further evaluation of the *in vitro* photothermal therapeutic efficacy. The mitochondrial membrane potential (MMP) was introduced to monitor the degree of damage through staining with JC-1 (**Figure 4A**). Acknowledgment of the decreasing MMP always replies to the gathering of JC-

1 monomer (green fluorescence) while the aggregation of JC-1 (red fluorescence) responds to a high MMP, which indicates a standard state. Moreover, the fluorescent shift of JC-1 from orange to green represents the occurrence of early apoptosis. As shown in **Figure 4A**, the approximate JC-1 aggregation through red fluorescence from different treatment groups suggested a negligible change of MMP in cells, as well as insignificant harm to the mitochondria. However, the sharp increase in green fluorescence in the BK@AIE NPs plus 980 nm laser group, suggesting that the mitochondria were destroyed. Hence, we comprehended that the local hyperthermia from BK@AIE NPs plus 980 nm laser treatment accounted for the dysfunction of mitochondria, which means this system could inspire an efficient antitumor process by the targeted PTT outcome and enhanced cell apoptosis.

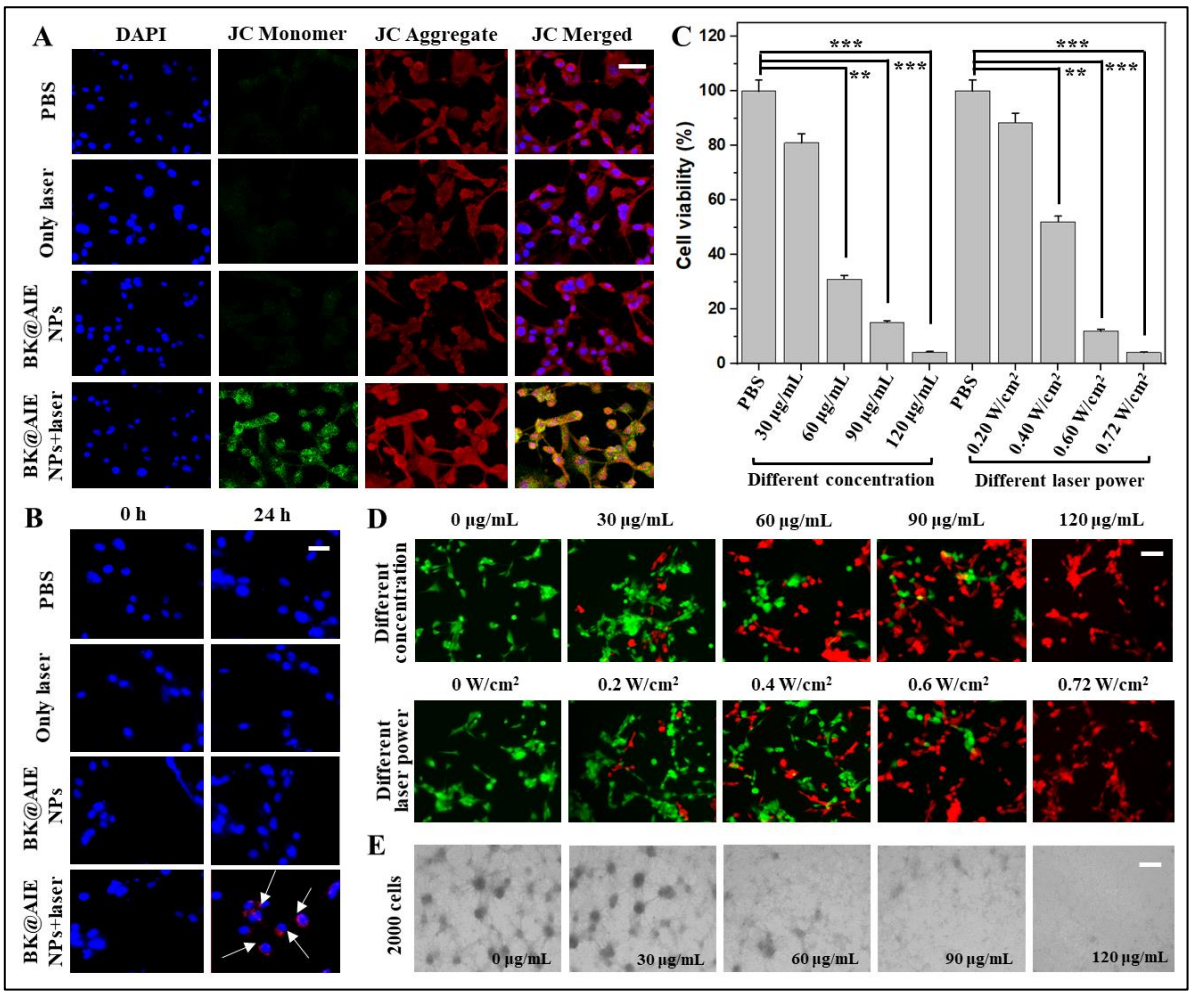

Figure 4. (A) Fluorescence images showing the MMP changes of U87-MG cells after different treatments. Scale bar: 50 μm (B) CRT expression of U87-MG cells after various treatments. Scale bar: 20 μm (C) Relative viabilities and (D) live/dead staining of U87-MG cells in different treatment groups. U87-MG cells were incubated with different concentrations of BK@AIE NPs, and then refreshed media and irradiated with the 980 nm laser (5 min, 0.72 W/cm^2). U87-MG cells were incubated with BK@AIE NPs (120 μg/mL), and then refreshed cell culture media and irradiated with the 980 nm laser at different laser power densities for 5

min. Afterward, cells were re-incubated for an additional 24 h before performing the MTT assay, $^{**}P$ <0.01 and $^{***}P$ <0.001. Scale bar: 50 μm (E) Images of formatted tumorspheres among U87-MG cells after various treatments. Scale bar: 200 μm

Recently, the immunogenic cell death (ICD) sprang up to describe the state of immunogenic apoptosis and the active immune response. One of the characteristics of ICD is the increased surface exposure of calreticulin proteins (CRT) following the extensive degree of damage. As a result, CRT exposure servers as a phagocytic calling signal to provoke an internal immune response.[49, 50] Based on this knowledge, we further investigated the PTT therapeutic effect from BK@AIE NPs plus NIR-II laser in GBM cells. Immunofluorescence assays (**Figure 4B**) showed that the higher level of CRT only occurred in the BK@AIE NPs plus laser radiation group, indicating their excellent photothermal effect. These results demonstrate that BK@AIE NPs based PTT can induce apoptosis among U87-MG cells while enhancing the release of damage-associated molecular patterns. Afterward, the *in vitro* antitumor efficiency of BK@AIE NPs was also confirmed by MTT assay, calcein-AM/PI staining, and tumorsphere formation. It was found that BK@AIE NPs treated cells showed remarkably reduced viabilities by increasing the BK@AIE NP concentration and laser power intensities (**Figure 4C**). However, incubation of U87-MG cells for 24 h without laser irradiation caused a minimal impact on the cell viability test. To investigate PTT *in vitro*, green-emissive calcein-AM and red-emissive propidium iodide (PI) staining was applied to distinguish live and dead cells, respectively (**Figure 4D**). Upon light irradiation at 980 nm for 5 min, the green fluorescence decreased upon increasing the BK@AIE NPs concentration and laser power intensities. In **Figure 4D**, almost all the cells were apoptotic/dead after treatment with 120 μg/mL BK@AIE NPs under 980 nm laser irradiation (5 min, 0.72 W/cm^2). Next, we examined tumorsphere formation of GBM cells by incubating with different concentrations of BK@AIE NPs after 980 nm laser irradiation (5 min, 0.72 W/cm^2). Treatment of U87-MG cells with BK@AIE NPs strongly inhibited their ability to form tumorspheres (**Figure 4E**). The above results indicated that the BK@AIE NPs group not only exerted their functions to kill cancer cells but also inhibited tumor recurrence.

The penetration of morbid BBB as one of the most challenging natural obstacles for drug delivery was also evaluated by constructing the U87-MG/human vascular endothelial cells (HUVECs) co-culture model. HUVECs were given angiogenesis characteristics when coexisting with U87-MG cells (**Figure 5A**). The AIE NPs and BK@AIE NPs were added to the apical chamber of the simulated morbid BBB. The agonist-mediated dynamic penetration of AIE NPs with and without BK were quantitatively evaluated by detecting the fluorescence

intensity in the basal chamber after adding these NPs into the apical chamber at various time points during 24 h. It was shown that the crossing efficiency of BK@AIE NPs changing with the morbid BBB permeability (**Figure 5A**). We monitored the morbid BBB crossing efficiency of AIE NPs and BK@AIE NPs within 24 h of post-treatment. BK@AIE NPs showed higher crossing efficiency, which was 5.3 times higher than that of AIE NPs. The results suggested that BK@AIE NPs could improve their passing amounts by upregulating morbid BBB permeability.

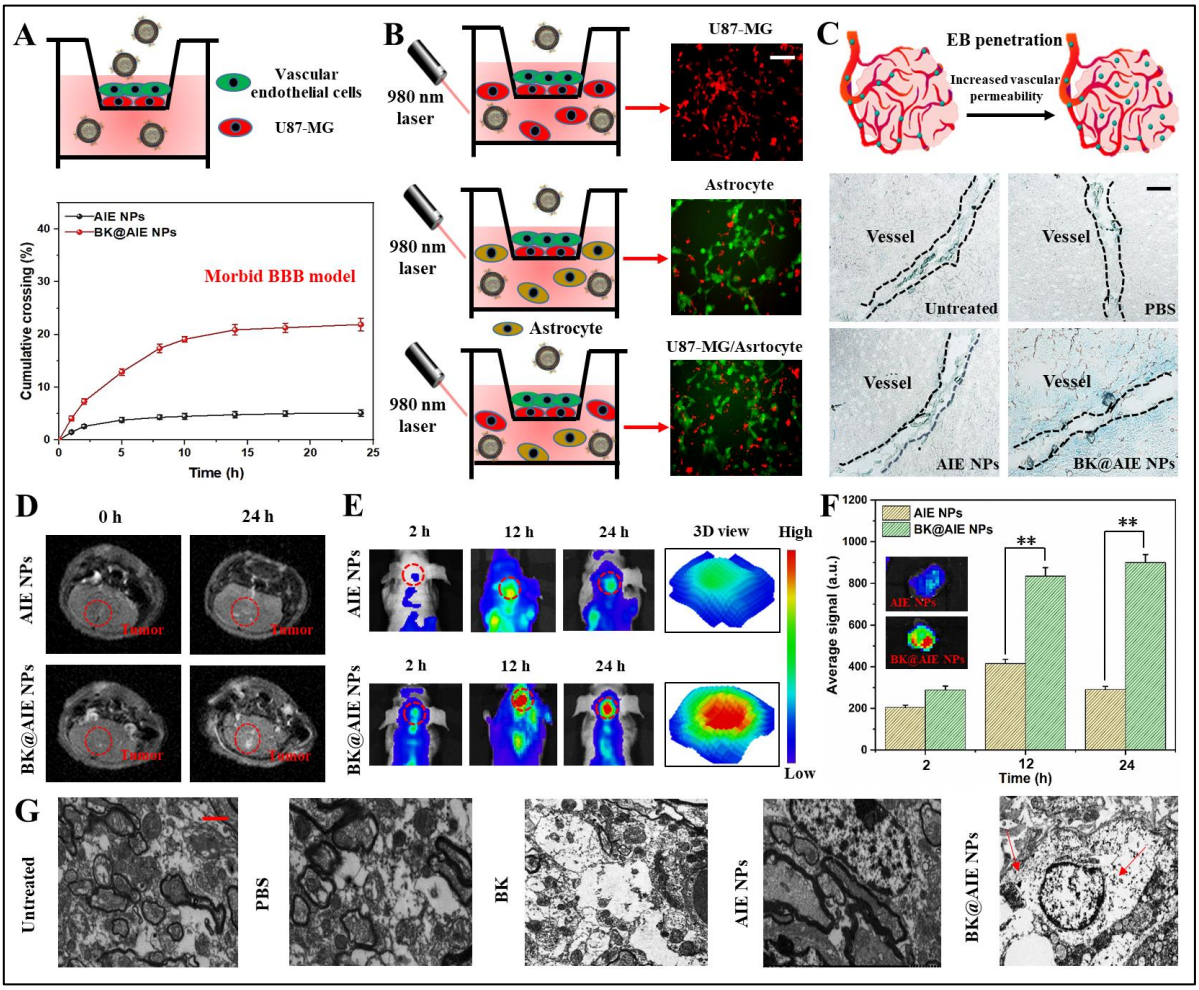

Figure 5. (A) Schematic of the transwell assay to evaluate co-cultured cell permeability. Evaluating morbid BBB crossing dynamics of AIE NPs and BK@AIE NPs (0–24 h). (B) U87-MG cells specifically targeted by the BK@AIE NPs and the astrocytes were mixed and co-cultured in the basal chamber. The viabilities of U87-MG, astrocytes/U87-MG, and astrocytes are shown after the PTT. Scale bar: 100 μm (C) EB staining of brain sections after different treatments. Scale bar: 50 μm (D) MR images for the mouse brain in different groups. (E) *In vivo* fluorescence imaging from mice at different time points after AIE NPs and BK@AIE NPs injections, respectively. (F) Quantitative fluorescence analysis in the tumor site at different time points after treating with AIE NPs and BK@AIE NPs. Inset is the fluorescence imaging of the brain after AIE NPs and BK@AIE NPs injections for 24 h, $^{**}P < 0.01$. (G) Bio-TEM images of the brain blood vessels after AIE NPs and BK@AIE NPs injections for 8 h. The red arrows represent BK@AIE NPs. Scale bar: 5 μm

Moreover, the specific targeting towards U87-MG cells and tumoricidal effects induced by NIR-II laser of the BK@AIE NPs were evaluated in the presence of astrocytes co-cultured in a basal chamber (**Figure 5B**). As the control experiment, we also plated U87-MG cells and astrocytes incubated with the BK@AIE NPs. The exposure of BK@AIE NPs-treated U87-MG cells with laser irradiation resulted in around 98% of cell loss, which was significantly higher than that of astrocytes (c.a. 49%). Interestingly, the amounts of astrocytes stayed healthy in the mixed astrocytes/U87-MG group. These results demonstrate that, with an effective cancer cell targeting molecules, PTT could serve as a precise strategy to cure GBM with minimal damage to the adjacent tissues.

To completely advance the therapy of PTT to malignant GBM, we need to overcome the restriction from morbid BBB to promote the delivery process. B1R is spontaneously introduced to our system as it is reported to regulate the microstructure of brain tumors by changing the permeability of vessels. Therefore, we studied the capability of BK@AIE NPs to temporarily modulate morbid BBB permeability *in vivo* by monitoring ethidium bromide (EB) penetration. EB extravasation represents serum albumin extravasation from blood vessels as they stably interplay with each other.[51] Mice were intravenously injected with AIE NPs or BK@AIE NPs, following by subsequent injection of EB. After 6 h, the mice brains were separated and used for performing histologic analysis. We found that the BK@AIE NPs treatment significantly enhanced the morbid BBB permeability, resulting in EB vascular penetration and a more homogeneous distribution of EB within the tumor interstitium (**Figure 5C**). We also noted that AIE NPs and PBS treatment could not enhance EB vascular penetration and improve their distribution profile. These results suggested that the morbid BBB permeability could only be improved under the treatment of BK@AIE NPs. It might be associated with the binding of B1R agonists (BK) to their receptors in brain tumor areas. This interaction results in increased permeability of morbid BBB by inspiring a set of secondary reactions and expression of related proteins in the transcellular or paracellular pathway.

In our current and various previous studies, we identified that gadolinium ion (Gd^{3+}) anchored on NPs produced by the ion complexation can provide strong contrast for magnetic resonance (MR) imaging.[52, 53] After intravenous injection of AIE NPs and BK@AIE NPs into U87-MG tumor-bearing mice, a remarkably bright appearance was detected in the tumor region with *in vivo* MR imaging, which attributed to the high tumor accumulation of NPs after systematic administration (**Figure 5D**). It was observed that the MR signal was about twofold higher in the BK@AIE NPs group, which gave clear evidence that BK played the key role in

crossing morbid BBB *in vivo*. The MR signal in the AIE NPs group benefits from the EPR effect, as compared to that of the BK@AIE NP group. The quantitative analysis of the region of interest (ROI) is shown in the MR imaging way (**Figure S6**).

Next, we evaluated the active crossing ability of BK@AIE NPs *in vivo* by intravenous injection with an orthotopic U87-MG tumor-bearing mice model. In **Figure 5E**, the higher fluorescence signal in the BK@AIE NP group suggested the excellent targeting ability of BK. Meanwhile, it also proved that the conjugation of BK made up for the limited penetration from the morbid BBB to the passive accumulation of AIE NPs from the EPR effect. The quantitative analysis for the brain accumulation of BK@AIE NPs and AIE NPs is shown in **Figure 5F**. Remarkably, the average signal in tumors achieved an almost threefold higher effect in the BK@AIE NPs treatment group after 24 h. These results validated that BK@AIE NPs have prominently enhanced morbid BBB penetration and tumor accumulation. Furthermore, we studied the *in vivo* behavior of BK@AIE NPs using animals. Prolonged circulation of NPs in the bloodstream is essential to improve the probability of entering the tumor and accumulation therein. We intravenously injected BK@AIE NPs into the U87-MG-bearing mice. To further verify that nanoparticles increase the permeability of blood vessels and cross the morbid BBB, biological TEM was used to observe the internal structure of blood vessels in the brain. Compared with the AIE NP group, we observed that the vascular tissues in BK and BK@AIE NP groups were relatively loose. As expected, the BK@AIE NPs are concentrated in the intercellular space (**Figure 5G**). Besides, the behavior of BK@AIE NPs in blood was detected at different time points during 24 h after the injection. It seemed that they were still at a reasonably high level after 24 h, even in spite of the general gradually downward trend (**Figure S7**).

We next evaluated the feasibility of PTT using BK@AIE NPs in conventional xenograft tumor mice. U87-MG cells were inoculated into the right oxter of female BALB/c nude mice as a conventional xenograft tumor model. The infrared thermal camera was applied to record the local temperature in tumor sites to supply evidence of the substantially higher ability of PTT from AIE NPs. Meanwhile, the conjugated BK endowed more AIE NPs to gather the tumor site, which assumed a hyperthermal effect with a local tumor temperature of 52.8 °C under NIR-II exposure for 5 min while the AIE NPs group was around 49 °C (**Figure 6A, S8**). These observations demonstrated that our BK@AIE NPs could successfully target brain tumor cells. To further evaluate the PTT efficiency, BK@AIE NPs, AIE NPs, and PBS were intravenously injected at predetermined times, respectively. After 24 h, 980 nm laser (0.72

W/cm^2) was used to irradiate the tumor sites for 5 min to assess the impacts from the laser irradiation to tumor propagation. As a result, only irradiation of NIR-II laser did not cause tumor suppression (**Figure 6B**). Moreover, tumor volumes were recorded under different treatments showing that the growth of tumors could be inhibited by the individual PTT effect from the NIR-II laser (**Figure S9A**). However, a more remarkable decrease occurred in the BK@AIE NPs plus NIR-II laser group, this result was also reflected in the tumor volumes measurement during 18 days.

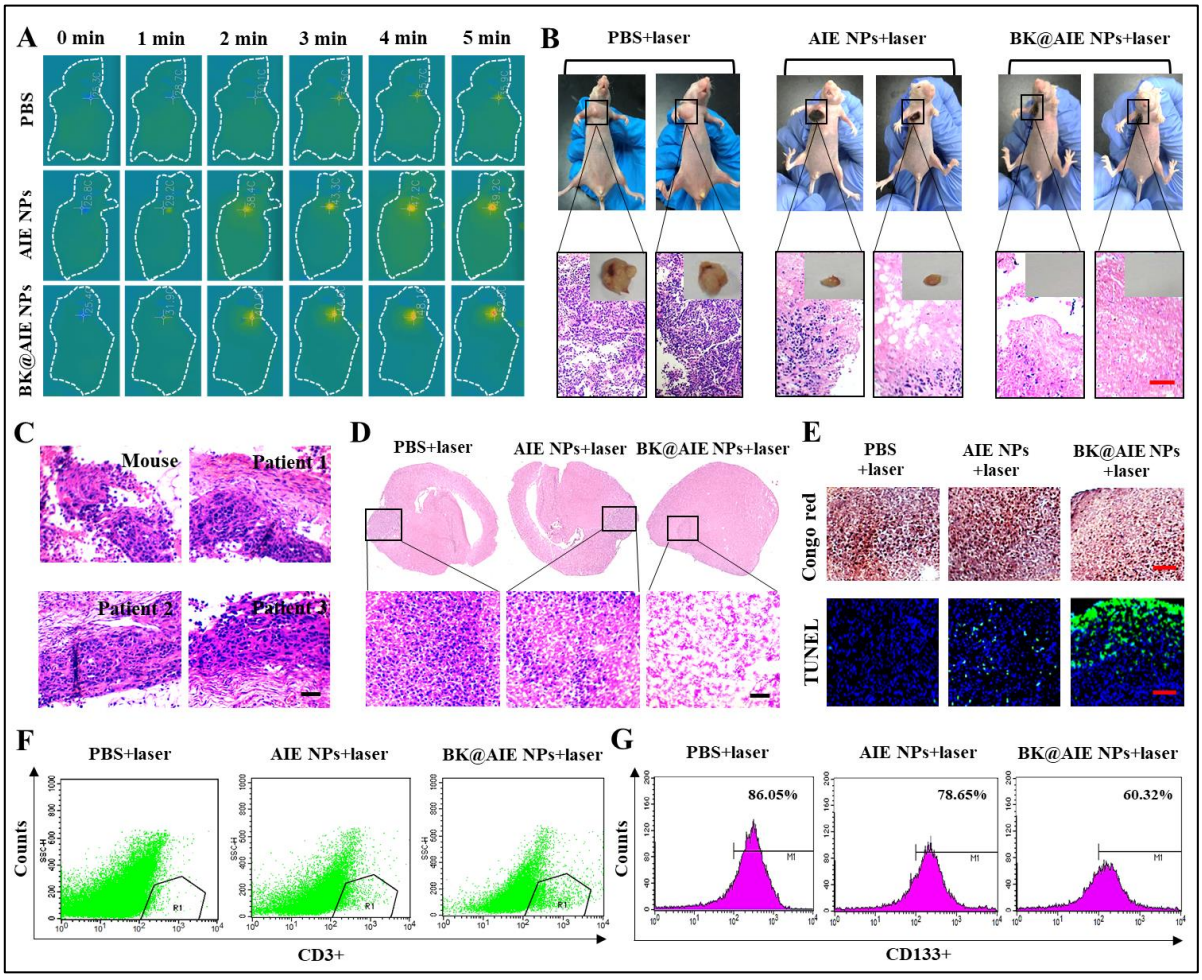

Figure 6. (A) Infrared thermographic maps of tumors in the mice were measured 5 min after continuous laser irradiation (980 nm, 0.72 W/cm^2). (B) Representative photos of U87-MG-bearing mice treated with PBS, AIE NPs, and BK@AIE NPs following by NIR-II laser irradiations. Scale bar: 100 μm (C) Histological observations of brains of orthotopic GL261-bearing mice and GBM patients. Scale bar: 100 μm (D) Histological observations of brains of orthotopic GL261-bearing mice treated with PBS plus laser, AIE NPs plus laser, and BK@AIE NPs plus laser. Scale bar: 100 μm (E) Congo red and TUNEL staining of brains of orthotopic GL261-bearing mice treated with PBS plus laser, AIE NPs plus laser, and BK@AIE NPs plus laser. Scale bar: 100 μm (F) Quantification of the intratumoral proliferation of CD3+ T cells by flow cytometric. (G) Histograms illustrating the percentage of annexin V expression in CD133+ cancer stem cells (CSCs).

The responding histological analysis of tumor tissues in every treatment group was performed to deeply understand the therapeutic effect. As shown in **Figure S9B**, obvious cytoplasmic leakage and nuclear shrinkage of apoptotic cells were observed in the H&E stained tumor slices from the BK@AIE NPs and PTT treated group. As an available therapeutic agent, the bio-safety of BK@AIE NPs also needed to be assessed. Body weights, identified as an assessment index, were recorded in all the groups during the therapeutic process, which represented the extent of side effects on mice (**Figure S10**). As recorded, mice in different groups slightly increased after 18 days, referring to a healthy life cycle. In **Figure S11**, H&E staining analysis for the major organs agreed with the above results, as no group showed necrosis or morphology changes. As a conclusion, we demonstrated that the fabricated BK@AIE NPs exerted no obvious *in vivo* toxicity.

In addition, the *in vivo* therapeutic effect of BK@AIE NPs was evaluated in orthotopic brain tumor models, which were constructed by inoculating glioblastoma 261 (GL261) cells into the striatum of female C57BL/6 mice. The successful establishment of tumor models was verified by comparing the pathological sections of patients and mice (**Figure 6C**). The patient's tumor tissue was similar to that of mice. Mice bearing orthotopic GBM were treated with various solutions and then exposed to laser irradiation (980 nm, 0.72 W/cm^2) for 5 min (**Figure S12A**). By recording the temperature of the tumor sites, we observed increased temperature of more than 15 °C only in the BK@AIE NPs plus laser treatment group (**Figure S12B**). AIE NPs plus laser and PBS plus laser groups were used as control (n = 10 per group). The high therapeutic effect of BK@AIE NPs plus laser group was also confirmed by histological staining, exhibiting the most apoptosis of tumor cells and a reduction in proliferation (**Figure 6C, D**). Moreover, the strong tumoricidal ability of BK@AIE NPs plus laser treatment was also identified in the H&E and Congo red staining results, in which nearly the whole tumor tissue disappeared, consistent with the tumor margin analysis of TUNEL staining (**Figure 6E**). The obviously strong green fluorescence signal presented due to the increase in apoptotic cells in tumor tissue, while cells around the normal tissue stayed normal, verifying the minimal damage of PTT to the healthy cells. The survival time of GBM bearing mice under different treatments was also measured to evaluate the anti-GBM efficacy in **Figure S13**. The medium survival time of BK@AIE NPs plus laser was 48 days, suggesting that BK@AIE NPs plus laser significantly extended animal survival time in comparison with PBS plus laser (25 days) and AIE NPs plus laser (30 days). These results indicated that BK conjugated AIE NPs

demonstrated a desirable therapeutic effect here that could serve as a promising drug delivery system for glioblastoma treatment.

Accordingly, PTT-induced dead cancer cells release tumor-derived antigens could stimulate the host immune system, lead to acute inflammation and leukocyte infiltration to tumors, inspire T cells, M1 MΦ, and NK cells.[54, 55] Oxaliplatin was generally used to induce ICD in mouse colorectal cancer models.[56, 57] The brain tumors near the endpoint of mice after PTT were harvested to further investigate the local immune response. CD3+ T cells, M1 MΦ, and NK cells were revealed by flow cytometry. The percentage of infiltrating CD3+ T cells (**Figure 6F**) concerning the whole cells in the tumors sharply increased in mice with BK@AIE NPs plus laser treatment. Activation of brain immunity contributed to a significant growth in tumor M1 MΦ and NK cells. Particularly, M1 MΦ-generated iNOS is responsible for the tumoricidal effect. Therefore, the immunohistochemical analysis of the anti-tumor marker iNOS was also measured using tumor slices after various treatments (**Figure S14**). The signals of the M1 MΦ marker iNOS showed a significant increase after BK@AIE NPs plus laser treatment compared with AIE NPs plus laser or PBS plus laser. In addition, NK cells, known as "tumor killers", also increased after the BK@AIE NPs plus laser treatment vs. PBS plus laser or AIE NPs plus laser, respectively (**Figure S15**).

As a result of the inspired immune system, series of representative cytokines of T cells in the serum that regulates immune responses including IL-2, IL-10, IL-12, IL-1β, IFNγ, and TNFα significantly increased after treating with BK@AIE NPs plus laser compared to AIE NPs plus laser or PBS plus laser (**Figure S16**). In general, IL-1β, IL-12, IFNγ, and TNFα belong to the T helper 1 (Th1) response when IL-10 belongs to the T helper 2 (Th2) response. IL-2 secretion inspires T and B lymphocyte activity, improves tumoricidal immunity, activates microglia, and regulates Tregs. The cytotoxic immune response was promoted by IFNγ, which was mainly generated by CD3+ cells, and NK cells. The microglia-secreted IL-12 could activate NK cells, and stimulate T cells during the self-stimulating circuit. While IL-10 is a multifunctional immune cytokine with antiangiogenic properties. Cytokines such as TNFα can stimulate a cell-mediated humoral immune reaction and ultimately inhibit tumor proliferation. As a local PTT, BK@AIE NPs also enhances antitumor immunity via three pathways. Firstly, PTT of AIE NPs could promote the generation of chemokines and cytokines, thereby stimulating the systemic immune response to exerting antitumor activity. The obvious increase in pro-inflammatory cytokines after PTT treatment induces acute inflammation, suggesting the occurrence of an inspired innate immune response. Secondly, PTT was identified to induce the

CNS and thus activates the immune system. Thirdly, the PTT of BK@AIE NPs kills GBM cells by both necrosis and apoptosis. Then the dead tumor cells would be engulfed by innate immune effector cells, which could specifically present tumor-derived antigenic peptides to T cells to stimulate the corresponding T-cell response.

For standard treatments of chemo and radiotherapy, CSCs are inherently refractory and play a role in key aspects of disease propagation including primary tumor expansion and tumor metastasis.[58, 59] The current challenge for ablating this key subgroup can be attributed to tumor recurrence. Fortunately, heat-mediated cancer treatments represent an attractive possibility for ablating CSCs. To confirm that stem cells had a sensitivity to PTT of BK@AIE NPs, the surviving fraction was analyzed by flow cytometry. The results are shown in **Figure 6G**. As expected, treatment with PBS plus laser had no significant impact on all the CD133+ cell subpopulations. AIE NPs plus laser reduced the average percentage of CD133+ cell subpopulations compared to PBS plus laser. However, the BK@AIE NPs plus laser could significantly reduce the percentage of cell subpopulations. These results demonstrated that BK@AIE NPs-mediated hyperthermia could serve as an advanced therapy for the elimination of stem cells and bulk brain cancer cells.

Conclusions

In summary, we have developed a multifunctional biocompatible nanoplatform based on BK coated AIE NPs, which could (i) specifically target the brain tumor, (ii) penetrate through the morbid BBB, (iii) perform PTT, and (iv) simultaneously activate the local immune system for a very effective synergetic brain cancer therapy. *In vivo* bimodal fluorescence and MR imaging verified the significant tumor accumulation of BK@AIE NPs. *In vivo* excellent tumor inhibition effect of PTT from BK@AIE NPs was realized by systematic administration of the animal tumor models. With the advantages like the temporary modulation of morbid BBB permeability, GBM cells could be specifically targeted, followed by a rapid increase in the local temperature of the brain tumor with minimal harm to surrounding normal tissue. *In vivo,* BK@AIE NPs-mediated PTT showed a significant effect in both eliminating tumor cells for releasing antigens in the local microenvironment and instigating an inflammatory response for recruiting immune cells into the region. BK@AIE NPs-mediated PTT is thus an apt tool for activating the immune system of the brain. Moreover, BK@AIE NPs-mediated PTT could eliminate CSCs inside tumors in mouse models, the root of cancer recurrence associated with conventional therapy, for cancer treatment with highly improved efficacy.

Supporting Information

Supporting Information is available from the Wiley Online Library or from the author.

Acknowledgements

This work is supported by the Villum Fonden, Denmark, Project No. 13153. We are also grateful for the financial support from the Research Grant Council of Hong Kong (16305518 and C6009-17G).

Conflict of Interest

The authors declare no conflict of interest.

Keywords: photothermal therapy, glioblastoma, magnetic resonance, immune response

[1] G. Deng, X. Peng, Z. Sun, W. Zheng, J. Yu, L. Du, H. Chen, P. Gong, P. Zhang, L. Cai, *ACS Nano* **2020**, *14*, 11452.
[2] C. H. Fan, E. L. Chang, C. Y. Ting, Y. C. Lin, E. C. Liao, C. Y. Huang, Y. C. Chang, H. L. Chan, K. C. Wei, C. K. Yeh, *Biomaterials* **2016**, *106*, 46.
[3] B. Guo, Z. Sheng, D. Hu, C. Liu, H. Zheng, B. Liu, *Adv. Mater.* **2018**, *30*, 1802591.
[4] B. Fazi, C. Proserpio, S. Galardi, F. Annesi, M. Cola, A. Mangiola, A. Michienzi, S. A. Ciafrè, *Int. J. Mol. Sci.* **2019**, *20*, 2496.
[5] G. D. Cha, T. Kang, S. Baik, D. Kim, S. H. Choi, T. Hyeon, D. H. Kim, *J. Control. Release* **2020**, *328*, 350.
[6] Y. Liu, Y. Zou, C. Feng, A. Lee, J. Yin, R. Chung, J. B. Park, H. Rizos, W. Tao, M. Zheng, *Nano Lett.* **2020**, *20*, 1637.
[7] Z. Z. Yang, W. Gao, Y. J. Liu, N. Pang, X. R. Qi, *Mol. Pharm.* **2017**, *14*, 1012.
[8] G. Morad, C. V. Carman, E. J. Hagedorn, J. R. Perlin, L. I. Zon, N. Mustafaoglu, T. E. Park, D. E. Ingber, C. C. Daisy, M. A. Moses, *ACS Nano* **2019**, *13*, 13853.
[9] L. M. Liau, R. M. Prins, S. M. Kiertscher, S. K. Odesa, T. J. Kremen, A. J. Giovannone, J. W. Lin, D. J. Chute, P. S. Mischel, T. F. Cloughesy, *Clin. Cancer. Res.* **2005**, *11*, 5515.
[10] M. N. Oliveira, B. Breznik, M. M. Pillat, R. L. Pereira, H. Ulrich, T. T. Lah, *Cancer Microenviron.* **2019**, *12*, 77.
[13] F. Marceau, J. F. Hess, D. R. Bachvarov, *Pharmacol. Rev.* **1998**, *50*, 357.
[11] J. Côté, V. Bovenzi, M. Savard, C. Dubuc, A. Fortier, W. Neugebauer, L. Tremblay, W. Müller-Esterl, A. M. Tsanaclis, M. Lepage, *PLoS One* **2012**, *7, 37485*.
[12] L. F. Leeb-Lundberg, F. Marceau, W. Müller-Esterl, D. J. Pettibone, B. L. Zuraw, *Pharmacol. Rev.* **2005**, *57*, 27.
[14] M. Simonelli, L. Di Tommaso, M. Baretti, A. Santoro, *Immunotherapy* **2016**, *8*, 1363.
[15] I. Guevara Lora, B. Błońska, A. Faussner, A. Kozik, *Acta Biochim. Pol.* **2013**, *60*, 299.
[16] D. Y. Lu, Y. M. Leung, S. M. Huang, K. L. Wong, *J. Cell. Biochem.* **2010**, *110*, 141.
[17] Y. Zhang, Y. Lu, F. Wang, S. An, Y. Zhang, T. Sun, C. Jiang, *Small* **2017**, *13*, 1602494.
[18] G. P. Skandalakis, D. R. Rivera, C. D. Rizea, A. Bouras, J. G. Jesu Raj, D. Bozec, C. G. Hadjipanayis, *Int. J. Hyperth.* **2020**, *37*, 3.
[19] A. M. Mohammadi, A. H. Hawasli, A. Rodriguez, J. L. Schroeder, A. W. Laxton, P. Elson, E. C. Leuthardt,. *Cancer med.* **2014**, *3*, 971.
[20] X. Wang, Z. Li, Y. Ding, K. Wang, Z. Xing, X. Sun, W. Guo, X. Hong, X. Zhu, Y. Liu, *Chem. Eng. J.* **2020**, *381*, 122693.
[21] M. Ma, N. Gao, X. Li, Z. Liu, Z. Pi, X. Du, J. Ren, X. Qu, *ACS Nano* **2020**, *14*, 9894.
[22] S. B. Lakshmanan, X. Zou, M. Hossu, L. Ma, C. Yang, W. Chen, *J. Biomed. Nanotechnol.* **2012**, *8*, 883.
[23] C. Yang, L. Ma, X. Zou, G. Xiang, W. Chen, *Cancer Nanotechnol.* **2013**, *4*, 81.

[24] K. Wu, H. Zhao, Z. Sun, B. Wang, X. Tang, Y. Dai, M. Li, Q. Shen, H. Zhang, Q. Fan, *Theranostics* **2019**, *9*, 7697.
[25] Q. Jiang, Y. Liu, R. Guo, X. Yao, S. Sung, Z. Pang, W. Yang, *Biomaterials* **2019**, *192*, 292.
[26] M. Gao, B. Z. Tang, *Drug Discov. Today* **2017**, *22*, 1288.
[27] D. Wang, H. Su, R. T. Kwok, X. Hu, H. Zou, Q. Luo, M. M. Lee, W. Xu, J. W. Lam, B. Z. Tang, *Chem. Sci.* **2018**, *9*, 3685.
[28] G. Feng, J. Liu, C. J. Zhang, B. Liu, *ACS Appl. Mater. Interfaces* **2018**, *10*, 11546.
[29] J. A. Li, J. Zhou, Z. Mao, Z. Xie, Z. Yang, B. Xu, C. Liu, X. Chen, D. Ren, H. Pan, *Angew. Chem. Int. Ed.* **2018**, *130*, 6559.
[30] S. Liu, C. Chen, Y. Li, H. Zhang, J. Liu, R. Wang, S. T. Wong, J. W. Lam, D. Ding, B. Z. Tang, *Adv. Funct. Mater.* **2020**, *30*, 1908125.
[31] Y. Cai, W. Si, W. Huang, P. Chen, J. Shao, X. Dong, *Small* **2018**, *14*, 1704247.
[32] H. S. Jung, P. Verwilst, A. Sharma, J. Shin, J. L. Sessler, J. S. Kim, *Chem. Soc. Rev.* **2018**, *47*, 2280.
[33] S. Liu, X. Zhou, H. Zhang, H. Ou, J. W. Lam, Y. Liu, L. Shi, D. Ding, B. Z. Tang, *J. Am. Chem. Soc.* **2019**, *141*, 5359.
[34] S. Liu, Y. Li, H. Zhang, Z. Zhao, X. Lu, J. W. Lam, B. Z. Tang, *ACS Mater. Lett.* **2019**, *1*, 425.
[35] Y. Li, R. T. Kwok, J. W. Y. Lam, B. Z. Tang, *Chem. Sci.* **2020**, *12*, 3427.
[36] Z. Zhang, W. Xu, M. Kang, H. Wen, H. Guo, P. Zhang, L. Xi, K. Li, L. Wang, D. Wang, *Adv. Mater.* **2020**, *32*, 2003210.
[37] Q. Li, Z. Li, *Adv. Sci.* **2017**, *4*, 1600484.
[38] L. Ma, X. Feng, S. Wang, B. Wang, *Mater. Chem. Front.* **2017**, *1*, 2474.
[39] Q. Chen, L. Xu, C. Liang, C. Wang, R. Peng, Z. Liu, *Nat. Commun.* **2016**, *7*, 1.
[40] D. Zhang, T. Wu, X. Qin, Q. Qiao, L. Shang, Q. Song, C. Yang, Z. Zhang, *Nano Lett.* **2019**, *19*, 6635.
[41] W. Chen, M. Qin, X. Chen, Q. Wang, Z. Zhang, X. Sun, *Theranostics* **2018**, *8*, 2229.
[42] F. Salehpour, P. Cassano, N. Rouhi, M. R. Hamblin, L. De Taboada, F. Farajdokht, J. Mahmoudi, *Photobiomodulation, Photomed., Laser Surg.* **2019**, *37*, 581.
[43] M. R. Hamblin, *J. Neurosci. Res.* **2018**, *96*, 731.
[44] X. E. Zhou, Y. He, P. W. de Waal, X. Gao, Y. Kang, N. Van Eps, Y. Yin, K. Pal, D. Goswami, T. A. White, *Cell* **2017**, *170*, 457.
[45] C. J. Hutchings, M. Koglin, W. C. Olson, F. H. Marshall, *Nat. Rev. Drug Discovery* **2017**, *16*, 787.
[46] Y. Jiang, L. Lv, H. Shi, Y. Hua, W. Lv, X. Wang, H. Xin, Q. Xu, *Colloids Surf. B. Biointerfaces* **2016**, *147*, 242.
[47] D. Pei, M. Buyanova, *Bioconj. Chem.* **2018**, *30*, 273.
[48] J. Chen, J. Li, J. Zhou, Z. Lin, F. Cavalieri, E. Czuba-Wojnilowicz, Y. Hu, A. Glab, Y. Ju, J. J. Richardson, *ACS Nano* **2019**, *13*, 11653.
[49] S. N. Sethuraman, M. P. Singh, G. Patil, S. Li, S. Fiering, P. J. Hoopes, C. Guha, J. Malayer, A. Ranjan, *Theranostics* **2020**, *10*, 3397.
[50] Y. Li, X. Liu, W. Pan, N. Li, B. Tang, *Chem. Commun.* **2020**, *56*, 1389.
[51] R. Abbas, X. Zhihui, E. C. Chan, C. Wei-Sheng, L. M. Scott, E. A. Robin, D. N. Krementsov, H. F. Rosenberg, S. M. Parikh, E. P. Blankenhorn, *Commun. Biol.* **2019**, *2*, 398.
[52] T. J. Clough, L. Jiang, K. L. Wong, N. J. Long, *Nat. Commun.* **2019**, *10*, 1.
[53] M. Zhang, W. Wang, F. Wu, P. Yuan, C. Chi, N. Zhou, *Carbon* **2017**, *123*, 70.
[54] M. Li, S. Li, H. Zhou, X. Tang, Y. Wu, W. Jiang, Z. Tian, X. Zhou, X. Yang, Y. Wang, *Nat. Commun.* **2020**, *11*, 1.
[55] V. Duhan, T. A. Hamdan, H. C. Xu, P. Shinde, H. Bhat, F. Li, Y. Al-Matary, D. Häussinger, J. Bezgovsek, S. K. Friedrich, *PLoS Pathog.* **2019**, *15*, 1007797.
[56] T. Flieswasser, J. Van Loenhout, L. Freire Boullosa, A. Van den Eynde, J. De Waele, J. Van Audenaerde, F. Lardon, E. Smits, P. Pauwels, J. Jacobs, *Cells* **2020**, *9*, 1474.
[57] A. Rossi, O. N Pakhomova, P. A. Mollica, M. Casciola, U. Mangalanathan, A. G Pakhomov, C. Muratori, *Cancers (Basel)* **2019**, *11*, 2034.
[58] T. Brabletz, A. Jung, S. Spaderna, F. Hlubek, T. Kirchner, *Nat. Rev. Cancer* **2005**, *5*, 744.
[59] A. R. Burke, R. N. Singh, D. L. Carroll, J. C. Wood, R. B. D'Agostino Jr, P. M. Ajayan, F. M. Torti, S. V. Torti, *Biomaterials* **2012**, *33*, 2961.

Supporting Information for PAPER II

Experimental Section

Materials. Unless otherwise stated, all reagents were obtained from Sigma-Aldrich Co. (St Louis, MO, USA). 3-(4,5-dimethyl-2-thiazolyl)-2,5-diphenyl-2-Htetrazolium bromide (MTT), phenethyl isothiocyanate, DSPE-PEG(2000)carboxylic acid, 4',6-diamidino-2-phenylindole (DAPI), hydroxy-2,5-dioxopyrrolidine-3-sulfonicacid sodium salt (NHS), and 1-Ethyl-3-[3-dimethylaminopropyl]carbodiimide hydrochloride (EDC) were used in this study. Terminal deoxynucleotidyl transferase dUTP nick end labeling (TUNEL) assay kit was purchased from KeyGEN BioTECH (Nanjing, China). Mitochondrial membrane potential assay kit (JC-1) and ER Tracker Red were purchased from Beyotime (Shanghai, China). All the other reagents were purchased from Sigma-Aldrich Co. (St Louis, MO, USA).

Instruments and Characterization. The morphology of samples was studied by employing a transmission electron microscope (TEM, Tecnai G2 F30 S-TWIN). Ultraviolet -Visible (UV-Vis) spectra were collected on a Lambda 25 spectrophotometer (PerkinElmer Inc., Waltham, MA, USA). The hydrodynamic diameter of samples were measured with a Zetasizer (Nano ZSP; Malvern Instruments, Malvern, UK). *In vitro* bright field and fluorescence images were performed with a confocal laser scanning microscopy (CLSM, LTI-EA1R, Nikon, Japan). To monitor the temperature changes at the tumor site during irradiation, infrared thermal images were recorded with a PTT monitoring system MG33 (Shanghai Magnity Electronics Co. Ltd).

Preparation of AIE NPs. BBT-C6T-DPA(OMe) (0.5 mg) and DSPE-PEG(2000)carboxylic acid (1 mg) were completely dissolved in THF (1 mL). Subsequently, the mixture was rapidly poured into DI water (10 mL). Sonication was used to vigorously disperse the organic components in water for about 2 min. The suspension was further stirred in a fume hood for two days. Finally, the suspension was filtered using a membrane filter (0.22 μm) and subsequently washed and concentrated to a concentration of 1.0 mg/mL.

Preparation of BK@AIE NPs. AIE NPs were sonicated for 1 min in a bath sonicator. An equal volume of EDC·HCl in water (4 mg/mL) was added and the solution was mixed at RT for 5 min. A solution of des-arg^9-Bradykinin (BK) (0.5 mg) in water (0.5 mL) was added into the AIE NPs suspension and further stirred for 12 h. To remove unreacted free des-arg^9-Bradykinin, the NPs suspension was dialyzed against DI water for three days. The mixture was vortexed briefly, frozen in liquid N_2, then lyophilized using a FreeZone 2.5 L Freeze Dry System.

In Vitro Penetration Ability of 808 and 980 nm Laser. For the penetration experiment, 808 and 980 nm lasers at the same power (0.72 W/cm^2) were used directly to irradiate the subject (such as chicken tissues with different thickness, skull, skull and scalp). A photometer was located under the subject to test the power density of the light which penetrated through the subjects.

Photothermal Performance of BK@AIE NPs. Measurement of photothermal performance: aqueous-dispersion BK@AIE NPs (1.0 mL) with different concentrations (0-120 μg/mL) were introduced in a quartz cuvette and irradiated with 980 nm laser at a power density of 0.72 W/cm^2 for 5 min. The BK@AIE NPs (100 μg/mL) was irradiated by laser power densities (0.72 W/cm^2) to investigate the laser power density effect for studying the photothermal conversion performance. The temperature was recorded every 1 s by a digital thermometer using a thermocouple probe. Real-time thermal imaging of the samples was recorded using a thermal infrared camera and was quantified by examiner software.

Cell Culture. Malignant glioblastoma cells (U87-MG), Glioblastoma 261 cells (GL261), human cervical cancer cell (HeLa cells), human astrocytes, and vascular endothelial cells were cultured in a DMEM medium containing 10 % FBS and 1 % streptomycin and penicillin. Cells were incubated in an incubator (37 °C, 5 % CO_2). The culture medium was changed every 2 days and then the cells were collected by treated with 0.25% trypsin-EDTA solution after reaching confluence.

Localization of BK@AIE NPs in U87-MG Cells. To show the process of NPs escape lysosomes, U87-MG cells were treated with BK@AIE NPs for 4 h at 37°C. Subsequently, the cells were treated with LysoTracker green (50 nM, diluted in DMEM) for 60 min and Hoechst 33342 (10 mg/mL) for 15 min to stain, respectively. The lysosomes and the nucleus were kept in a dark room. Finally, the cells were washed three times with ice-cold PBS for a CLSM visualization.

Mitochondrial Membrane Potential Change. U87-MG cells were cultured with BK@AIE NPs solution (100 μg/mL) in the cell culture medium for 2 h. Then the cells were irradiated under 980 nm laser (0.72 W/cm^2) for 5 min. Cells treated with BK@AIE NPs solution without irradiation were used as control. Afterward, the medium was removed and the JC-1 staining solution was added according to the manufacturer protocol. After staining for 30 min, cells were washed and imaged under a CLSM.

Immunofluorescence. For surface detection of CRT, 5 ×10^5 of U87-MG cells were seeded in 24-well plates for overnight. Then cells were cultured with BK@AIE NPs solution (100 μg/mL) in cell culture medium for 2 h. Then the cells were irradiated under 980 nm laser (0.72 W/cm^2) for 5 min. Cells treated with BK@AIE NPs solution without irradiation were used as control. Then, cells were fixed with 4% formaldehyde for 15 min, permeabilized with 0.5% Triton X-100 for 20 min, blocked with 1.5% Bovine Serum Albumin (BSA) for 1 h. Cells were washed three times in cold Hank's, and incubated with rabbit anti-CRT antibody (ab2907, Abcam) (1:100) was added for 1 h incubation. After three washes in cold Hank's, the cells were incubated with goat anti-rabbit IgG H&L (Alexa Fluor® 594) (ab150080, Abcam) (1:200) for more 1 h. Subsequently, the cells were stained with DAPI (1:500) for 15 min. Finally, the cells were washed three times with ice-cold PBS for CLSM visualization.

For detection of iNOS, 5 ×10^5 of RAW 264.7 cells were seeded in 24-well plates for overnight. Then cells were treated as the above groups. Cells were treated as the same above protocol, but incubated with the rabbit anti-iNOS antibody [EPR16635] (ab178945, Abcam) (1:100) for iNOS detection.

Cell Cytotoxicity. MTT assay was used to test the cell viability of various samples. In brief, U87-MG cells were seeded into 96-well plates at 2 × 10^4/well. After attaching for 24 h, cells were incubated with different concentrations of BK@AIE NPs for 24 h. Afterward, each well was added with MTT solution (50 μL, 2 mg/mL). HeLa cells were incubated with BK@AIE NPs for 1.5 h, and then irradiated with different power NIR light for 5 min. After additional incubation, the cell viability was measured by MTT assay. After 4 h, the supernatant was discarded and each well was added into 150 μL DMSO. A microplate reader was used to testing the OD at 570 nm.

The antitumor efficacy was further studied through live/dead staining. After antitumor treatments, the cell culture medium was discarded. Then fresh medium containing Calcein-AM (5 μg/mL) and PI (10 μg/mL) was added. After cultured for 20 min, the cells were washed with PBS and imaged on a CLSM.

Hemolysis Test and the Shape of Erythrocytes. Erythrocytes were acquired by centrifuging 5 mL whole blood with anticoagulation at 3000 rpm for 8 min. Ablution of erythrocytes was used by PBS and then resuspended in PBS at a volume ratio of 1:9. Afterward, 1.2 mL of BK@AIE NPs solutions with different concentrations were mixed with 0.3 mL of the attenuated erythrocytes suspension. Positive and negative controls were acquired by mixing 1.2 mL of

deionized water and PBS with 0.3 mL of the attenuated erythrocytes suspension, respectively. All mixtures were maintained at 37 °C for 3.5 h and then centrifuged at 3000 rpm for 8 min. A microplate reader (BioTek Synergy 2) was used to measure the optical density (O.D.) of the samples at 541 nm. The calculating equation of the hemolysis rate was as follow[2]:

$$\text{Hemolysis rate (\%)} = [(OD_{sample} - OD_{negative}) / (OD_{positive} - OD_{negative})] \times 100\%.$$

$O.D._{sample}$, $O.D._{positive}$, and $O.D._{negative}$ represent the absorption values of the sample, positive control, and negative control, respectively. Light microscopy (Nanjing Jiangnan Novel Optics Co., Ltd, BM2100) was used for observing the shape of erythrocytes. 1.2 mL of BK@AIE NPs solutions (in PBS) with different concentrations were incubated with 0.3 mL of the attenuated erythrocytes suspension in tubes for 3.5 h at 37 °C. The mixtures were centrifuged to acquire erythrocytes pellet. Erythrocyte pellet was dispersed in PBS. The dispersion was dropped on glass slides to perform microscopy research.

Animal Model. All animal operations were carried out in accordance with institutional animal use and care regulations provided by Nanjing Normal University. Female BALB/c nude mice were inoculated by subcutaneous injection of 1×10^6 cells in 100 μL PBS on the axilla and brain of each mouse. For orthotopic glioblastoma models I, BALB/c nude mice (6-8 weeks old, female) were used. Anesthetized mice were fixed at a stereotaxic apparatus and then the brain was cleaned by 75 % ethanol. A hole was drilled with a 1 mm bit at 1.6 mm on the right side of bregma and 4.6 mm behind the coronal suture. Then the U87-MG cells (1×10^6) in 10 μL of PBS were injected 2.6 mm deep into the brain tissue for 10 min.

For the experiment of activating the brain immune system, in order to establish the animal brain tumor model with immunity, we can only select the GL261 cells for the experiment. In orthotopic glioblastoma models II, C57BL/6 mice (8 weeks old, female) were used. Anesthetized mice were fixed at a stereotaxic apparatus and then the brain was cleaned by 75 % ethanol. A hole was drilled with a 1 mm bit at 1.6 mm on the right side of bregma and 4.6 mm behind the coronal suture. GL261 cells (1×10^6) in 10 μL of PBS were injected 2.6 mm deep into the brain tissue for 10 min.

In Vivo Fluorescence and MR Imaging. BK@AIE NPs were intravenously injected into tumor-bearing mice. Fluorescent scans were performed at various time points of post-injection (2, 12, and 24 h) by a Maestro 2 Multispectral Small-animal Imaging System. BK@AIE NPs dissolved in DI water with different concentrations were scanned by a 3.0 T clinical MR

imaging scanner. T1 weighted animal MR imaging was performed under the same MR scanner with a special coil designed for small-animal imaging.

Blood Circulation. 200 μL of BK@AIE NPs was intravenously injected into five mice. At each time point, 20 μL of blood was collected from the mouse and then dissolved in 300 μL of lysis buffer (1% SDS, 1% Triton-100, 40 mM Tris-acetate, 10 mM EDTA, and 10 mM DTT). To extract BK@AIE NPs from blood, 300 μL of HCl/isopropanol was added. Then, the mixture was incubated in the dark overnight. By centrifuging to obtain the BK@AIE NPs in the supernatant, the amount of BK@AIE NPs remaining in the blood was determined by fluorescence.

In Vivo PTT for Subcutaneous Tumor Model. The subcutaneous U87-MG tumor-bearing mice were categorized into six groups in which five mice were used in each group. The six groups include (i) PBS only with intravenous injection of PBS; (ii) PBS with NIR laser irradiation treatment (980 nm, 0.72 W/cm^2, 5 min) on tumor site alone; (iii) AIE NPs group with intravenous injection of AIE NPs (2 mg/Kg); (iv) BK@AIE NPs group only with intravenous injection of BK@AIE NPs (2 mg/Kg); (v) "AIE NPs + laser" group with intravenous injection of AIE NPs (2 mg/kg). At 24 h post-injection of NPs, PTT was conducted using a 980 nm laser irradiation (0.72 W/cm^2) on tumor site for 5 min; and (vi) "AIE NPs + laser" group with intravenous injection of AIE NPs (2 mg/kg). At 24 h post-injection, PTT was carried out with a 980 nm laser (0.72 W/cm^2, 5 min) on the tumor site. After treatment, both the tumor size and body weight were continuously recorded. The tumor volume was evaluated using an equation.

$$\text{Tumor volume} = \text{length} \times (\text{width})^2/2.$$

Subsequently, the tumor volume was normalized to comparatively study tumor growth at different time points. After PTT treatment on day 18, major organs and tumors were collected, sectioned, and studied with H&E staining.

In Vivo Toxicity Test. Three groups of healthy BALB/c mice with five mice in each group were treated with BK@AIE NPs at changing concentrations (0, 1, and 5 mg/Kg), respectively. At 1, 7, and 18 days post-injection, mouse blood with a volume of about 0.8 mL was obtained through the ocular vein and tested using both blood biochemistry assay and blood panel test.

In Vivo PTT for an Orthotopic Brain Tumor. Similar to the *in vivo* subcutaneous tumor model, the mice bearing orthotopic brain tumors were classified into three groups and ten mice were

in each group. At 24 h sample post-injection, the three groups include (i) PBS with laser group only with 980 nm laser irradiation (0.72 W/cm^2) for 5 min on tumor site, (ii) AIE NPs with 980 nm laser irradiation (0.72 W/cm^2) for 5 min on tumor site, (iii) BK@AIE NPs with 980 nm laser irradiation (0.72 W/cm^2) for 5 min on tumor site. After PTT treatment, the mice extended their survival span to a certain degree but died afterward owing to the progress of brain tumors which have not been totally removed during PTT treatment. After PTT treatment on day 20, the brain was collected, sectioned, and studied by H&E, Congo red, and TUNEL staining to evaluate the PTT efficacy in different groups.

Flow Cytometry Analysis. Mouse intracranial tumors were harvested and dissociated with 1.5 μg/mL Liberase TL (Roche Diagnostics GmbH) in RPMI medium at 37 °C for 30 min. The dissociated GL261 tumor cells were filtered through 70 μm cell strainers and loaded into a 96-well plate (~10^6/well) for flow cytometry staining. After blocking with rat anti-mouse CD16/32 (Mouse BD Fc Block, clone 2.4G2, BD Biosciences), the cells from each tumor were split into two 96-well plates and stained with a panel of T-cell antibodies and a panel of NK/macrophage antibodies in parallel. Flow cytometry was performed using fluorescence-activated cell sorting (FACS). Furthermore, CD133 expression in the tumor was monitored by FACS. The median and peak fluorescence channels were determined using the Stat program in Cell Quest.

Cytokine Analysis. Blood was drawn from tumor-bearing mice after the PTT treatment, and serum was separated for cytokine analysis. The multiplex cytokine assay was performed using a custom Bio-Plex Pro Assay kit (Bio-Rad) including antibodies targeting IL-1β, IL-2, IL-10, IL-12 (p70), IFNγ, and TNFα, according to the manufacturer's instructions. Results were obtained using a Bio-Plex 200 System (Bio-Rad) equipped with Bio-Plex Manager Software (Bio-Rad) and data were processed using the same software.

Statistical Analysis. All statistical analyses were performed by an unpaired Student's t-test and one-way or two-way ANOVA with Bonferroni multiple comparisons post-test. Data were approximately normally distributed, and variance was similar between the groups. Statistical significance is indicated as $*P < 0.05$, $**P < 0.01$, and $***P < 0.001$.

Supporting Figures

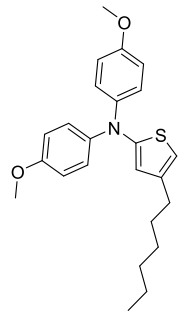

Bis(4-methoxyphenyl)amine (0.23 g, 1 mmol), 2-bromo-4-hexylthiophene (0.25 g, 1 mmol), $Pd_2(dba)_3$ (46 mg, 0.05 mmol), P(*t*-Bu)$_3$ (0.8 mL, 0.4 mmol, 10w/v% in pentane), NaOBu-*t* (21.3 mg, 1.3 mmol) and toluene (10 mL) were added into a two-necked flask. The mixture was refluxed for 24 h under protection of nitrogen. After cooling down to room temperature, water was added to quench the reaction and the organic phase was extracted and dried. The crude product was purified by a silica gel column to obtain the product (yield: 70%).

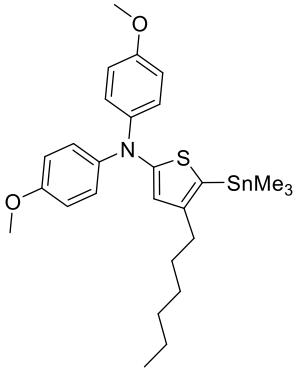

Add nBuLi (0.67 mL, 1.6 mmol, 2.4 M in hexane) dropwise to a solution of BBT-C6T (0.5 g, 1.2 mmol) in THF (10 mL) at -78 °C. Stirring the reaction mixture 1 h at -78 °C. Then trimethyltin chloride (1.6 mL, 1.6 mmol, 1.0 M in THF) was added into the reaction at one portion. After stirring the mixture for 12 h at room temperature, KF solution was added to quench the reaction. The mixture was extracted with hexane three times, the combined organic phase was dried with Na_2SO_4. After removing the solvent, the product was used directly without further purification.

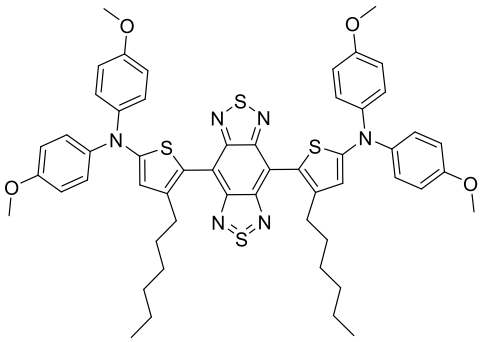

Under N_2 atmosphere, trimethyltin-substituted BBT-C6T (139 mg, 0.25 mmol), benzo[1,2-c:4,5-c′]bis([1,2,5]thiadiazole) (35 mg, 0.1 mmol), $Pd_2(dba)_3$ (9.2 mg, 0.01 mmol), P(*o*-tol)$_3$ (24.3 mg, 0.08 mmol) and 5 mL toluene were added to a two-necked flask. The mixture was refluxed for 24 h. After cooling down to room temperature, the solvent was removed by rotary evaporation. The crude product was purified by flash silica gel to obtain the target product (yield: 50%).

Figure S1. The detail synthesis procedure of BBT-C6T-DPA(OMe).

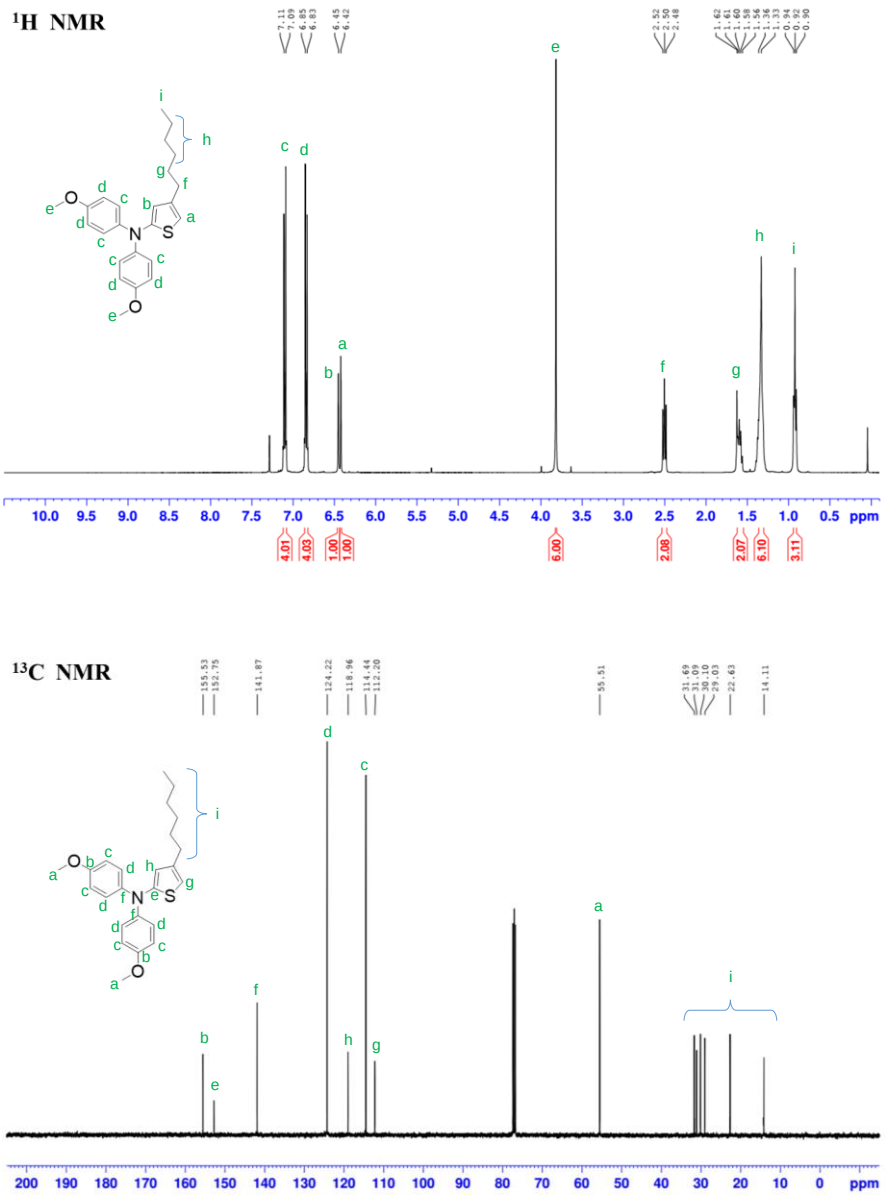

Figure S2. ^{1}H NMR and ^{13}C NMR spectrum of BBT-C6T in D-chloroform.

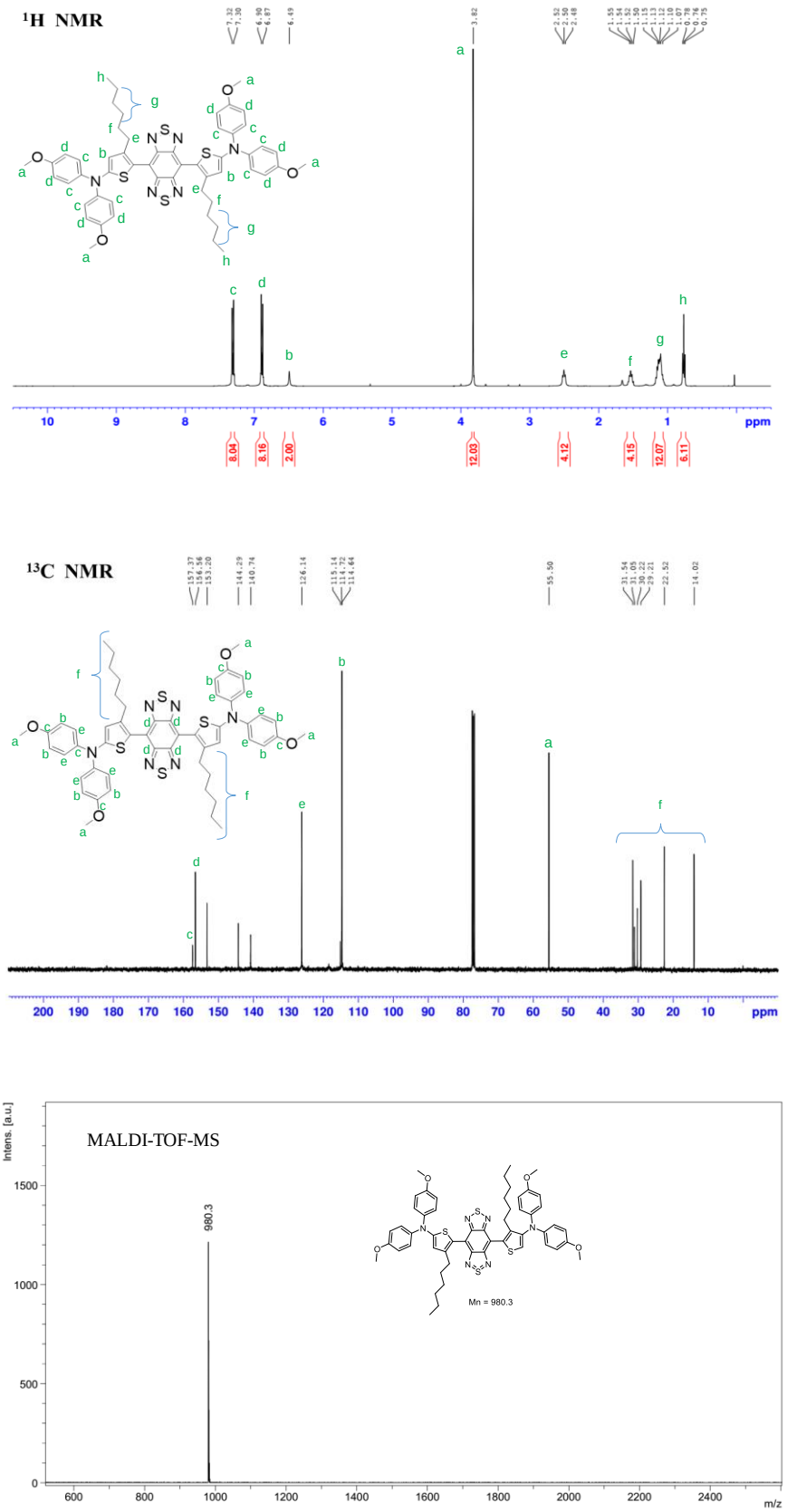

Figure S3. ^{1}H NMR, ^{13}C NMR, and MALDI-TOF-MS spectrum of BBT-C6T-DPA(OMe) in D-chloroform.

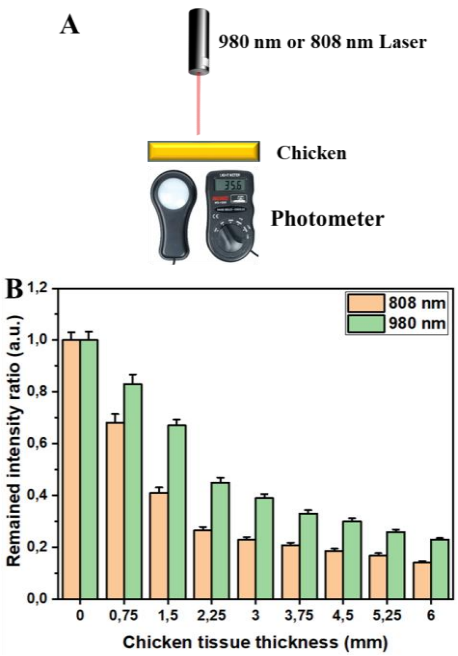

Figure S4. (A) Illustration of light penetration through different thickness of chicken tissues. (B) Quantitative results of remained intensity ratio after the light source penetrated chicken tissues with different thickness.

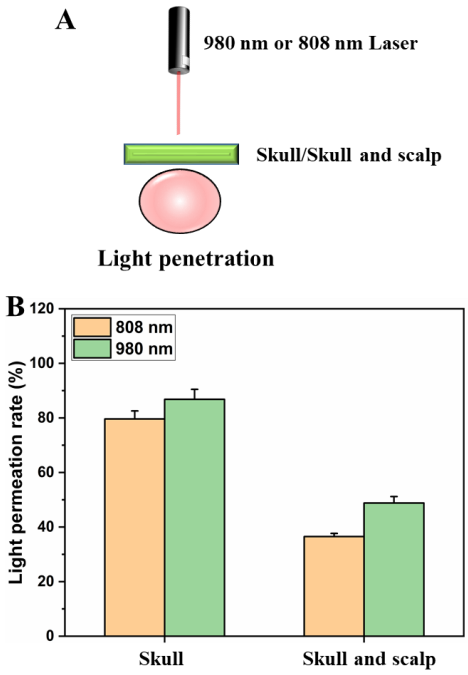

Figure S5. (A) Illustration of light penetration through skull, and skull together with scalp. (B) Quantitative results of light penetration rate after the light source penetrated through skull, and skull together with scalp.

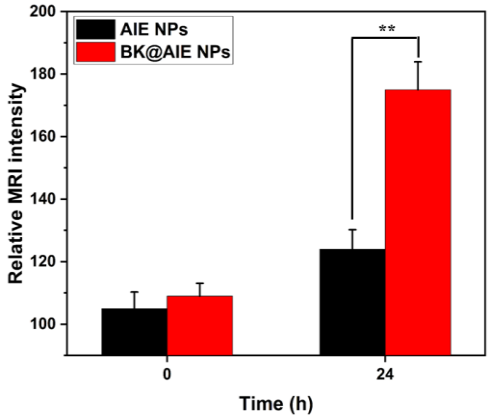

Figure S6. Quantitative signal intensity changes of the tumor treated with AIE NPs and BK@AIE NPs, $^{**}P < 0.01$.

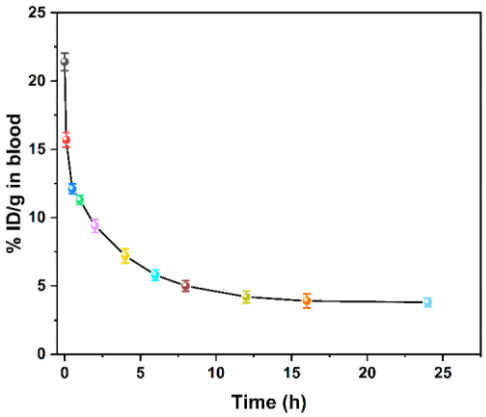

Figure S7. The blood circulation profile of BK@AIE NPs.

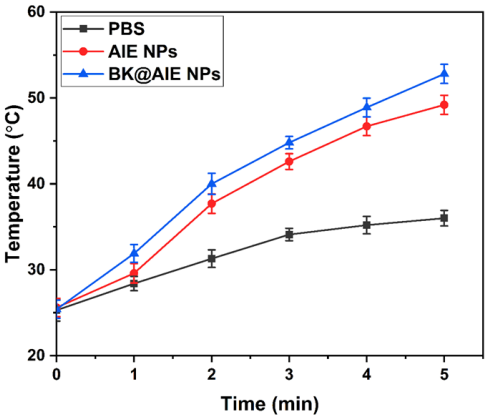

Figure S8. Temperature evaluations profiles of AIE NPs and BK@AIE NPs.

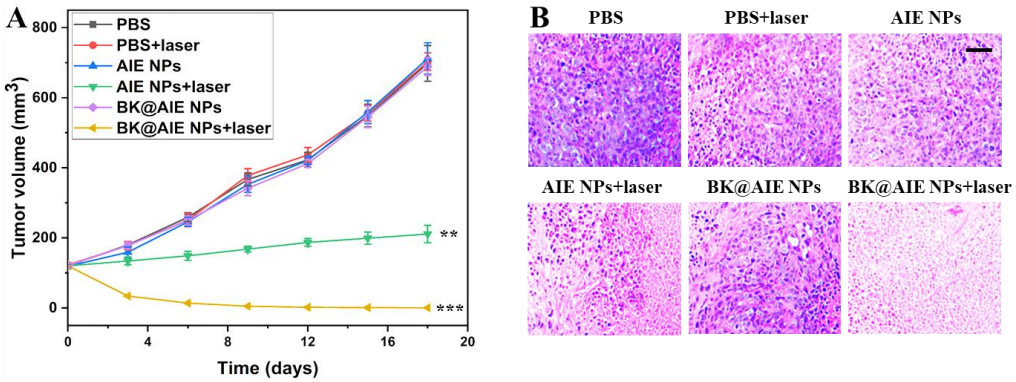

Figure S9. (A) Tumor volumes of mice treated with PBS, AIE NPs, and BK@AIE NPs with or without NIR laser irradiation (980 nm, 0.72 W/cm^2, 5 min), $^{**}P < 0.01$ and $^{***}P < 0.001$. (B) Representative H&E stained images of tumors, which were collected from the mice after different treatments. Scale bar: 100 μm

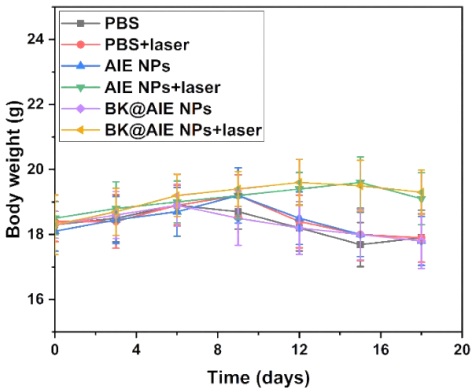

Figure S10. Mice weight after treating with PBS, AIE NPs, and BK@AIE NPs with or without NIR laser irradiation (980 nm, 0.72 W/cm^2, 5 min).

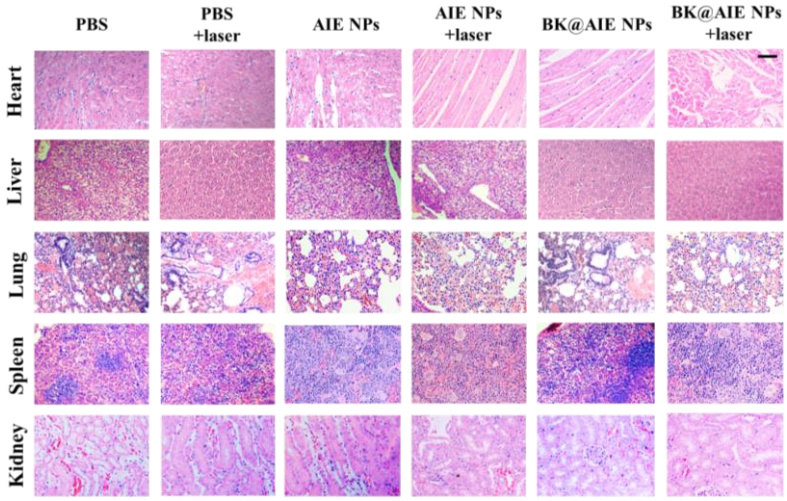

Figure S11. Representative H&E stained images of major organs, which were collected from the mice after different treatments. Scale bar: 100 μm

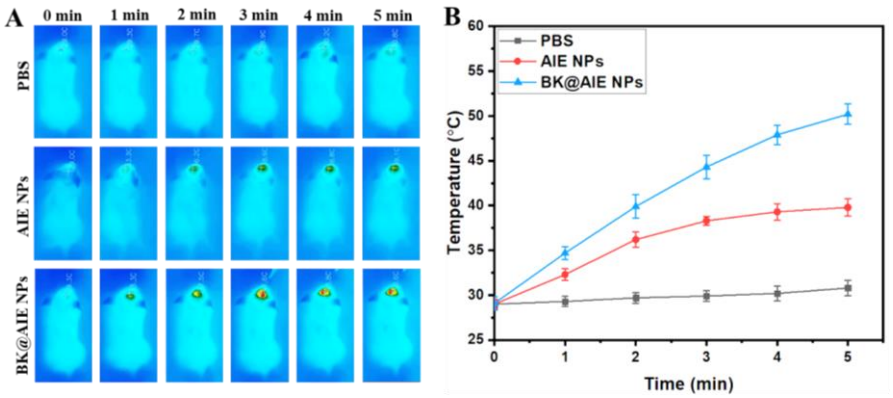

Figure S12. (A) *In vivo* whole body thermal images of mice treated with PBS, AIE NPs, and BK@AIE NPs after NIR laser irradiation (980 nm, 0.72 W/cm^2, 5 min); images were obtained using a thermal camera. (B) Kinetic temperature changes of mice treated with PBS, AIE NPs, and BK@AIE NPs after NIR laser irradiation (980 nm, 0.72 W/cm^2, 5 min).

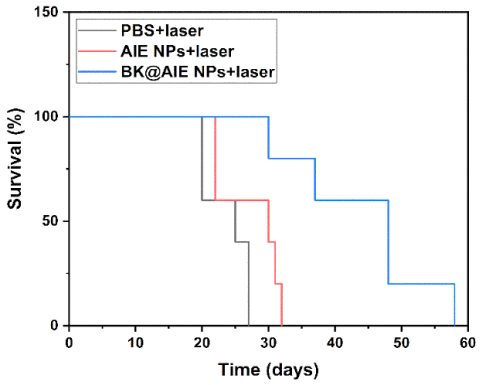

Figure S13. Mice survival rates after PTT treatment.

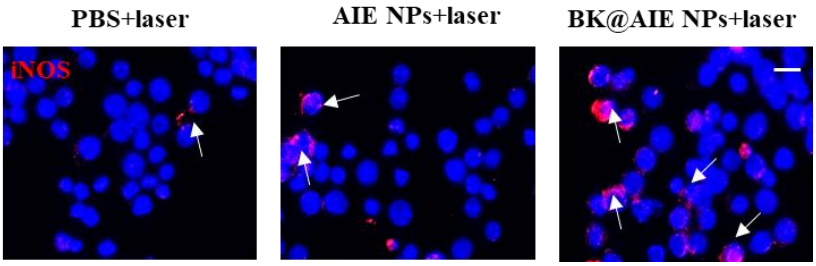

Figure S14. *Ex vivo* study of M1 MΦ by immunostaining for iNOS (white arrows) demonstrates their increased numbers in the brain tumors after PTT treatment. Scale bar: 20 μm

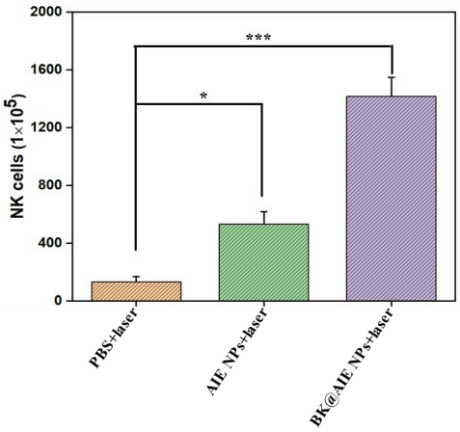

Figure S15. Flow cytometric quantification of intratumoral proliferation of NK cells after PTT treatment, **P* < 0.05 and ****P* < 0.001.

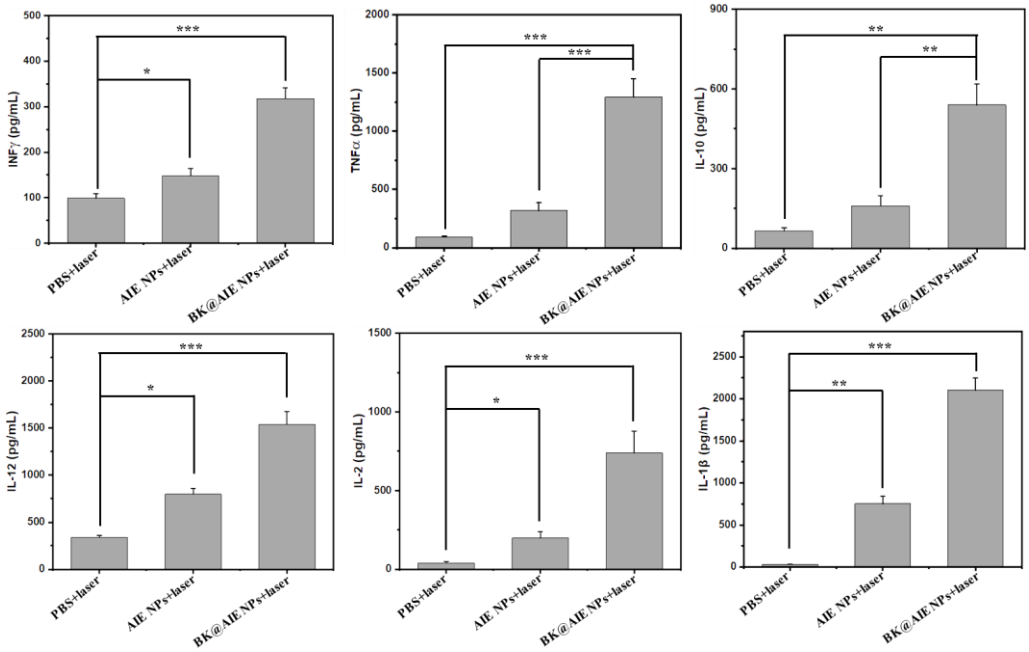

Figure S16. Inflammatory cytokine INFγ, TNFα, IL-10, IL-12, IL-2, and IL-1β levels in mice brain tissues after PTT treatment, **P* < 0.05, ***P* < 0.01, and ****P* < 0.001.

BIBLIOGRAPHY

[1] M. R. Umarkar, *Int. J. Technol. Sci. Res.* **2018**, *4*, 263064.
[2] Y. Liu, E. B. Carson-Walter, A. Cooper, B. N. Winans, M. D. Johnson, K. A. Walter, *J. Neurooncol.* **2010**, *99*, 13.
[3] G. Seano, H. T. Nia, K. E. Emblem, M. Datta, J. Ren, S. Krishnan, J. Kloepper, M. C. Pinho, W. W. Ho, M. Ghosh, *Nat. Biomed. Eng.* **2019**, *3*, 230.
[4] P. A. Forsyth, J. B. Posner, *Neurology* **1993**, *43*, 1678.
[5] H. Snyder, K. Robinson, D. Shah, R. Brennan, M. Handrigan, *J. Emerg. Med.* **1993**, *11*, 253.
[6] D. A. Reardon, K. L. Fink, T. Mikkelsen, T. F. Cloughesy, A. O'Neill, S. Plotkin, M. Glantz, P. Ravin, J. J. Raizer, K. M. Rich, *Clin. Oncol.* **2007**, *26*, 5610.
[7] L. Souhami, W. Seiferheld, D. Brachman, E. B. Podgorsak, M. Werner-Wasik, R. Lustig, C. J. Schultz, W. Sause, P. Okunieff, J. Buckner, *Int. J. Radiat. Oncol. Biol. Phys.* **2004**, *60*, 853.
[8] K. Melnick, D. Shin, F. Dastmalchi, Z. Kabeer, M. Rahman, D. Tran, A. Ghiaseddin, *Curr. Treat. Options Oncol.* **2021**, *22*, 1.
[9] A. Iyer, G. Harrison, H. Kano, G. M. Weiner, N. Luther, A. Niranjan, J. C. Flickinger, L. D. Lunsford, D. Kondziolka, *J. Neurosurg.* **2014**, *121*, 564.
[10] S. R. Chandana, S. Movva, M. Arora, T. Singh, *Am. Fam. Physician* **2008**, *77*, 1423.
[11] R. Sawaya, B. L. Ligon, A. K. Bindal, R. K. Bindal, K. R. Hess, *J. Neurooncol.* **1996**, *27*, 269.
[12] P. Salander, T. Bergenheim, R. Henriksson, *Soc. Sci. Med.* **1996**, *42*, 985.
[13] L. Rigante, H. Borghei-Razavi, P. F. Recinos, F. Roser, *Cleve. Clin. J. Med.* **2019**, *86*, 16.
[14] E. de Divitiis, L. M. Cavallo, P. Cappabianca, F. Esposito, *Neurosurgery* **2007**, *60*, 46.
[15] https://www.mskcc.org/cancer-care/patient-education/radiation-therapy-brain
[16] J. G. Cairncross, J. H. Kim, J. B. Posner, *Ann. Neurol.* **1980**, *7*, 529.
[17] https://www.parkwaycancercentre.com/in/news-events/news-articles/news-articles-details/brain-cancer-treatment-using-radiotherapy
[18] C. Nieder, A. Leicht, B. Motaref, U. Nestle, M. Niewald, K. Schnabel, *Am. J. Clin. Oncol.* **1999**, *22*, 573.
[19] M. Stovall, C. R. Blackwell, J. Cundiff, D. H. Novack, J. R. Palta, L. K. Wagner, E. W. Webster, R. J. Shalek, *Med. Phys.* **1995**, *22*, 63.
[20] M. D. Prados, C. Russo, *Semin. Surg. Oncol.* **1998**, *14*, 88.
[21] D. J. Stewart, M. Leavens, M. Maor, L. Feun, M. Luna, J. Bonura, R. Caprioli, T. L. Loo, R. S. Benjamin, *Cancer Res.* **1982**, *42*, 2474.
[22] H. Potschka, M. Fedrowitz, W. Löscher, *J. Pharmacol. Exp. Ther.* **2003**, *306*, 124.
[23] L. Sasongko, J. M. Link, M. Muzi, D. A. Mankoff, X. Yang, A. C. Collier, S. C. Shoner, J. D. Unadkat, *Clin. Pharmacol. Ther.* **2005**, *77*, 503.
[24] H. S. Chan, G. Haddad, P. S. Thorner, G. DeBoer, Y. P. Lin, N. Ondrusek, H. Yeger, V. Ling, *N. Engl. J. Med.* **1991**, *325*, 1608.
[25] J. Li, T. Tan, L. Zhao, M. Liu, Y. You, Y. Zeng, D. Chen, T. Xie, L. Zhang, C. Fu, *ACS Appl. Bio Mater.* **2020**, *3*, 5500.
[26] T. Friedmann, *Science* **1989**, *244*, 1275.
[27] B. Everts, H. G. van der Poel, *Cancer Gene Ther.* **2005**, *12*, 141.
[28] S. O. Freytag, K. R. Rogulski, D. L. Paielli, J. D. Gilbert, J. H. Kim, *Hum. Gene Ther.* **1998**, *9*, 1323.
[29] C. H. Fan, E. L. Chang, C. Y. Ting, Y. C. Lin, E. C. Liao, C. Y. Huang, Y. C. Chang, H. L. Chan, K. C. Wei, C. K. Yeh, *Biomaterials* **2016**, *106*, 46.
[30] J. Polivka, L. Holubec, T. Kubikova, V. Priban, O. Hes, K. Pivovarcikova, I. Treskova, *Anticancer Res.* **2017**, *37*, 21.
[31] H. Okura, C. A. Smith, J. T. Rutka, *Mol. Cell. Ther* **2014**, *2*, 1.
[32] K. K. Jain, *Front. Oncol.* **2018**, *8*, 419.
[33] S. Wang, G. Balasundaram, *Curr. Gene Ther.* **2010**, *10*, 214.
[34] S. Missios, K. Bekelis, G. H. Barnett, *Neurosurg. Focus* **2015**, *38*, 13.
[35] M. Sharma, S. Balasubramanian, D. Silva, G. H. Barnett, A. M. Mohammadi, *Expert Rev. Neurother.* **2016**, *16*, 223.
[36] U. Salem, V. A. Kumar, J. E. Madewell, D. F. Schomer, D. C. de Almeida Bastos, P. O. Zinn, J. S. Weinberg, G. Rao, S. S. Prabhu, R. R. Colen, *Cancer Imaging* **2019**, *19*, 1.

[37] R. Pruitt, A. Gamble, K. Black, M. Schulder, A. D. Mehta, *J. Neurosurg.* **2017**, *126*, 1238.
[38] F. A. Mirza, R. Mitha, M. S. Shamim, *Asian. J. Neurosurg.* **2020**, *15*, 800.
[39] H. Wolburg, A. Lippoldt, *Vascul. Pharmacol.* **2002**, *38*, 323.
[40] A. P. Stout, *Ann. Surg.* **1943**, *118*, 445.
[41] H. Wolburg, S. Noell, A. Mack, K. Wolburg-Buchholz, P. Fallier-Becker, *Cell Tissue Res.* **2009**, *335*, 75.
[42] A. Warth, S. Kröger, H. Wolburg, *Acta Neuropathol.* **2004**, *107*, 311.
[43] R. Pandit, L. Chen, J. Götz, *Adv. Drug Del. Rev.* **2020**, *165*, 1.
[44] S. Logan, T. Arzua, S. G. Canfield, E. R. Seminary, S. L. Sison, A. D. Ebert, X. Bai, *Compr. Physiol.* **2019**, *9*, 565.
[45] J. Bicker, G. Alves, A. Fortuna, A. Falcão, *Eur. J. Pharm. Biopharm.* **2014**, *87*, 409.
[46] G. Chen, M. A. Davies, *Biochem. Pharmacol.* **2012**, *83*, 305.
[47] P. S. Steeg, *Nat. Rev. Clin. Oncol.* **2021**, *18*, 696.
[48] M. Strazza, V. Pirrone, B. Wigdahl, M. R. Nonnemacher, *Brain Res.* **2011**, *1399*, 96.
[49] K.-H. Song, B. K. Harvey, M. A. Borden, *Theranostics* **2018**, *8*, 4393.
[50] E. E Konofagou, Y.-S. Tunga, J. Choia, T. Deffieuxa, B. Baseria, F. Vlachosa, *Curr. Pharm. Biotechnol.* **2012**, *13*, 1332.
[51] T. Sun, G. Samiotaki, S. Wang, C. Acosta, C. C. Chen, E. E. Konofagou, *Phys. Med. Biol.* **2015**, *60*, 9079.
[52] S. K. Wu, P. C. Chu, W. Y. Chai, S. T. Kang, C. H. Tsai, C. H. Fan, C. K. Yeh, H. L. Liu, *Sci. Rep.* **2017**, *7*, 1.
[53] L. R. Morgan, F. B. Sarica, *Brain and Spinal Tumors: Primary and Secondary*, BoD–Books on Demand, **2020**.
[54] G. P. Skandalakis, D. R. Rivera, C. D. Rizea, A. Bouras, J. G. Jesu Raj, D. Bozec, C. G. Hadjipanayis, *Int. J. Hyperthermia* **2020**, *37*, 3.
[55] D. M. Smith, J. K. Simon, J. R. Baker Jr, *Nat. Rev. Immunol.* **2013**, *13*, 592.
[56] A. C. Anselmo, S. Mitragotri, *Bioeng. Transl. Med.* **2016**, *1*, 10.
[57] F. Persano, S. Leporatti, *Curr. Nanomater.* **2020**, *5*, 92.
[58] F. Xiao, L. Lin, Z. Chao, C. Shao, Z. Chen, Z. Wei, J. Lu, Y. Huang, L. Li, Q. Liu, *Angew. Chem.* **2020**, *132*, 9789.
[59] D. Gao, D. Hu, X. Liu, Z. Sheng, H. Zheng, *Nanoscale Horiz.* **2019**, *4*, 1037.
[60] J. V. Georgieva, D. Hoekstra, I. S. Zuhorn, *Pharmaceutics* **2014**, *6*, 557.
[61] J. Yoo, C. Park, G. Yi, D. Lee, H. Koo, *Cancers (Basel)* **2019**, *11*, 640.
[62] R. C. Gupta, *Handbook of toxicology of chemical warfare agents*, *Academic Press*, **2015**.
[63] M. Ramezanpour, S. Leung, K. Delgado-Magnero, B. Bashe, J. Thewalt, D. Tieleman, *Biochim. Biophys. Acta Biomembr.* **2016**, *1858*, 1688.
[64] J. M Rabanel, V. Aoun, I. Elkin, M. Mokhtar, P. Hildgen, *Curr. Med. Chem.* **2012**, *19*, 3070.
[65] J. Ramos, J. Forcada, R. Hidalgo-Alvarez, *Chem. Rev.* **2014**, *114*, 367.
[66] S. Liu, S. Yang, P. C. Ho, *Asian J. Pharm. Sci.* **2018**, *13*, 72.
[67] S. M. Moghimi, *Adv. Drug Del. Rev.* **1995**, *17*, 103.
[68] C. S. Lewis, State University of New York at Stony Brook, **2016**.
[69] S. Ohta, E. Kikuchi, A. Ishijima, T. Azuma, I. Sakuma, T. Ito, *Sci. Rep.* **2020**, *10*, 1.
[70] "CROSSING THE BLOOD BRAIN BARRIER (BBB) WHICH ROUTE TO TAKE ?", **2015**.
[71] S. G. Boyce, *Amyloid precursor protein subtypes and secretases implicated in Alzheimer's disease, Sheffield Hallam University (United Kingdom)*, **2011**.
[72] P. McCrorie, C. E. Vasey, S. J. Smith, M. Marlow, C. Alexander, R. Rahman, *J. Control. Release* **2020**, *328*, 917.
[73] G. Frosina, *Brain Pathol.* **2016**, *26*, 689.
[74] L. R. Hanson, W. H. Frey, *J. Neuroimmune Pharmacol.* **2007**, *2*, 81.
[75] H. L. Weiner, C. A. Lemere, R. Maron, E. T. Spooner, T. J. Grenfell, C. Mori, S. Issazadeh, W. W. Hancock, D. J. Selkoe, *Ann. Neurol.* **2000**, *48*, 567.
[76] A. Mangraviti, S. Y. Tzeng, D. Gullotti, K. L. Kozielski, J. E. Kim, M. Seng, S. Abbadi, P. Schiapparelli, R. Sarabia-Estrada, A. Vescovi, *Biomaterials* **2016**, *100*, 53.
[77] H. H. Mahmoud, G. K. Rivera, M. L. Hancock, R. A. Krance, L. E. Kun, F. G. Behm, R. C. Ribeiro, J. T. Sandlund, W. M. Crist, C.-H. Pui, *N. Engl. J. Med.* **1993**, *329*, 314.
[78] A. Misra, S. Ganesh, A. Shahiwala, S. P. Shah, *J. Pharm. Pharm. Sci.* **2003**, *6*, 252.
[79] P. Beauchesne, *Lancet Oncol.* **2010**, *11*, 871.

[80] https://scasource.net/2020/08/14/snapshot-intrathecal-injections/
[81] J. M. Lajoie, E. V. Shusta, *Annu. Rev. Pharmacol. Toxicol.* **2015**, *55*, 613.
[82] M. Braun, J. J. Iliff, *Int. Rev. Neurobiol.* **2020**, *154*, 413.
[83] P. Van Dyken, B. Lacoste, *Front. Neurosci.* **2018**, *12*, 930.
[84] F. A. Jolesz, *Annu. Rev. Med.* **2009**, *60*, 417.
[85] A. Dréan, N. Lemaire, G. Bouchoux, L. Goldwirt, M. Canney, L. Goli, A. Bouzidi, C. Schmitt, J. Guehennec, M. Verreault, *J. Neurooncol.* **2019**, *144*, 33.
[86] A. Weiss, H. van den Bergh, A. W. Griffioen, P. Nowak-Sliwinska, *Biochim. Biophys. Acta Rev. Cancer* **2012**, *1826*, 53.
[87] J. C. Kennedy, R. H. Pottier, *J. Photochem. Photobiol. B: Biol.* **1992**, *14*, 275.
[88] W. G. Roberts, T. Hasan, *Cancer Res.* **1992**, *52*, 924.
[89] L. Gao, R. Liu, F. Gao, Y. Wang, X. Jiang, X. Gao, *ACS Nano* **2014**, *8*, 7260.
[90] N. Mehraban, H. S. Freeman, *Materials* **2015**, *8*, 4421.
[91] B. Chen, L. Shen, E. Pun, H. Lin, *Opt. Express* **2012**, *20*, 879.
[92] J. W. Kleinovink, P. B. van Driel, T. J. Snoeks, N. Prokopi, M. F. Fransen, L. J. Cruz, L. Mezzanotte, A. Chan, C. W. Löwik, F. Ossendorp, *Clin. Cancer. Res.* **2016**, *22*, 1459.
[93] H. Chen, X. Zhou, Y. Gao, B. Zheng, F. Tang, J. Huang, *Drug Discov. Today* **2014**, *19*, 502.
[94] X. Deng, Z. Shao, Y. Zhao, *Adv. Sci.* **2021**, *8*, 2002504.
[95] G. G. Yang, D. J. Zhou, Z. Y. Pan, J. Yang, D. Y. Zhang, Q. Cao, L. N. Ji, Z. W. Mao, *Biomaterials* **2019**, *216*, 119280.
[96] X. Song, Q. Chen, Z. Liu, *Nano Res.* **2015**, *8*, 340.
[97] H. Huang, J. F. Lovell, *Adv. Funct. Mater.* **2017**, *27*, 1603524.
[98] Y. Chen, Z. Li, H. Wang, Y. Wang, H. Han, Q. Jin, J. Ji, *ACS Appl. Mater. Interfaces* **2016**, *8*, 6852.
[99] N. Rabiee, M. T. Yaraki, S. M. Garakani, S. M. Garakani, S. Ahmadi, A. Lajevardi, M. Bagherzadeh, M. Rabiee, L. Tayebi, M. Tahriri, *Biomaterials* **2020**, *232*, 119707.
[100] J. Chen, C. Ning, Z. Zhou, P. Yu, Y. Zhu, G. Tan, C. Mao, *Prog. Mater Sci.* **2019**, *99*, 1.
[101] L. Xu, L. Cheng, C. Wang, R. Peng, Z. Liu, *Polym. Chem.* **2014**, *5*, 1573.
[102] S. Li, Q. Deng, Y. Zhang, X. Li, G. Wen, X. Cui, Y. Wan, Y. Huang, J. Chen, Z. Liu, *Adv. Mater.* **2020**, *32*, 2001146.
[103] M. M. Mueller, N. E. Fusenig, *Nat. Rev. Cancer* **2004**, *4*, 839.
[104] E. F. McCarthy, *Iowa Orthop. J.* **2006**, *26*, 154.
[105] M. Peng, Y. Mo, Y. Wang, P. Wu, Y. Zhang, F. Xiong, C. Guo, X. Wu, Y. Li, X. Li, *Mol. Cancer* **2019**, *18*, 1.
[106] M. Canning, G. Guo, M. Yu, C. Myint, M. W. Groves, J. K. Byrd, Y. Cui, *Front. Cell Dev. Biol.* **2019**, *7*, 52.
[107] Y. Zhang, Z. Zhang, *Cell. Mol. Immunol.* **2020**, *17*, 807.
[108] W. K. Decker, R. F. da Silva, M. H. Sanabria, L. S. Angelo, F. Guimarães, B. M. Burt, F. Kheradmand, S. Paust, *Front. Immunol.* **2017**, *8*, 829.
[109] S. J. Till, J. N. Francis, K. Nouri-Aria, S. R. Durham, *J. Allergy Clin. Immunol.* **2004**, *113*, 1025.
[110] K. Esfahani, L. Roudaia, N. Buhlaiga, S. Del Rincon, N. Papneja, W. Miller, *Curr. Oncol.* **2020**, *27*, 87.
[111] P. Darvin, S. M. Toor, V. S. Nair, E. Elkord, *Exp. Mol. Med.* **2018**, *50*, 1.
[112] M. Preusser, M. Lim, D. A. Hafler, D. A. Reardon, J. H. Sampson, *Nat. Rev. Neurol.* **2015**, *11*, 504.
[113] J. D. Martin, H. Cabral, T. Stylianopoulos, R. K. Jain, *Nat. Rev. Clin. Oncol.* **2020**, *17*, 251.
[114] W. R. Chen, M. Korbelik, K. E. Battels, H. Liu, J. Sun, R. E. Nordquist, *Photochem. Photobiol.* **2005**, *81*, 190.
[115] X. Li, M. F. Naylor, H. Le, R. E. Nordquist, T. K. Teague, C. A. Howard, C. Murray, W. R. Chen, *Cancer Biol. Ther.* **2010**, *10*, 1081.
[116] T. Nagaya, J. Friedman, Y. Maruoka, F. Ogata, S. Okuyama, P. E. Clavijo, P. L. Choyke, C. Allen, H. Kobayashi, *Cancer Immunol. Res.* **2019**, *7*, 401.
[117] W. R. Chen, J. W. Ritchey, K. E. Bartles, M. D. Lucroy, H. Liu, R. E. *Saratov Fall Meeting 2001: Optical Technologies in Biophysics and Medicine III*, **2002**.
[118] Q. Chen, L. Xu, C. Liang, C. Wang, R. Peng, Z. Liu, *Nat. Commun.* **2016**, *7*, 1.
[119] L. Zou, H. Wang, B. He, L. Zeng, T. Tan, H. Cao, X. He, Z. Zhang, S. Guo, Y. Li, *Theranostics* **2016**, *6*, 762.
[120] M. Yang, T. Yang, C. Mao, *Angew. Chem. Int. Ed.* **2019**, *58*, 14066.

[121] E. R. Padayachee, F. A. N. Biteghe, Z. Malindi, D. Bauerschlag, S. Barth, *Transfus. Med. Hemother.* **2017**, *44*, 303.
[122] X. Xu, H. Lu, R. Lee, *Front. Bioeng. Biotechnol.* **2020**, *8*, 488.
[123] J. Yang, C. Zhang, *Wiley Interdiscip. Rev.: Nanomed. Nanobiotechnol.* **2020**, *12*, 1612.
[124] C. Wu, Y. Wu, X. Zhu, J. Zhang, J. Liu, Y. Zhang, *Nano Today* **2021**, *36*, 100963.
[125] S. Gao, X. Yang, J. Xu, N. Qiu, G. Zhai, *ACS Nano* **2021**, *15*, 12567.
[126] Y. Xing, Y. Cai, J. Cheng, X. Xu, *Appl. Nanosci.* **2020**, *10*, 2069.
[127] X. Gao, Q. Yue, Z. Liu, M. Ke, X. Zhou, S. Li, J. Zhang, R. Zhang, L. Chen, Y. Mao, *Adv. Mater.* **2017**, *29*, 1603917.
[128] K. Fan, X. Jia, M. Zhou, K. Wang, J. O. Conde, J. He, J. Tian, X. Yan, *Acs Nano* **2018**, *12*, 4105.
[129] X. Li, Y. Yang, H. Zhao, T. Zhu, Z. Yang, H. Xu, Y. Fu, F. Lin, X. Pan, L. Li, *J. Am. Chem. Soc.* **2020**, *142*, 3862.
[130] a) T. T. Zhang, W. Li, G. Meng, P. Wang, W. Liao, *Biomater. Sci.* **2016**, *4*, 219; b) R. Qiao, Q. Jia, S. Huwel, R. Xia, T. Liu, F. Gao, M. Gao, *ACS Nano*. **2012**, *6*, 3304; c) S. Wohlfart, A. S. Khalansky, S. Gelperina, D. Begley, J. Kreuter, *J. Control. Release*, **2011**,*154*, 103.
[131] Y. Song, D. Du, L. Li, J. Xu, P. Dutta, Y. Lin, *ACS Appl. Mater. Interfaces* **2017**, *9*, 20410.
[132] T. Lin, P. Zhao, Y. Jiang, Y. Tang, H. Jin, Z. Pan, H. He, V. C. Yang, Y. Huang, *ACS Nano* **2016**, *10*, 9999.
[133] a) K. B. Johnsen, T. Moos, *J. Control. Release* **2016**, *222*, 32; b) K. B. Johnsen, M. Bak, F. Melander, M. S.Thomsen, A. Burkhart, P. J. Kempen, T. Moos, *J. Control. Release* **2019**, *295*, 237; c) G. Sharma, A. R. Sharma, S. S. Lee, M. Bhattacharya, J. S. Nam, C. Chakraborty, *Int. J. Pharm.* **2019**, *559*, 360.
[134] Y. Xu, G. K.-W. Kong, J. G. Menting, M. B. Margetts, C. A. Delaine, L. M. Jenkin, V. V. Kiselyov, P. De Meyts, B. E. Forbes, M. C. Lawrence, *Nat. Commun.* **2018**, *9*, 1.
[135] J. S. Smith, S. Rajagopal, *J. Biol. Chem.* **2016**, *291*, 8969.
[136] J. Zhang, X. Zhang, G. Liu, D. Chang, X. Liang, X. Zhu, W. Tao, L. Mei, *Theranostics* **2016**, *6*, 2099.
[137] X. Hu, R. K. Leak, A. W. Thomson, F. Yu, Y. Xia , L. R.Wechsler, J. Chen, *Nat. Rev. Neurol.* **2018**, *14*, 559.
[138] J. Côté, V. Bovenzi, M. Savard, C. Dubuc, A. Fortier, W. Neugebauer, L. Tremblay, W. Müller-Esterl, A.-M. Tsanaclis, M. Lepage, *PLoS One* **2012**, *7*, 37485.
[139] https://ccr.cancer.gov/news/article/japan-approves-photoimmunotherapy-for-head-and-neck-cancer
[140] https://www.japantimes.co.jp/news/2021/07/02/national/science-health/japan-cancer-photoimmunotherapy/
[141] H. Kobayashi, A. Furusawa, A. Rosenberg, P. L. Choyke, *Int. Immunol.* **2021**, *33*, 7.
[142] Y. Maruoka, H. Wakiyama, P. L. Choyke, H. Kobayashi, *EBioMedicine* **2021**, *70*, 103501.
[143] H. Wakiyama, T. Kato, A. Furusawa, P. L. Choyke, H. Kobayashi, *Nanophotonics* **2021**, *10*, 3135.
[144] V. R. Juneja, K. A. McGuire, R. T. Manguso, M. W. LaFleur, N. Collins, W. N. Haining, G. J. Freeman, A. H. Sharpe, *J. Exp. Med.* **2017**, *214*, 895.
[145] B. J. Zheng, K. W. Chan, S. Im, D. Chua, J. S. Sham, P. C. Tin, Z. M. He, M. H. Ng, *Int. J. Cancer* **2001**, *92*, 421.